POLITECNICO DI MILANO

SCHOOL OF INDUSTRIAL AND INFORMATION ENGINEERING

Energy Engineering Master of Science

INNOVATIVE CSP TOWER SYSTEM COUPLED WITH SOLAR MICRO GAS TURBINE

Supervisor: Prof. Giovanni Lozza
Assitant supervisors: Prof. Andrea Giostri e Prof. Marco Binotti

Author: Camilla Margherita Maria Sterpos
ID: 836761

Academic Year 2015 – 2016

Ringraziamenti

Con questa tesi concludo il grande capitolo studentesco della mia vita. Non è stato sempre facile, ma arrivata al traguardo mi rendo conto di quanto io abbia imparato; sia a livello didattico che a livello personale. Il Politecnico mi ha permesso di conoscere persone di grande valore, di sapere cosa veramente voglia dire impegnarsi, di vivere esperienze uniche come pilotare un aereo, di trascorrere un periodo in Australia; forgiando cosi il mio carattere e arricchendo il bagaglio che porto oggi con me.
Nonostante pensi che questo mio percorso sia frutto di circostanze, di persone che ho conosciuto, che siano professori, amici, parenti, o persone incrociate per caso, vorrei ringraziare in particular modo:

Il Professore Giovanni Lozza per avermi dato l'opportunità di questa tesi.

I Professori Andrea Giostri e Marco Binotti per la pazienza, le idee, l'aiuto alla programmazione, lo stimolo ad approffondire la mia ricerca, ed i consigli sulla scrittura stessa di questa tesi.

I miei compagni di università, dalla Triennale alla Magistrale, quelli che sento ancora e quelli che ho perso di vista, per tutte le risate che hanno alleggerito questi anni, per tutte le ore passate a studiare insieme, e per tutti gli sfoghi dopo le sconfitte.

La squadra di Tennis del Politecnico, alcuni dei quali oggi considero tra i miei migliori amici, per tutte le avventure a Milano, in montagna, a Tolosa.. Sono ricordi che mai dimenticherò.

Le mie amiche "francesi" di sempre, per gli svaghi, le cene, le feste, ma soprattutto per gli incoraggiamenti a proseguire i miei studi, ricordandomi chi sono veramente.

Le mie sorelle Carolina, Federica, Valeria e i loro mariti, per tutti i consigli (Luigi, chissà che ingegneria avrei scelto se tu non ci fossi stato…) e il conforto di non sentirsi mai sola, nemmeno nei momenti più difficili.

Giacomo, per capirmi, sopportarmi e credere in me. Spero di poter continuare a sognare con te.

Ed infine i miei genitori, senza i quali non avrei mai fatto niente di tutto ciò. Grazie per aver creduto in me, senza mai fare troppi complimenti, ma sempre appoggiando le mie idee. Mi avete insegnato l'ambizione, senza la pretenzione. Devo a voi le mie qualità, pur sapendo che avete ancora tanto da insegnarmi.

Index

List of figures

Abstract

In this thesis a complete thermodynamic, operational and economic analysis of a solar micro gas turbine is presented (design net power output of 187.25 kW_e).
The heliostats field is taken from the existing plant of Aora in Almeria (Spain) while the tower receiver is optimized to give the maximum annual performances (optical efficiency of 72.02%).
Following a description of the components necessary to implement the power block, such as the volumetric receiver (allowing a higher maximum temperature with respect to a tubular receiver, respectively 1200°C and 800°C), a Matlab model is developed to simulate both on-design and off-design performances of the system. Technical constraints regarding the receiver, the recuperator, the combustor and the gas turbine engine (operating up to 950°C to avoid cooled-blade technologies) are accounted for a correct run. On-design conditions are characterized by a DNI of 950 W/m^2 (based on peak flux) and an ambient temperature of 35°C, which correspond to an incident power from the sun of 790 W and a resulting solar-block efficiency of 32.99% while the solar-to-electric efficiency is 23.71%. The exergy analysis of the design system is also presented, highlighting a total second-law-efficiency loss of 74.51%, mostly due to the solar block (loss of 46.31%).
Referring to the GSE in Italy, a power plant can access renewable incentives while using an annual fuel-integration up to 15%. Thus, off-design conditions of the system also include hybridization.
Different strategies of operations are considered, such as the solar-only-mode (annual energy of 285.3 MWh_{el} and annual η_{sol-el} of 0.2189), the nominal-power-mode with heavy fossil fuel firing (annual energy of 479.0 MWh_{el} and annual η_{sol-el} of 0.2141), the maximum cycle efficiency mode (annual energy of 398.2 MWh_{el} and annual η_{sol-el} of 0.2325), the hourly fuel-control of 15% (annual energy of 333.9 MWh_{el} and annual η_{sol-el} of 0.2176) and the optimal renewable strategy with hybridization only when sun's irradiation is low (annual energy of 339.0 MWh_{el} and annual η_{sol-el} of 0.2239). A particular attention on CO_2 emissions-savings with respect to a standard gas turbine is exposed.
Based on the reliable power-block costs (346.33 euro/kW_e), and on the more uncertain solar-block costs (2444.24 euro/kW_e), the final economic analysis is computed considering two possible discount rates, presenting a best scenario (LCOE of 0.2064 euro/kWh for the renewable strategy) and a worst scenario (LCOE of 0.2717 euro/kWh). Other economic parameters such as Net Present Value, Pay Back Time and Internal Rate of Return are calculated to evaluate the profitability of the project.
Finally a last case in view of a future where incentives wouldn't be available anymore is considered, to understand if fuel-integration would be convenient or not. This analysis shows how the income increases with a higher hybridization, even though the profits remain negative.

1. Introduction

At the recent United Nations Climate Change Conference (COP21), held in Paris in December 2015, 196 countries agreed to reduce CO_2 emissions and to keep the global warming well below 2°C.
In November 2016 all the countries met again in Marrakesh for the COP22 to show their initiatives regarding the Paris Agreement. Today, 23.7% of the total world energy demand is supplied by renewable energy [1], while this share was of 2% in 1998. Many ambitious projects were announced, such as Morocco to aim at producing 52% of its energy from renewable resources within 2030, or Sweden to aim at 100% within 2020.
From now on, adherent countries will meet every five years to report on their emissions and "progress made in implementing and achieving" their nationally determined contributions. In 2020 (official begin of the pact) a fund of 100 billion dollars will be mobilized to help developing countries to go towards green technologies [2].
In the renewable power production area, a healthy competition among technologies (PV, wind, hydro-electric, tidal…) is leading to continuous improvements in efficiency and cost. The local conditions, the requirements of the utility, the maturity, the available subsidies and financing questions are the parameters that incline to one or the other technology.
Among the renewable alternatives solar energy emerges as one of the most promising sustainable options, and not only speaking about photovoltaic. In fact, PV might have a lower cost/kWh today but it doesn't allow to store the energy unless with very costly batteries. On the contrary, concentrated solar power (CSP) technologies with suitable heat transfer fluids (HTF) allowing storage of energy, entered the market during the last years and proved the reliability of concepts and components. Besides, the option of hybridizing the system, by adding a combustor in parallel to the solar heat allows to produce continuously the design power output, or even to boost it to higher values.
Among the CSP, there are significant technical distinctions in availability, dispatchability, scalability and footprint.
United Arab Emirates, China and many other countries are already investing huge amount of capital in this new "Solar Revolution" [1].

This thesis will investigate a particular system, belonging to the CSP world, which is characterized by a "Micro-Tower". A brief introduction will present the various CSP technologies available today and their probable future role, to give a context to this thesis.

Concentrated Solar Power

The primary source of heat for these system is the sun. The sun is a star that behaves as a black body at the temperature of 5777 K. Inside its core several nuclear reactions occur such has fusion reactions: process in which light molecules of hydrogen combine to form heavier molecules of helium. During the fusion the mass is converted into energy ($E=mc^2$). This energy is then transferred from the interior to the external surface by a succession of radiative and convective processes.
The sun irradiates to the Universe 3.8 x 10^{14} TW but due to the large distance (1.495 x 10^{11} meters) and the dimensions of the two bodies, only 172500 TW are intercepted by the Earth.
This amount of energy is defined by the solar constant, G=1367 W/m^2, which represent the mean value of thermal power received, outside the atmosphere, per unit area normal to the propagation direction.

The CSP technologies are based on the conversion of the direct component of solar radiation (DNI) into high temperature thermal energy and then into electricity, heat or mechanical work.

To obtain a higher level of energy per unit area, concentrators (mirrors or lens) are used.
Solar radiation is received by a collection surface A_c, and redirected onto an absorption surface A_{abs}. The ratio between these two surfaces is one of the most representative indicators of the system and is called concentration ratio CR.
Notice that CR maximum value depends on the type of concentrator: 2D line-focus concentrator (one axis tracking visible in Figure 1.2) or 3D point focus concentrator (2 axis tracking visible in Figure 1.3):

$$CR_{2D} = \frac{1}{\sin(\Psi_{\text{rim}})} \tag{1.1}$$

$$CR_{3D} = \frac{1}{\sin(\Psi_{\text{rim}})^2} \tag{1.2}$$

Where Ψ_{rim} is the rim angle of the concentrator, exposed in Figure 1.1, taken from [3].

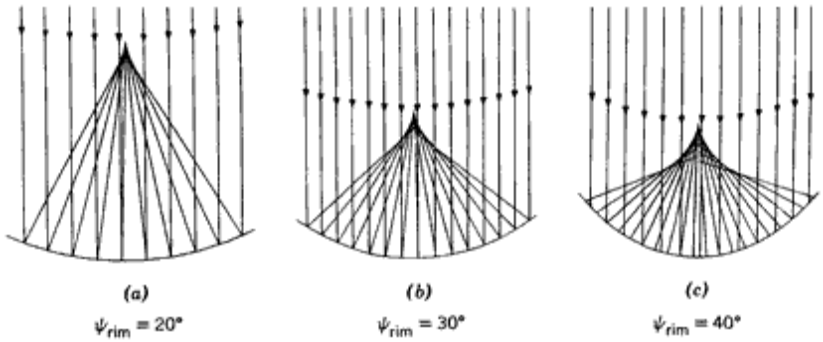

Figure 1.1 Sun's rays paths for three different concentrator's rim angle, taken from [3]

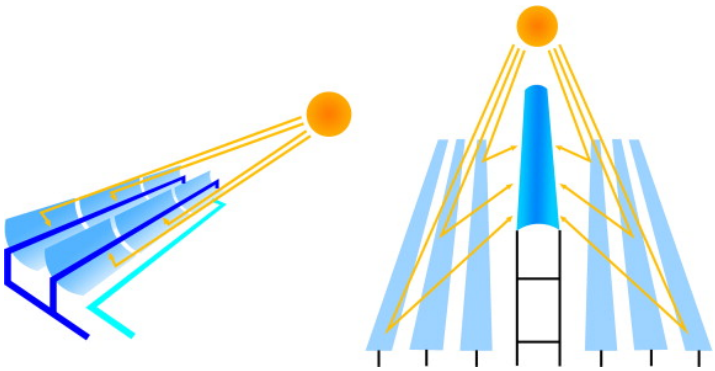

Figure 1.2 Scheme of single axis tracking systems: parabolic through (left) and Fresnel collector (right), taken from [4]

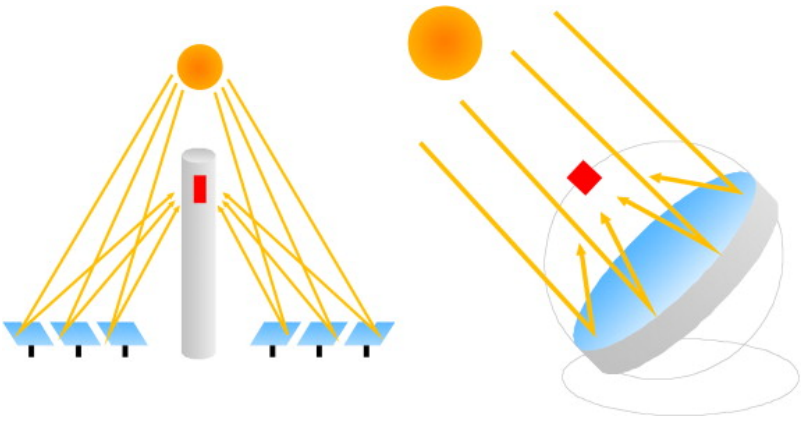

Figure 1.3 Scheme of double axis tracking systems: solar tower (left) and parabolic dish (right), taken from [4]

The coupling of the solar energy concentrating system and the thermal engine identifies a CSP plant. The global efficiency can be expressed as the product of the solar receiver efficiency and of the thermodynamic cycle efficiency as defined by the relation below:

$$\eta_{CSP} = \eta_{receiver} * \eta_{cycle} \quad (1.1)$$

To simplify the equation some assumptions must be done. The receiver is modeled as a cavity with a thermal behavior assimilated to a black body. Therefore, the receiver thermal losses are only radiative and no convective losses are considered. The thermal efficiency of the thermodynamic cycle is assumed to be equal to the ideal Carnot cycle efficiency, and to have a more realistic value a second-law efficiency (i.e. 65.0 %) can be considered.
The collection system receives and concentrates the solar radiation on an absorber where solar radiation is converted into thermal energy (typically increasing the enthalpy of a fluid used in a conventional power cycle). Concentrating solar power plants allow to exploit more efficiently the solar radiation, with respect to non concentrating systems, because of the higher temperatures reached by the working fluid. The absorber temperature is higher than the ambient temperature thus implying thermal losses to the environment.
The useful thermal energy is defined by the difference between the absorbed fraction of the concentrated solar energy and the thermal losses.
Once a steady condition is reached, the energy balance equation referred to the absorber surface can be written as follows:

$$\begin{aligned} Q_{receiver} &= Q_{absorbed} - Q_{rad} \\ &= \alpha * CR * DNI - \sigma * \varepsilon * ({T_{abs}}^4 - {T_{sky}}^4) \end{aligned} \quad (1.2)$$

Where α is the receiver absorptivity, representing the share of impinging solar energy that is converted in thermal energy, CR is the geometrical concentration ratio, DNI is the beam normal irradiance, σ is the Stefan-Boltzmann constant, ε is the thermal emissivity of the receiver, T_{abs} represents the absorber temperature and T_{sky} is the reference ambient temperature viewed by the receiver (both expressed in Kelvin degree).
The global efficiency can be expressed as it follows:

$$\begin{aligned} \eta_{CSP} &= \frac{Q_{receiver}}{Q_{concentrated}} * \eta_{carnot} * \eta_{II} \\ &= \left(\alpha - \frac{\sigma * \varepsilon * \left({T_{abs}}^4 - {T_{sky}}^4\right)}{CR * DNI}\right) * \left(1 - \frac{T_{amb}}{T_{abs}}\right) * \eta_{II} \end{aligned} \quad (1.3)$$

Therefore, the total efficiency presents an optimum that depends on the temperature and the CR, shown in Figure 1.4.

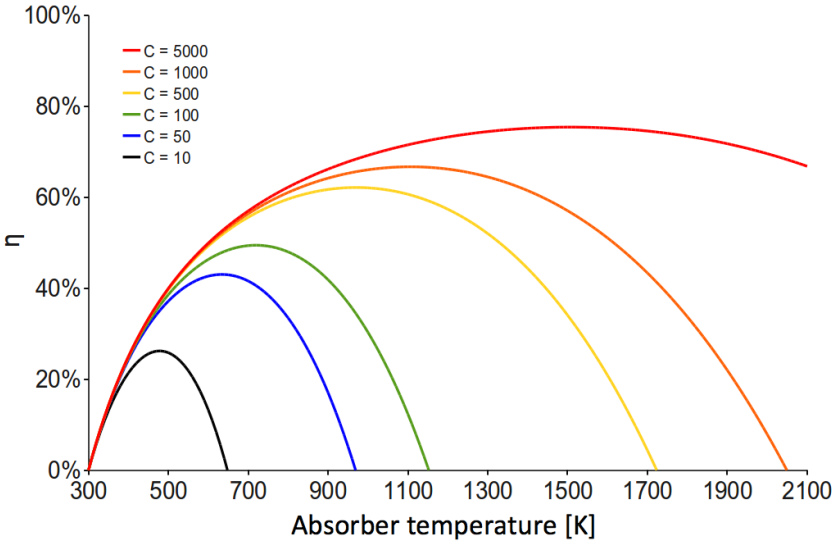

Figure 1.4 Cycle efficiency for different CR

A thermal solar power plant consists of a number of subsystems: the collector/concentrator, the receiver/absorber, the power converter, often the heat storage and the conventional burner/boiler in case of hybridization of the system.

1.1 Parabolic Dish

A solar parabolic dish system is composed by:

- A parabolic dish that tracks the Sun by a rotational movement along two orthogonal axes and concentrates the solar radiation on a receiver set at the focal point (supported above the center of the dish).
- A thermal engine placed at the top of the receiver that uses a working fluid heated by the concentrated radiation.

Parabolic dishes are characterized by the highest solar to electric efficiency among the CSP technologies (up to 31.25%), high modularity and autonomy, inherent hybridization but until now show reliability problems, related to the receiver/engine block working at very high temperature, and high costs that have obstructed their entry in the power generation market. Moreover they are not compatible with thermal storage; and from the economical point of view no scale effect is applicable.

The parabolic dish can be made by discrete elements (facets) that approximate the geometry of a paraboloid or by a continuous metallic membrane that approximates the ideal geometry. With this particular geometry, it is possible to reach a concentration ratio CR of almost 3000, what means very high temperature on the absorber. For example a 17 m diameter dish is able to supply 46 kWe in presence of a solar flux of 1000 W/m^2, bringing the fluid up to 1760°C [5].

The power system is a thermal engine, most of the times a Stirling reciprocating engine or a Brayton cycle gas turbine.
The first pilot plant was the Solar Total Energy Project built in 1982 in Georgia (USA) [6].
According to Ripasso Energy, a Swedish firm, in 2015 its Dish Stirling system being tested in the Kalahari Desert in South Africa showed 34% efficiency, generating about 80 MWhe a year [7].

Figure 1.5 Ripasso Parabolic Dish, in Kalahari Desert, taken from [8]

1.2 Parabolic Trough Collectors

The parabolic trough technology is the one that has reached the highest level of commercial maturity. These plants use linear parabolic concentrators that track the Sun, rotating on a single axis, and focus the radiation on a receiver tube that runs along the focal line, hence transferring heat to a thermal fluid that flows inside the trough. This fluid is then used as thermal input in a steam generator as in traditional plants. Parabolic collectors usually have concentrating ratio CR up to 90, and the annual average solar-to-electricity conversion efficiency is about 15% for current designs.
The collector consists of a group of curved reflectors, supported by a steel structure that keeps them in the correct position even under wind or other atmospheric loads. The reflecting surface is a common glass mirror with proper curvature and low iron content on its surface to improve its transmittance.
The receiver is a metal tube with evacuated glass covering, mounted along the focal line of the linear array. A coated glass pipe encloses a black metal pipe to limit heat loss by convection and to allow transmissivity. The metal tube is covered with selective coating to increase solar absorbance (> 90%) and reduce emittance (< 30%).

The heat transfer fluid can be: synthetic oils, mineral oils, molten salts, water, ionic liquids, air or other gases. If the temperatures desired are moderate (< 200°C), demineralized water might be the best choice but, nowadays, the main working fluid is synthetic oil thanks to its low vapor pressure, that allows working at modest pressure and with economic materials reaching 400°C. Direct steam generators can reach 550°C but presents technical challenges due to the high pressure involved in boiling.
The low efficiency of this technology is due to different types of losses such as: shadow losses (between a parabolic mirror and another), no interception (due to single axis rotation), optical losses and thermal losses (conductive, convective and radiative losses of the absorber).
Solar Energy Generating Stations (SEGS) were the first commercial plants. They were built in California between 1981 and 1991 with a today-capacity of 354 MW. This is still the largest PT plant in the world, and the second largest CSP plant.

Figure 1.6 SEGS Parabolic Through, California, taken from [9]

1.3 Linear Fresnel Reflectors

A linear Fresnel collector employs flat mirrors simulating a continuous surface to collect and concentrate solar energy, therefore reducing construction problems and costs. Concentration ratio CR reach 160, but the solar to electric efficiency is lower than the one of parabolic through and thermal storages are difficult to install.
The system consists of:

- Long parallel rows of mirrors that can rotate around their longitudinal axis and concentrate solar radiation on a linear receiver that is suspended at a certain height above the mirror plane. A geometry of this type allows to dispose two or more receivers in parallel in order to have a single

receiver shared by a number of mirrors, optimizing the land use and minimizing mirror blocks.
- The absorbing pipe that is, essentially, the same used in parabolic trough systems.

Good exploitation of land, lightness, simplicity of construction and low cost, since the receiver is fixed and a higher pressure is allowed.
The first LFR prototype was installed in Liege in 2009.
The largest plant today is Puerto Errado 2, built in 2012 in the region of Murcia (Spain). Its capacity is of 30 MW, covering a mirror surface of 302,000 m^2.

Figure 1.7 Puerto Errado 2 Linear Fresnel, Spain, taken from [10]

1.4 Solar tower

Solar towers concentrate solar radiation in three dimensions (in a point) and for this reason they can reach the high concentrating ratios (up to 3000). The main components of a tower plant are: the heliostats field, the tower, the receiver and the power block.
The heliostat field is the most characteristic component of this kind of plants and constitutes about 50% of the total cost. Each heliostat (usually flat or slightly concave mirror) is formed by: a Reflective surface (for example glass mirrors or reflective surface containing polymeric film with high reflectivity), a Supporting structure, a Tracking system, a Control system.
The heliostat distribution on the ground needs to consider: shadows created among neighbor heliostats, radiation blocking by the heliostat placed ahead, tower height and land costs. This optimization process (technical and economical) brings to a "heliostat field" that can be:
- North field (South for the southern hemisphere): used for high latitude (as Europe)
- Circular field: used in low latitude where the sun stays high most of the day

The tower, whether made of metal or concrete, has the function of supporting the receiver that must be placed at a certain height above the heliostat field, in order to reduce shadowing and blocking losses.
The receiver, instead, is the device where the concentrated solar radiation is converted into thermal energy. During the short story of central receiver technology very different types have been proposed, designed, tested and built. Differentiating them for the working fluid: water (PS10), air (Phoebus-TSA), molten salts (Solar Two) or molten sodium (SSPS ASR).
Another differentiation is between: external tubular, cavity tubular and volumetric receivers (a more detailed analysis is done in *Chapter 5*).

The high concentrating ratio allows this technology to reach high working temperatures, bringing the use of gas as the working fluid very interesting. In this case, a volumetric receiver pressurized at 1.5 MPa can increase the gas temperature up to 1000°C (with metallic absorber) or 1500°C (with Silica carbide absorber).
The first solar tower commercial plant was the Planta Solar (PS10) in Spain. It began operation in 2007, designed to produce 24 GWh. The largest tower (and CSP) plant today is the Ivanpah Solar Power Generating Station, its operations started at the beginning of 2014. This plant consists of three units for a total installed capacity of 392 MW.
Latest solar tower constructed was Khi Solar One, located in the Northern Cape Region of South Africa. Constructed in February 2016 it is the first solar tower plant in Africa. It produces 50 MW, and covers an area of 140 hectares.

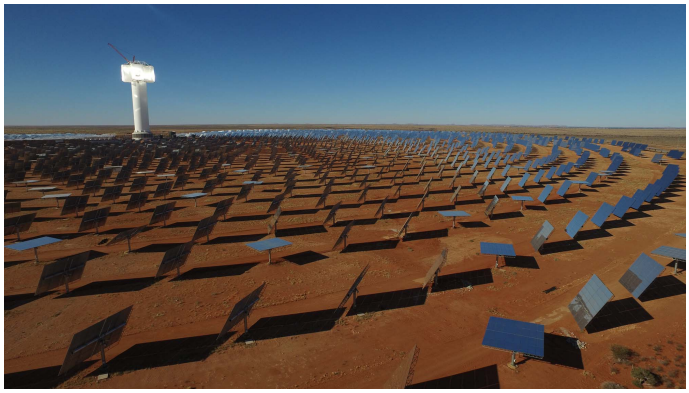

Figure 1.8 Khi Solar One Solar Tower, South Africa, taken from [11]

Evolution of CSP plants

Figure 1.9 shows the world map, highlighting countries/areas active in CSP world. It is possible to see the current plants operational today (in blue in the histograms), the ones under construction (in red) and the ones that have been announced (in green).

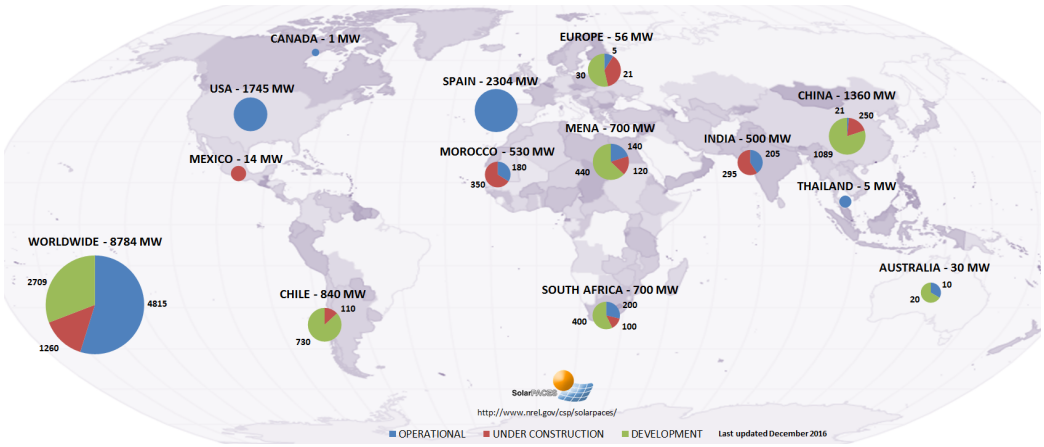

Figure 1.9 Operational, Under-construction and Announced CSP plants in the world; from [12]

Focusing on the Italian case, only three CSP plants exist:

- Archimede (built in 2010 by ENEL) which is a parabolic trough plant operating in Sicily. The plant produces steam (4.72 MW equivalent) sent to a combined-cycle steam turbine rated at 130 MW.
- ASE Demo Plant (built in 2013 by Archimede Solar Energy) which is a parabolic trough plant operating in Umbria. The plant produces steam (0.35 MW equivalent).
- Rende-CSP Plant (built in 2014 by Falck Renewables) which is a linear fresnel plant operating in Calabria. The plant produces steam (1 MW equivalent).

As it can be seen, no solar-towers are present in Italy nor planned. Besides the only plants under-construction (six today among Sicily and Sardinia) all regard parabolic through of 30/50 MW [13].
Thus, this thesis will investigate a solar tower plant, belonging to the microgeneration (kW).

Thermodynamic cycles

1.5 Steam Rankine Cycles

Steam turbines work in a closed-cycle. The cycle is mainly constituted by:

- Transformation in isobar conditions at high pressure, where water heats up (at temperatures between 500 and 650°C) and evaporates.
- Expansion until a low pressure is reached, producing useful work.
- Transformation in isobar and isothermal conditions in which water goes back to its liquid state, in a condenser.
- Compression to bring water at its initial pressure.

In the first transformation, the heat is obtained through a thermodynamic cycle, where the water never gets directly in contact with the fuel/hot source. Major problems of steam turbines are:

- The heat exchanged to heat the liquid is introduced in the cycle at a low mean temperature, influencing negatively the yield.
- During the expansion the fluid remains inside the transition curve, producing the formation of water droplets, having a bad impact on the turbine blades (erosion due to the higher density of the liquid, reducing the lifetime of the turbine) and on the yield.
- High temperatures are not reachable because higher temperatures induce higher pressure and the problems previously explained increase. Moreover in a close cycle maximum temperature of the fluid can't exceed the one of the heat-exchanger material, adding a limit on it.
- Starting a steam turbine takes time (slowly preheating is required to avoid mechanical problems).

A steam turbine itself is very efficient, the energy losses in a steam power plant occur elsewhere mostly (in the condenser / cooling tower or electric generator). Once a steam turbine is in operation its load can be varied without influencing the efficiency too much (within limits).

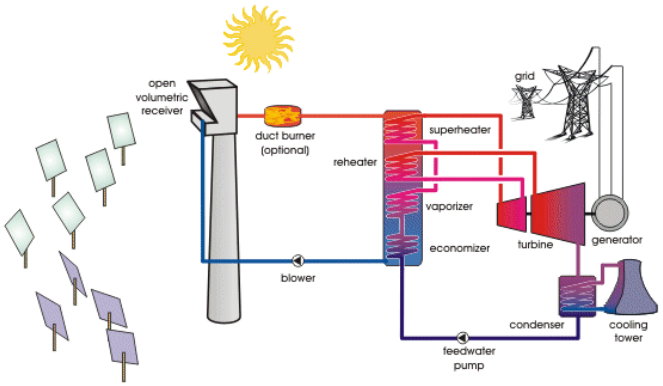

Figure 1.10 Solar Steam Turbine Configuration, taken from [14]

1.6 Joule-Brayton

Gas turbines refer to the conceptual Brayton open-cycle, which is composed by the following gas transformations:

- An adiabatic compression with inlet air at ambient conditions.
- A heating at constant pressure in which air gets in direct contact with the hot source. In this way the maximum operative temperatures are higher (up to 1500°C).
- An adiabatic expansion.
- A release of heat by air-dispersion in the ambient.

In this way no heat exchanger are required, so land occupation and costs are reduced. The biggest advantage of gas turbines is their flexibility, giving a

lot of performance whenever it is needed. Steam turbines take time to start so you have to run inefficiently in order to provide the same flexibility gas turbines do.
The efficiency of a gas turbine is determined by the combustion temperature. The exhaust gas is usually still hot, reducing the efficiency of the cycle, for this reason a bottom cycle is often implemented.
Gas turbines are rather more expensive to make because the turbine blades (especially in the first stages) need to be made of exotic alloys that can withstand the very high temperatures.
Gas turbines are very versatile and can operate directly or indirectly fired. This fact makes them especially suitable for their integration in concentrated central tower thermosolar plants. Solar gas turbine systems use concentrated solar power to heat the pressurized air in a gas turbine before entering the combustion chamber. The solar heat can therefore be converted with the high thermal efficiency of a modern recuperated or combined gas turbine cycle. The combustion chamber closes the temperature gap between the receiver outlet temperature (800-1000 °C at design point) and the turbine inlet temperature (950-1300 °C) and provides constant turbine inlet conditions despite fluctuating solar input. The solar power tower technology is used to have high concentration ratios in order to achieve the high receiver temperatures.

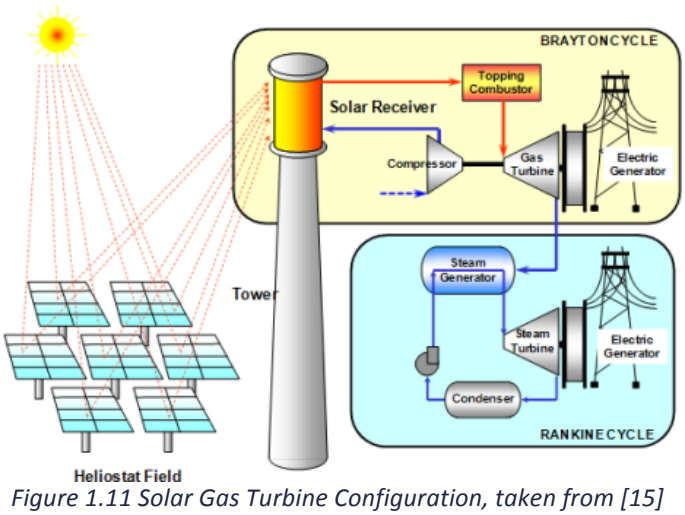

Figure 1.11 Solar Gas Turbine Configuration, taken from [15]

A solar tower coupled with a solar tower (in a Brayton cycle), and with fuel integration presents clear advantages:
- Full dispatchability and grid stability through flexibility and instant regulation of the additional fuel flow.
- High achievable power outputs.
- Fast start up of the gas turbine.
- Low to zero water consumption.

- Air as cheap and ‘‘harmless” heat transfer fluid (no freezing, no overheating).
- A wide range of plant concepts are feasible: independent recuperated Brayton cycle, peaking plants and especially combined cycle with or without thermal energy storage.
- Cycle efficiencies higher than 50% in solarized combined cycle configuration are possible.

Thus, this thesis will investigate this final interesting configuration in order to provide reliable power with variable solar share. Moreover, even if not included here, it can be noticed that fuels from renewable sources could also be used, such as biogas or solar fuels, making possibly this technology 100% sustainable.
Most of the existing plants require very large areas (e.g. PS10), producing power outputs in the range of MWe while this project will aim at a power output around 200 kWe (by the use of a micro gas turbine), thus requiring small areas.
For the solar hybrid Brayton cycle, the two key components to be developed are the solar receiver and the adapted gas turbine.
A large fraction of the thermal power required by the gas turbine should be provided by solar energy to achieve a reasonable solar share, ideally up to 100%, for this research at least 75% in order to access Italian subsidies. On the other hand, the efficiency of the Brayton cycle rises with higher operation temperatures and pressures. Consequently, to become viable the solar receiver developments need to focus on conditions with high material requirements to reach outlet temperatures of 1000°C (a modern molten salt solar plant for example operates at up to 580 C). Furthermore, the low heat capacity and thermal conductivity of compressed air compared with other HTFs, makes necessary to think of design concepts which still allow high thermal receiver efficiencies.
The gas turbines main challenges are the substantial changes to accept the externally heated gas flow from the solar receiver and the combustion chamber modifications. High requirements on air flow control are a consequence of the introduction of a solar receiver and a larger air volume in the ducting between compressor and turbine. The combustor needs to operate at significantly higher and varying air inlet temperatures and must react fast enough to ensure stable gas turbine operation during solar fluctuations.

Solar towers coupled with micro-gas-turbines

Since this thesis will investigate a CSP solar tower coupled with a recuperated micro-gas turbine, it is interesting to present the existing plants that adopt this technology. Today, only four towers with design power output lower than 1 MW_e exist [13] and none of them operate for commercial purpose. In fact, they are all for research.

Aora company [16] built its first micro-tower in 2009 in Samar (Israel) and another one in 2012 in Almeria (Spain), both with a design output of 100 kWe. The turbine (on top of 33 meters tulip tower) produces electricity thanks to solar energy and to the combustor that allows hybridization.

Figure 1.12 Aora plant in Spain

Another company investing in this field is Daesung Energy [17], who built its only tower in 2009 in Daegu (South Korea), with a design output of 200 kWe. The tower is 50 meters high and there are 450 heliostats in the field.

Figure 1.13 Daesung Energy plant in South Korea

The last micro-tower was built in 2010 and is situated in Abu Dhabi [18]. This 100 kWe turbine with its 33 heliostats is sponsored by the Tokyo Institute of Technology, Cosmo Oil and Masdar. The configuration of this latter plant is different from all the previous one, since it uses the "Beam Down Mode", meaning that the system reflects sunlight twice, once from the heliostats to the central tower and once from the tower down to a collection platform at the system's base. The main advantage of this configuration is that all major equipments are at ground level (including the receiver), so that

installation, maintenance and operations are easier. On the contrary, the most important challenges regard the additional the hyperboloid mirror and its additional reflection losses.

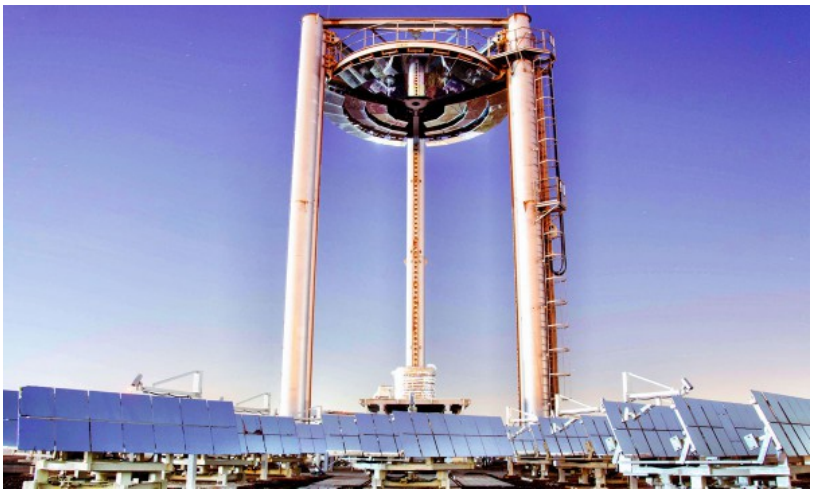

Figure 1.14 Beam Down tower in Abu Dhabi

2. Methodology

The project purpose is to develop a model for the simulation of a small tower system coupled with a micro-gas-turbine. The turbine works in a Brayton cycle and the highest temperature at which the fluid (air) heats up is 950°C (upper limit allowing the use of metal blades, and not cooled or ceramic ones [19]). Brayton cycle is a well-known-technology with a consolidated experience in the gas turbine field; this is the key to the coupling with the tower system.

2.1 Main objectives

In parallel, models for the sizing and for the calculation of performances of the various macro-components of the system (heliostats, receiver and power block) are developed.

The initial field of heliostats is taken from the existing plant of Aora in Almeria (Spain). Coordinates of the heliostats and of the tower are extracted from Google Earth [20], and they are kept fixed for all the simulations.

An on design analysis helps at optimizing the components in terms of several characteristics, therefore defining the best plant configuration.
On the other side, due to the random and somewhat unpredictable nature of the primary energy source exploited by the power plant, these facilities are subjected to extremely variable working conditions.
Therefore an off design analysis is also investigated to react in the best possible way to changes of the external conditions.
For the cycle modeling, a code implemented in Politecnico di Milano for a parabolic trough plant [21] was taken, and adapted to this project conditions.
To improve the flexibility of the plant the integration of fossil fuel was implemented (not present in the initial code), considering the limit imposed by the Italian Law [22] to receive renewable-incentives (equivalent to an annual fuel fraction equal or lower than 15%).

2.2 Software choices

To develop the analysis of the power-block, MATLAB R2016b [23] is used with the integration of the REFPROP program [24] (to calculate properties of pure substances and mixtures).
MATLAB is a high-level technical computing language and interactive environment for algorithm development, data visualization, data analysis, and numeric computation, first developed in 1984.
The essential characteristics that make this software suitable for the modeling of a solar tower power plant are its capability in managing non-linear equations systems and its stability in working with multi-variables iterative processes (essential to solve the system working points). Moreover, the huge diffusion of this tool both in the Academic and in the Industrial Research Centers will allow a

large number of hypothetical users of the model to run it and to eventually manage and modify it.
REFPROP is a software that computes fluid thermodynamic properties such as temperature, enthalpy, entropy, heating values.

To develop the analysis of the solar field, SOLTRACE [25] is used for the simulations, while MATLAB and EXCEL are exploited to re-elaborate the obtained results.
SolTrace began its development at the National Renewable Energy Laboratory (NREL) in early 2003. It is an optical simulation tool designed to model optical systems used in concentrating solar power (CSP) applications. It can model virtually any optical system utilizing the sun as the source.
The code utilizes a Monte Carlo ray-tracing methodology from the sun through the system, encountering various optical interactions. The user can select the number of rays to be traced through the system, knowing that a higher number of rays launched induces a longer processing time and a more accurate result. This value depends on the detail needed in the results. In general, ray numbers on the order of one million are required for good accuracy.
The screenshot of the interface of the software can be seen in Figure 2.1.

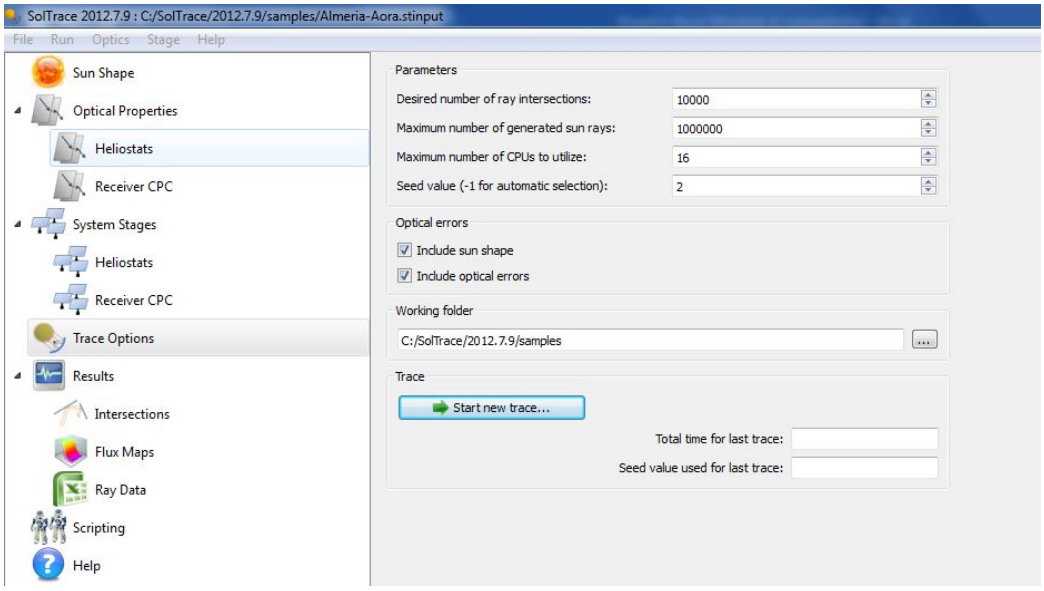

Figure 2.1 SolTrace software interface

2.3 Resume methodology diagram

To resume all the steps used to arrive to this project final results, a flow diagram is presented in Figure 2.2.

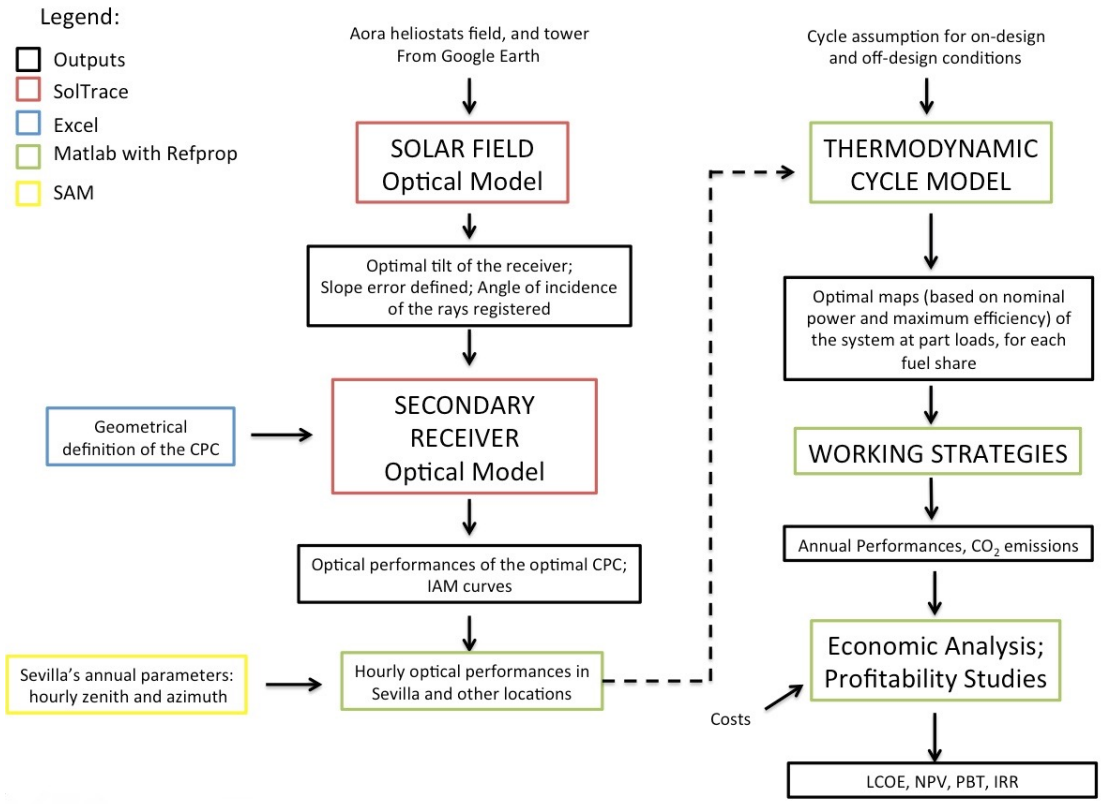

Figure 2.2 Flow diagram to resume the adopted methodology

3. Collector subsystem

The collector subsystem for a solar central receiver is responsible for the interception, redirection, and concentration of direct solar radiation to the receiver, located on the top of the tower. The collector subsystem consists of a field of tracking mirrors, called heliostats, and a tracking control system to maintain the direct solar radiation continuously focused on the receiver while energy is being collected.

3.1 Basic optics and performances

Solar concentrators follow the basic principles of Snell's law of reflection: in a specular surface the reflection angle equals the angle of incidence. Nevertheless, in real mirrors with intrinsic and constructional errors, the reflected ray distribution is better described with "cone optics" and the error associated to the reflected ray direction takes the shape of a normal distribution function.
The errors of a typical reflecting solar concentrator may be either microscopic or macroscopic (Figure 3.1). Specularity errors are the one associated to the microscopic roughness of the heliostat, while slope errors are the one associated with the macroscopic shape of the heliostats (they occur when the mirror is not perfectly flat, but slightly curved).

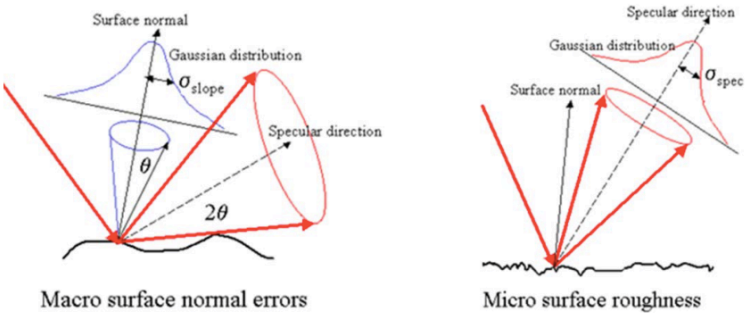

Figure 3.1 Effects of normally distributed slope and specularity errors on reflected ray direction, taken from [25]

The total error is given by:

$$\sigma_{optical} = (4\sigma_{slope}{}^2 + \sigma_{specularity}{}^2)^{1/2} \quad (3.1)$$

This ends up modifying the direction of the normal compared to the reference reflecting element, but it is useful to discriminate between microscopic and macroscopic errors. Microscopic errors are indeed intrinsic to the material; they depend on the fabrication process, and can be measured at the lab with mirror samples. Macroscopic errors are instead characteristic of the concentrator and of

the erection process. They should therefore be measured and quantified with the final system in operation.
The consequence of the errors from the sun, tracking system and reflecting surface, leads to the fact that the spot and energy profile obtained on a flat absorber can be approximated to a Gaussian shape, as shown in *Figure 3.2*.

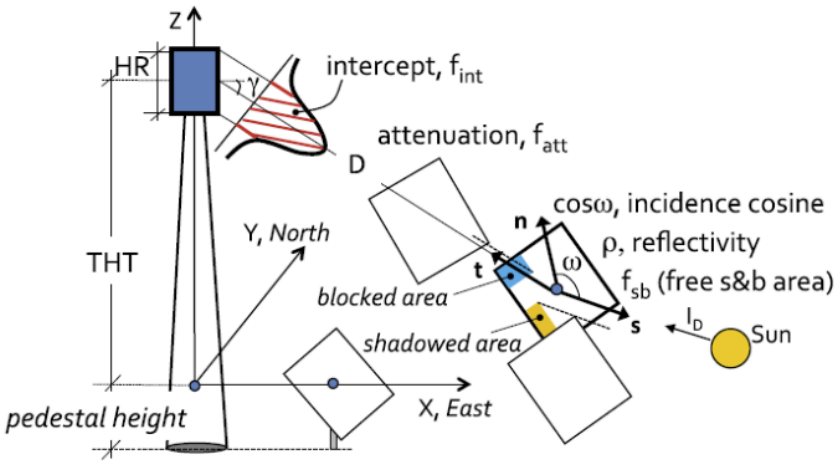

Figure 3.2 Gaussian shape of energy profile due to various effects, taken from [26]

The performance of the heliostat field is defined in terms of the optical efficiency, which is equal to the ratio of the net power intercepted by the receiver to the product of the direct insolation and the total mirror area.
In addition to these effects, characteristics of the specific sun-heliostat-receiver interaction, other losses must be considered to properly describe the performance of a heliostat field and are described subsequently.

3.1.1 Cosine effect

The amount of insolation reflected by the heliostat is proportional to the amount of sunlight intercepted. The reflected power is proportional to the cosine of the angle (cosine effect) between the heliostat mirror normal and the incident sun rays; the ratio of the projected mirror area that is perpendicular to the solar beams over the total area of the heliostat determines the magnitude of the cosine effect.
The heliostat is oriented so that the incident sunlight is reflected onto the receiver (Figure 3.3). If the sun is due south and low in the sky, as it is in winter, then the heliostats due north of the tower will be almost perpendicular to the sun's rays and, therefore, have almost the maximum cosine efficiency of 1.0. At the same time, heliostats due south of the tower will have a low cosine efficiency. Since the greatest fraction of the annual insolation occurs when the sun is in the southern sky, the annual average cosine will be greatest in the northern part of the heliostat field. Thus, in the northern hemisphere, heliostat fields are usually biased toward the north of the tower.

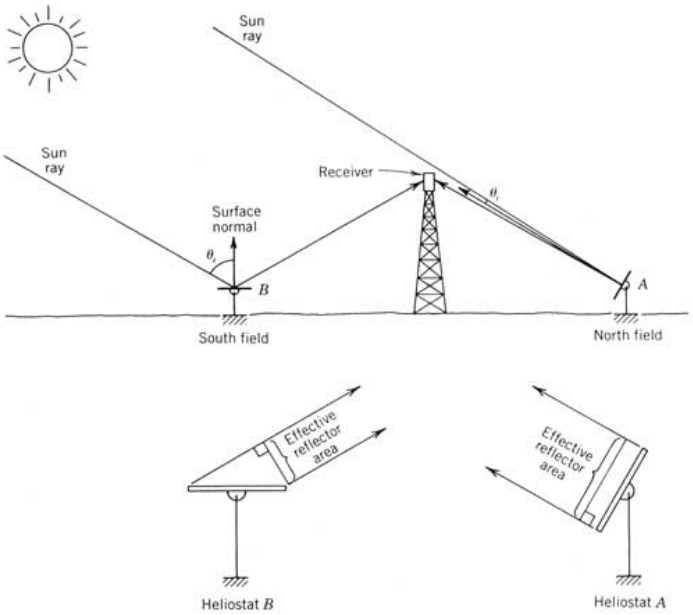

Figure 3.3 Cosine effect for two different inclinations of heliostat, taken from [3]

3.1.2 Blocking and Shadowing effects

Blocking of reflected rays is also an important limitation on spacing heliostats. Blocking is produced by heliostats neighbors (the backside of a heliostat receives a ray coming from the heliostat behind). To avoid blocking losses, the distance between the heliostat rows must be calculated properly.

Shadowing produced by neighboring heliostats also has to be taken into account. This occurs mostly at low sun angles and in the middle of the field where blocking conditions would allow close spacing. The shadows move during the day and year, as does the heliostat orientation, so there is no simple rule.

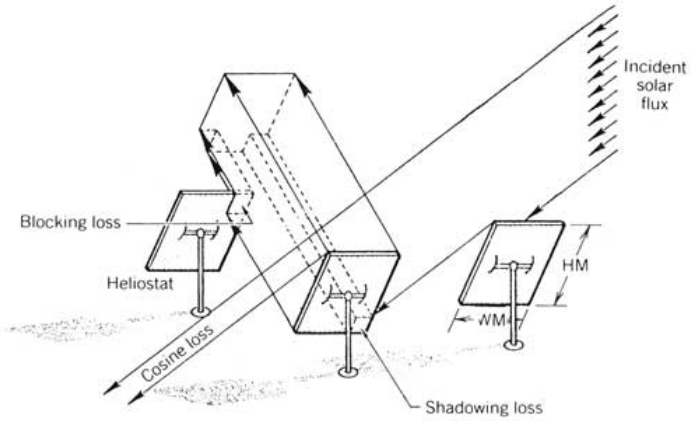

Figure 3.4 Blocking and shadowing effects, taken from [3]

3.1.3 Intercept factor

The intercept factor (also called spillage) represents the ratio between the energy intercepted by the receiver to the one reflected by the focusing design (heliostats). The parameters affecting the intercept factors are: the curvature of the heliostats, the aiming point of the heliostats, the shape, the size and the position of the receiver.

3.1.4 Mirror reflectivity

The heliostats do not reflect the whole solar radiation that impinges their surface because part of this radiation is absorbed by the glass. The ratio between the incoming and the reflected radiation is called reflectivity and depends on the radiation wave length. To quantify this factor, a mean value for the whole solar spectrum is normally used. It has to be noticed that the mirror cleanliness influences the reflectivity value.

3.1.5 Atmospheric attenuation

Not all the sunlight that leaves the heliostats reaches the vicinity of the receiver. Some of the energy is scattered and absorbed by the atmosphere; this effect is referred to as the attenuation loss. In a day with good visibility, this effect will have a small percentage of energy loss per kilometer. The losses increase when water vapor or aerosol content in the atmosphere is high.

3.2 Field layout

The heliostat field is a very important subsystem of a solar tower power plant and it contributes about 50% to the total cost [27]. From this, the attention paid on the disposition of the different heliostats has been remarkable in the last 30 years, with the development of several different approaches and methods.
The first big differentiation of a solar field is between a north and a surround configuration.
In a surround field configuration, heliostats are arranged around a centrally located tower. In the north field configuration (or for plants located in the southern hemisphere, a south field configuration), instead, all heliostats are arranged on the north side of the tower. Talking about the north-field or surround configuration, the main factor that affects whether choose one or the other is the cosine effect.
Representative collector fields are shown in *Figure* 3.5 and *Figure* 3.6 for surround and north-side fields, respectively.

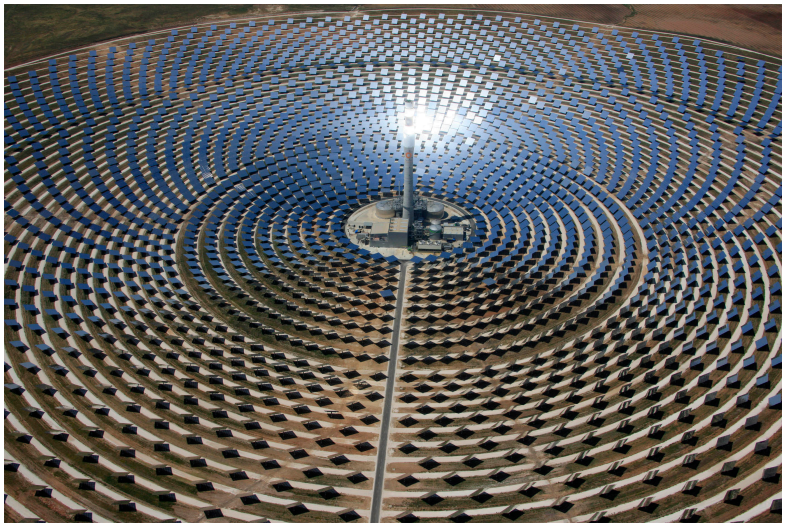

Figure 3.5 Surrounded field configuration (Gemasolar Plant in Almeria)

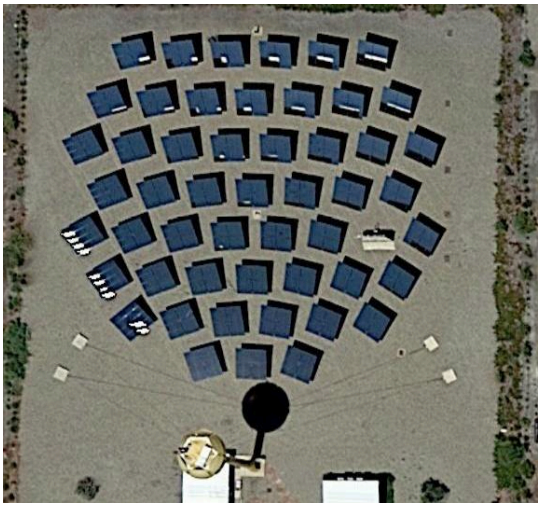

Figure 3.6 North field configuration (Aora plant in Almeria), taken from [20]

In this analysis, the Aora active site near Sevilla was taken as the starting point. This tower, known as the "Solar Tulip" was switched on the first time in 2012, and designed to produce 100kW$_e$ thanks to a micro-gas-turbine. The North-field was reproduced in its disposition and dimensions.

Heliostats

Heliostats are the first elements of the system to interact with the solar radiation. They consist in a mirror mounted on a dual axis tracker (which allows for movement about the azimuth and elevation axis) by which a sunray is steadily reflected in one direction. A fractional-horsepower motor through a gearbox drive gives the motion of the heliostat. This mirror is almost flat; a small curvature is required in order to focus the sun's image. It collects and concentrates the solar energy on the tower-mounted receiver. The surface on a heliostat is typically a thin, back-reflecting surface in a low-iron mirror. Large heliostats are normally composed of many mirror modules rather than a single large mirror.

Heliostats field optimization is a complex and time-consuming task. The optimization mainly concentrates on the distance between mirrors to maximize the field annual thermal performance. Deciding to focus the researches on the optical performances due to receiver's various configurations, as previously said, dimensions and position of heliostats are taken from the Aora field (supposed to be already optimized) located in Almeria (near Sevilla), throught Google Earth [20]. The 52 squared-mirrors are characterized by a 4 meter-side (composed by four modules of 1 meter), which sums up to 832 m^2 reflecting area for the field. The distance between the centers of two heliostats in the same row is 6.3 meters, while the distance between two rows is 5.6 meters.
Moreover, since the mirrors are slightly concaves, tilt angle for a specific mirror changes according to its position in the field (radial distances to the tower). The layout of the field is visible in Figure 1.12.

The geometrical definition of the tilt angle (n in *Figure* 3.7) of a single heliostat is a function of the tower height, of its distance from the tower and of the incidence angle of the sun.

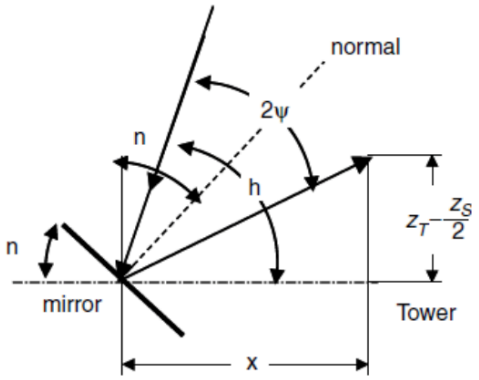

Figure 3.7 Geometrical definition of elevation angle n

A script in SolTrace is written in order to vary n for each incidence angle of the sun (defined by a zenith and azimuth angle). The tracking movement of the heliostats is represented by the rotation defined by the matrix R^4 (in 3D space), function of zenith ϑ_{ZS} and azimuth Ψ_S:

$$R = \begin{bmatrix} \cos(\Psi_S) & -\cos(\vartheta_{ZS}) * \sin(\Psi_S) & \sin(\vartheta_{ZS}) * \sin(\Psi_S) \\ \sin(\Psi_S) & \cos(\vartheta_{ZS}) * \cos(\Psi_S) & -\sin(\vartheta_{ZS}) * \cos(\Psi_S) \\ 0 & \sin(\vartheta_{ZS}) & \cos(\vartheta_{ZS}) \end{bmatrix} \quad (3.2)$$

Regarding optical properties of the heliostats stage:

- reflectivity of the mirrors is set equal to 0.94, conceivable with reflecting surfaces made of silver back-coated low-iron glass

- slope error is set to 1.5 mrad, specularity error is set to 0,0001 mrad inducing a total optical error of 3 mrad.

NB: a sensible analysis is then performed to show the weight of the slope error setting in *Section 4.3*.

3.3 SolTrace input

Before entering the stage of the heliostats in SolTrace, first input is the light source. There are two options for defining the sun position. First option is to define a point in the global coordinate system (x, y, z) such that a vector from this point to the global coordinate system origin defines the sun direction. The second option is to define a particular site latitude and time (day of year and local solar hour).

In the case where the element geometry depends on sun position (e.g., the heliostat in the tower geometry), the user must determine element aim points. These equations are based on solar time and come from the spherical geometric relationship of the earth and sun, and they do not account for longitude, eccentricity of the earth's orbit, or impacts due to atmospheric effects.

Three options are available for the sun shape (to represent the flux intensity) as it can be seen in *Figure 3.8*. The first two are probabilistic distributions.
-Gaussian distribution
-Pillbox constant distribution
-User defined distribution

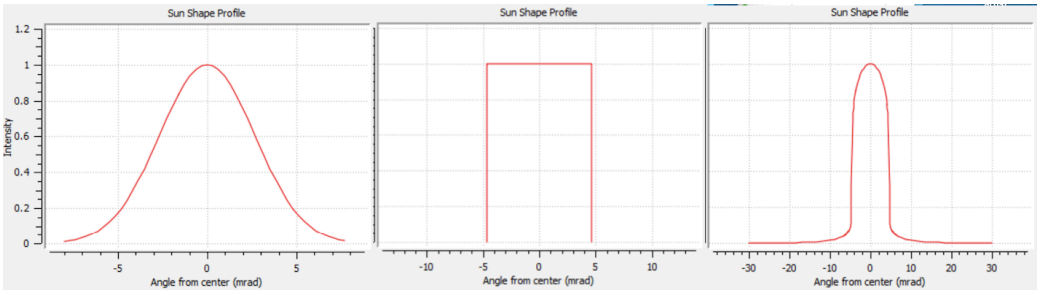

Figure 3.8 Gaussian, pillbox and user-defined measured sun shapes

For highly accurate systems, the use of a Gaussian sun is not recommended unless the system includes relatively large optical errors (either based on geometry or optical property definitions). The parameter defining a Gaussian distribution for the sun's disk is the standard deviation, σ. The parameter for the pillbox, being a flat distribution, is simply the half-angle width. The third option allows the user to define the sun shape profile as a series of intensity datum points; using profiles already defined, based on Neumann's work. These profiles represent the shape of the solar cone for various attenuations of the solar disc. They are defined with the initials CRSx. Where x represents the percentage of the attenuation as in equation *(3.3)*.

$$CRS = \frac{I_{cs}}{I_{cs} + I_{sun}} \tag{3.3}$$

For the following cases the sun was positioned at height of 100 meters (absolute reference) with a CRS10 sun configuration, defined by 50 points.

After having defined the light source, the various stages must be computed.
Only the first stage of an optical system "sees" the sun. That is, rays are traced from the sun only to the first stage, omitting other stages regardless of their spatial arrangement. Subsequent stages only "see" the rays that come from the previous stage. It is important to know this for shading purposes. In general, if it is possible and reasonable to define all optical elements in the first stage, then it is most accurate to do so. Individual optical elements within a stage can have either reflective or refractive optical properties.

In these simulations first stage is defined as the heliostat field (composed by 52 elements, each of them representing a heliostat). Second stage is defined as the tower receiver (composed by one element in case of a simple flat receiver, and of more elements for other configurations).
Optical properties are defined for each element, specifying front and back sides of a surface. For example reflectivity of the heliostats is set equal to 0.94 as suggested by [28]; to keep this value during the lifetime of the plant, heliostats must be maintained properly since actual reflectivity can fall to low values due to fouling.

4. Optical analysis of the simple receiver

Now that the heliostats field is defined, a brief introduction must be done on the tower itself. Indeed, the tower is 33 meters high; composed by a structural column made of grey galvanized steel and a two-levels (6 meters total high) mechanical space containing the thermal engine, the generator and the receiver.
The receiver must be tailored to a matching heliostat field layout. This means that the field of heliostats must be circumscribed within the view cone of the receiver's geometry because only the heliostats situated inside these boundaries will give useful contribution to the receiver. Since in this case, the starting point is the heliostats field, the receiver must be designed accordingly.

4.1 Optimal tilt

This analysis is first done at Solar Noon of equinox days in Sevilla (March 21 and September 21), as it can be considered as an "average" day in the year. Sun's position is given by (*4.1)*; and then evaluated for other days.

$$\Psi_S = 180 \tag{4.1}$$

$$\vartheta_{ZS} = 90 - Latitude \tag{4.2}$$

A flat surface with a defined area (circle of 1 meter diameter) is set as the receiver. In the simulations, real conditions are tested since optical errors accounting for sun shape and heliostats are considered.
Thus the tilt angle of this surface is changed from 0° to 90° with a step of 5°. For each tilt angle the optical yield is calculated directly in a SolTrace script with the following formula:

$$\eta_{opt} = \frac{N_{rays-r} * P_{ray}}{G * N_{hel} * A_{hel}} \tag{4.3}$$

Where:
$N_{rays\text{-}r}$ is the number of rays hitting the receiver;
P_{ray} is the power of the single ray;
G is the sun's irradiance (set as 1000 [W/m^2]);
N_{hel} is the number of heliostats (52);
A_{hel} is the area of the single heliostat (16 [m^2]);

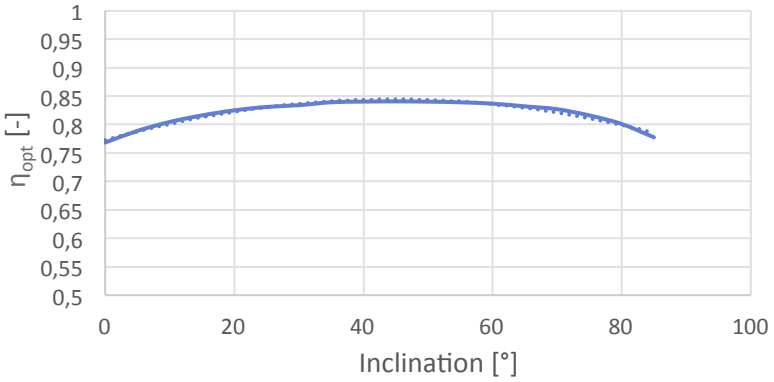

Figure 4.1 Optical efficiency varying receiver's tilt angle

The resulting efficiency curve gives a maximum for a tilt angle of 45°, corresponding to a receiver aiming on the y-direction of the field at 33 meters (the center the closest heliostat is at 8 meters, and the one of the farthest is at 49.2 meters in the y-direction, as shown in Figure 4.2).

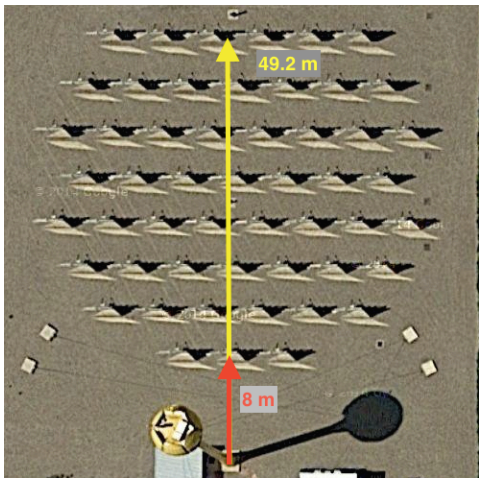

Figure 4.2 Aora field with y-axis notations, taken from [20]

These results are then confirmed by repeating the simulations for other characteristic days of the year such as summer solstice and winter solstice.
It is noteworthy that the optimal inclination angle is higher than the bisector angle (35.41°) of the field. This is an acceptable result since the field has a higher heliostats-density farther from the tower.
Thus, for the next simulations the inclination of the receiver is set at 45°.

4.2 Optical maps

Hereafter a script in SolTrace is written in order to change the sun's position in all the possible combinations of zenith-azimuth considering the assumptions reported in Table 1. The receiver is set as a flat surface with a very large area (diameter of 20 meters) in order to intercept all the rays coming from the heliostats and have an ideal analysis. Optical efficiency is then calculated in all the points.

Discretization is characterized by a 5°-step for the zenith angle, 10°-step for the azimuth angle and the number of rays launched for each simulation is 100 000.

Table 1 Assumptions to calculate optical efficiency

	Symbol	*Value*	*Unit of measurement*
Heliostats stage			
Reflectivity	ρ	0.94	-
Transmissivity	τ	0	-
Slope error	σ_{slope}	1.5	mrad
Specularity error	$\sigma_{specularity}$	0	mrad
Lateral side	L	4	meter
Surface	-	spherical	-
Absorber stage			
Absorbtivity	α	0.99	-
Slope error	σ_{slope}	0	mrad
Diameter	d	20	meter
Height	H	33	meter
Tilt	θ	45	°
Surface	-	flat	-

The final optical map of the absorber surface is presented in *Figure 4.3*. As expected optical efficiency is higher for low zenith angles when the sun is high in the sky and for azimuth around 180° when sun is south with respect to the field. However some unexpected undulations of optical efficiency at some azimuth values are observed.

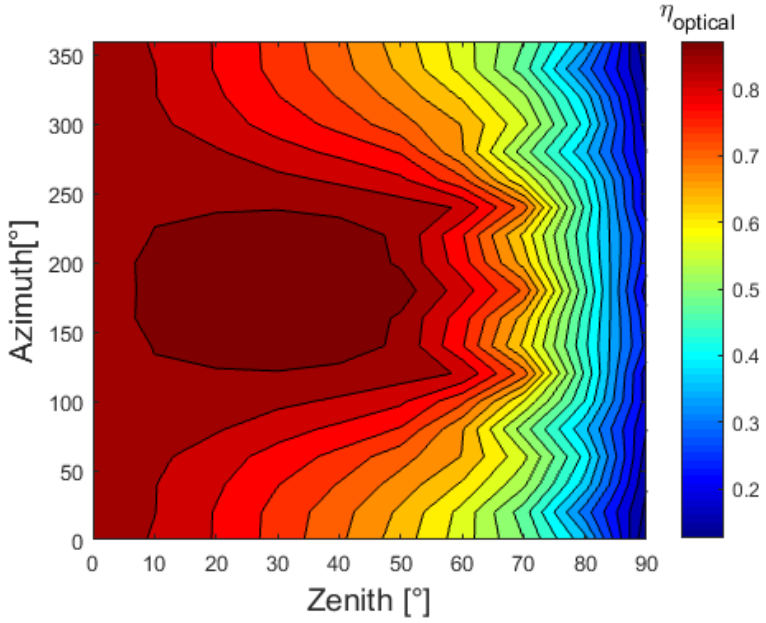

Figure 4.3 Optical Map of the receiver

To explain these undulations, the optical efficiency must be decomposed in its various components: cosine, blocking and shadowing effects. Their relative maps are plotted through a Matlab code (*Figure 4.4* and *Figure 4.5)*.

NB: the intercept factor isn't plotted since always equal to 1 (this analysis is a for a very large receiver).
As it can be seen, the undulations come from the blocking/shading effect. This makes sense since the density of the heliostats in the field is high, as exposed in the following equation:

$$density = \frac{A_{heliostats} * N_{heliostats}}{A_{field}} = 0.38 \quad (4.4)$$

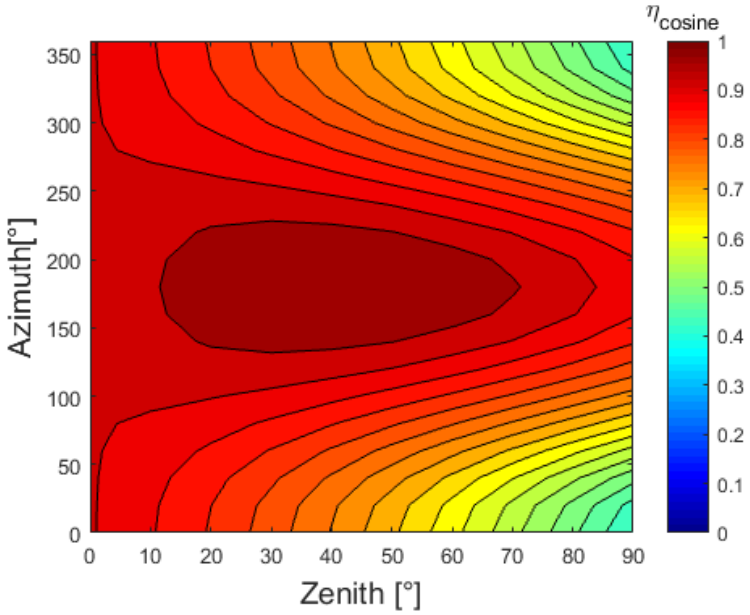

Figure 4.4 Cosine Map

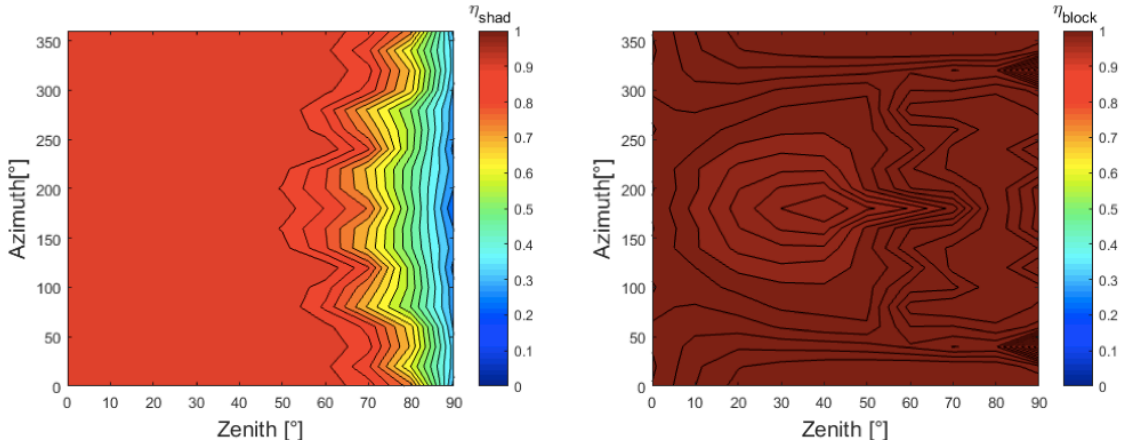

Figure 4.5 Blocking map (left) and Shadowing map (right)

Moreover a graph (*Figure 4.6*) is plotted to see at a fixed high value of zenith (meaning low elevation) the variations of the optical efficiency with the azimuth. This graph is in an azimuth interval of [0°-180°] since it would present a symmetric behavior in the next [180°-360°] interval.

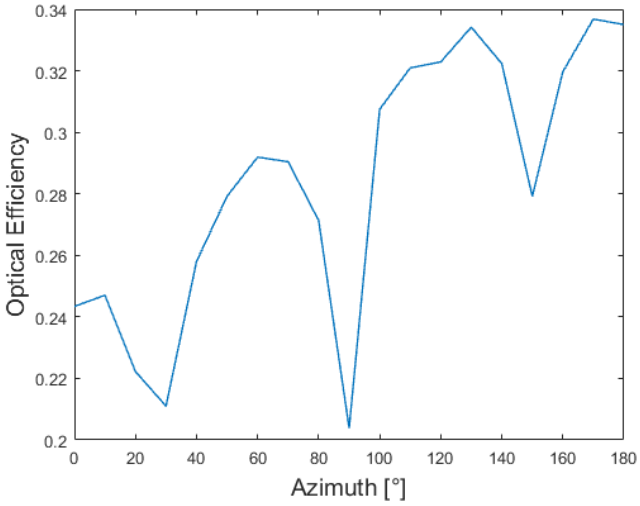

Figure 4.6 Optical efficiency at zenith equal to 10°

The minimum points of the graph (representing high shadowing effects as visible in *Figure 4.7*) feature:

- When the sun is in the diagonal path of the heliostat field; when Azimuth is 30° or 150°
- When the sun is completely East (or West); when Azimuth is 90°.

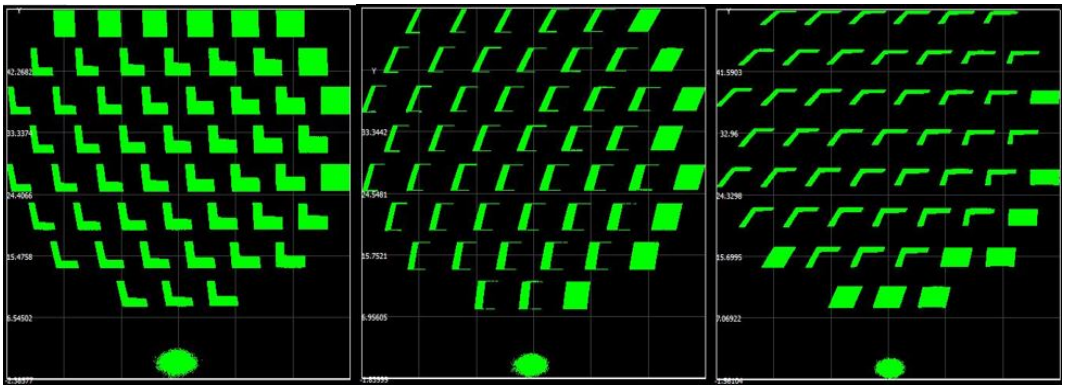

Figure 4.7 Rays reflected on Aora field heliostats, through SolTrace for a sun at zenith 80° and azimuth 28° (left), 90° (center) and 152° (right)

A screenshot of the field in an optimal condition, meaning a sun in the southern position and high in the sky is reported in Figure 4.8.

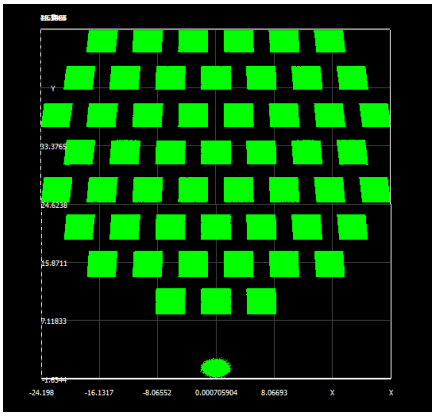

Figure 4.8 Rays reflected on Aora field heliostats, through SolTrace for a zenith 10° and azimuth 180°

Comparing the obtained map (*Figure 4.3*) with the one of the Planta Solar 10 (*Figure 4.9* taken from [29] it can be seen that the undulations aren't present. In facts, the heliostats density in the PS-10 is much lower (0.12) than for Aora (0.38). Moreover, in this latter figure, optical map of the Gemasolar receiver is visible as well and shows a totally different behavior but being characterized by "surrounded-field", other considerations must be done.

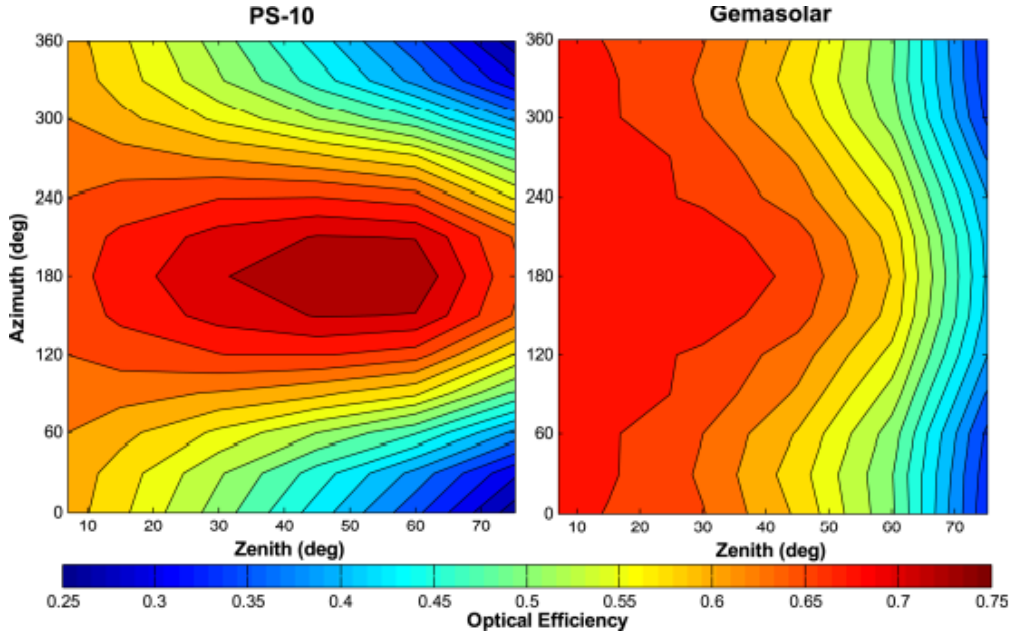

Figure 4.9 Optical Map of the receiver of the PS-10 plant (left) and of the Gemasolar plant (right)

4.3 Optimal diameter

The receiver is set as a flat surface with a very large area in order to intercept all the rays coming from the heliostats, but this is an ideal situation. Thus, the optimal diameter of the receiver must be found.
A script is SolTrace is attached to extract from a simulation the position of all the rays hitting the receiver (the reference is still at the autumn equinox, at Solar Noon in Sevilla).

Determination of the standard deviation of the surface slope error, σ, is critical for good modeling accuracy. To show the impact of the heliostats slope error, four cases are implemented, changing the slope error at values: 0, 1, 2, and 3. In these four cases, specularity error is set as 0, so that the total error is given only by the slope error (and is twice its value as calculated with equation (3.1)).
For each case, the ray positions are given as an input to a code in Matlab, to calculate the optimal diameter of the receiver in order to intercept 98% of the total rays arriving on the large squared surface.
Results (in *Figure 4.10*) show that for the ideal case (0 error) the required absorber radius is 0.6 meters; for the case with slope error equal to 1 the radius is 0.7 meters; for the case with slope error equal to 2 the radius is 0.75 meters and for the worst case the radius is 0.9 meters. These results show the influence of the slope parameter in the design of the receiver.
On the contrary, slope error has no impact on the distribution of the incident angles of the rays on the receiver. This is visible from the colors of the points, representing the arrival angle of the rays on the receiver. Hence a higher slope error doesn't change the interval of angle-values, nor their distribution (which is random in all the cases). This is an important consideration for the next analysis, where the receiver will be modeled as a Compound Parabolic Concentrator.

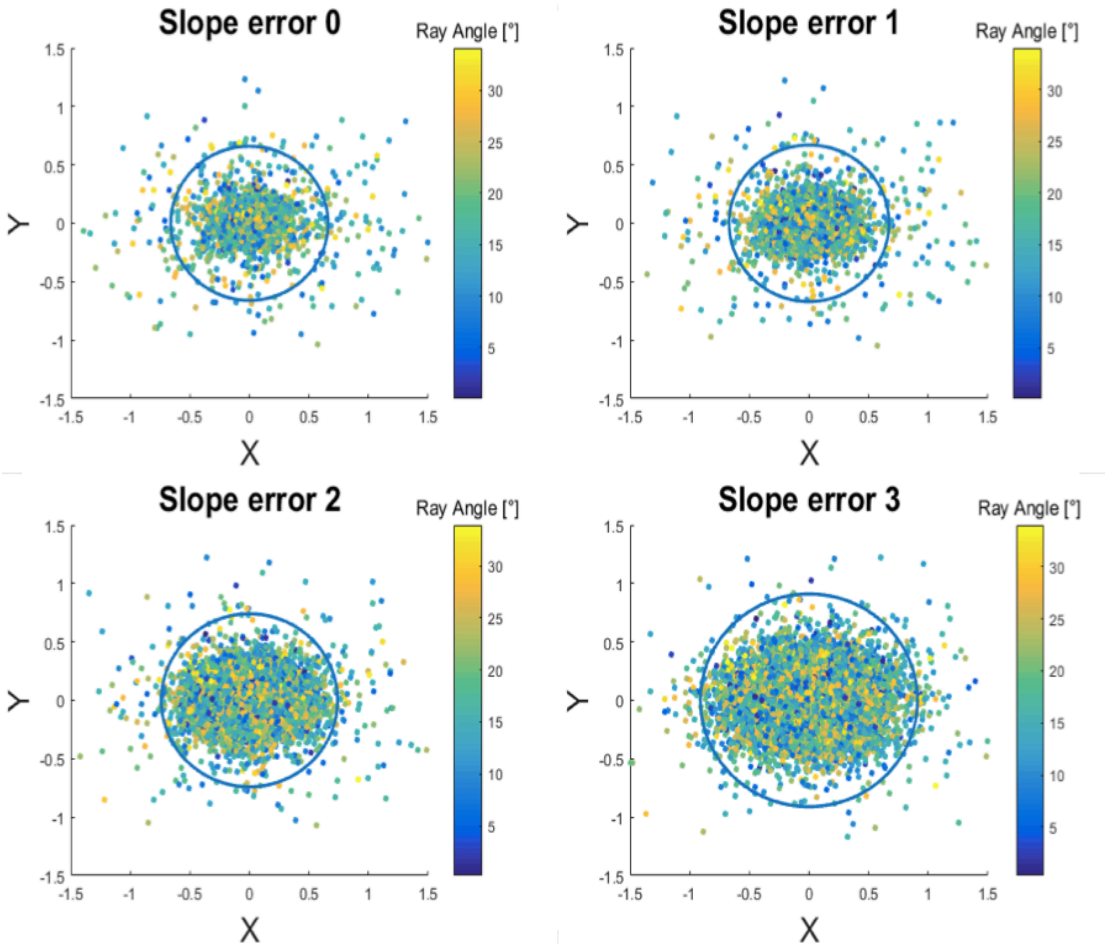

Figure 4.10 Rays on the receiver, varying slope error of heliostats (ray incident angle are shown with the color bar)

From available publications of optical modeling of solar tower system [30], a reasonable slope error seems to be **1.5 mrad** (corresponding to a 3 mrad total optical error). Thus, 1.5 mrad is the value used for all the next analysis.

To give some values with this slope error, and splitting the optical efficiency in its various components (*Figure 4.11*): net optical efficiency at Solar Noon is best on autumn equinox (reaching 0.91 value) whereas worst on winter solstice (0.82). About the cosine effect, on summer solstice zenith angles are usually low, and thus the cosine loss becomes larger. Blocking effect has a low weight but it is not as negligible as it should be (blocking efficiency is equal to 1), and this is due to a bad design of the field layout (heliostats are too close from each other). Shadowing effects are mostly significant during winter timer, when the sun is lower in the sky (the tower's shade adds to the heliostats shades). Intercept factor is not displayed as it is always equal to 1 (this ideal analysis is done with a receiver characterized by a diameter of 20 meters).

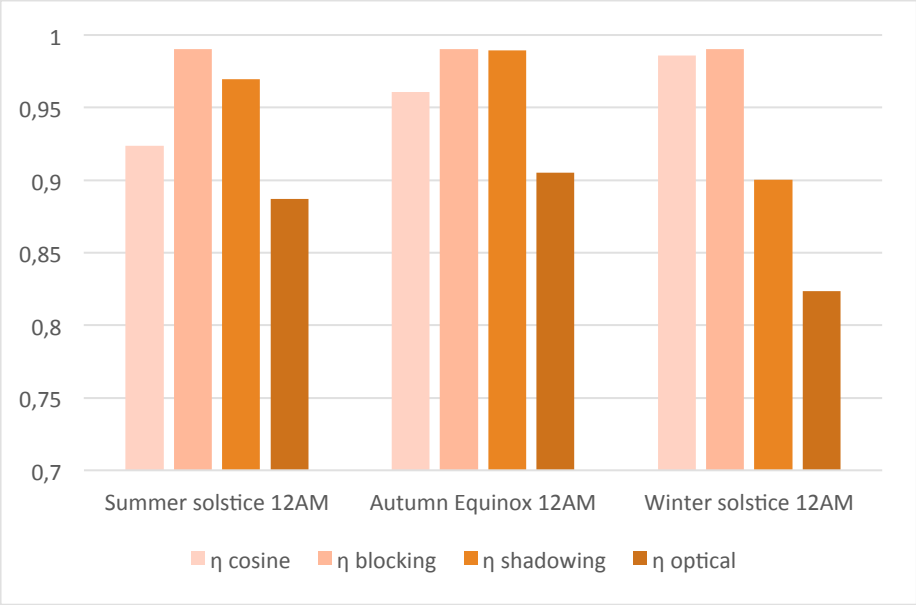

Figure 4.11 Optical efficiency variations

Finally, as it will be useful for the next chapter regarding the design of the Compound Parabolic Concentrator, it is important to reason on the incidence angles of the rays on the receiver. Indeed, over 10 000 rays launched for three different hours of the same day, the number of rays arriving with each incidence angle have been reported in Figure 4.12. The observed maximum angle is 34° no matter the hour of the day when the receiver is inclined of 45°, which is consistent with the field layout (the angle between the normal of the receiver and the normal of the closer heliostat from the tower is 35°). On the contrary, what changes with time, is the distribution of the angles.

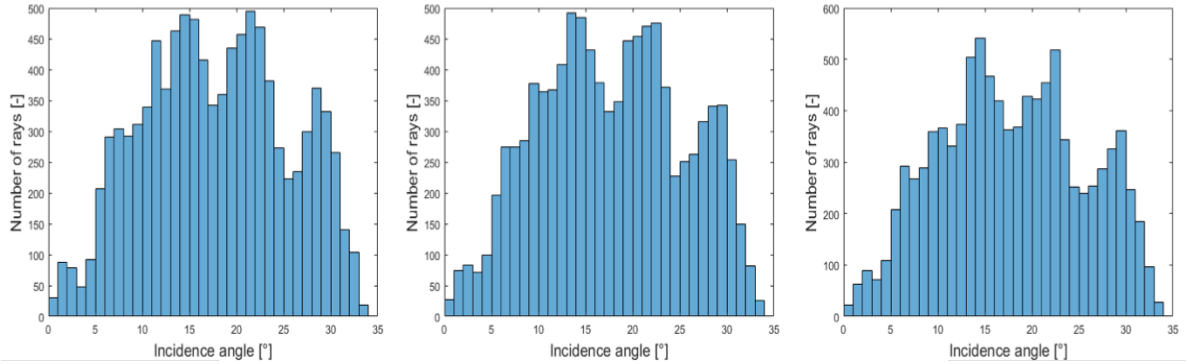

Figure 4.12 Incident angles of rays on a receiver tilted of 45°; on equinox day at 8 AM (left), 10 AM (middle) and 12 AM (right)

Furthermore, if the receiver would be tilted as the bisector of the field, the interval of arrival angles would be different. Indeed, the maximum ideal angle in this latter case is lower (*Figure 4.13*), and in this case the rays with the highest incidence angle come both from the further mirror of the field and from the closest one.

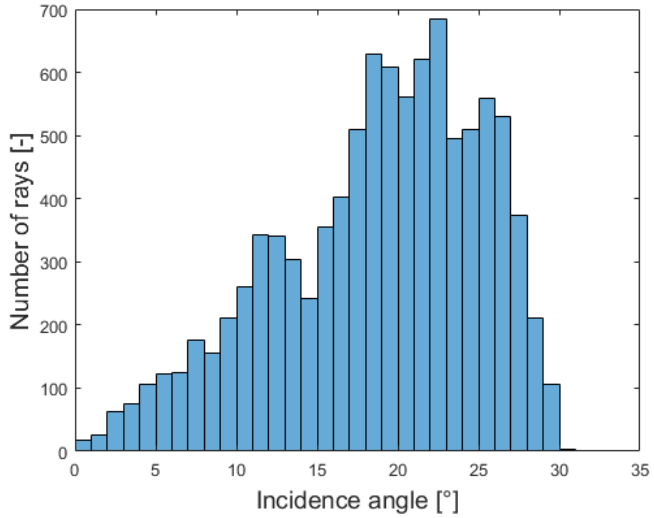

Figure 4.13 Incident angles of rays on a receiver inclined of 35.41° at equinox at 12 AM

In conclusion, the distribution of the various angles is a function of the receiver's inclination, of the field layout (number of heliostat in each row, number or row, distance between rows…) and of course of the sun's position.

Still in relation with the CPC, a consideration must be done about the optimal diameter of the receiver. First intuition was to look at the intercept factor; thus for each hour, following the values of the sun's zenith and azimuth, the intercept factor is calculated and weighted on its relative DNI. To have an annual intercept factor equal to 98% the resulting required diameter is **1.85 meters (***Figure 4.14***)**; which is higher than in all the previous cases (in the slope error analysis) where only equinox at noon was considered.

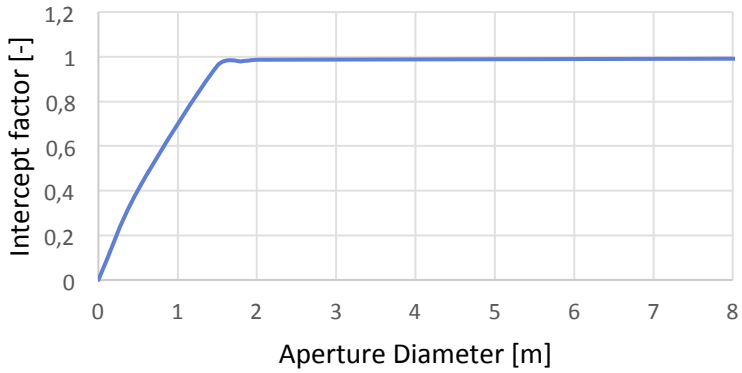

Figure 4.14 Intercept factor versus receiver's aperture diameter for a 1,5 slope error

In the next section, introducing the CPC receiver, it will be seen that the required aperture diameter is designed to have the highest efficiency and not the desired/highest intercept factor.

5. Secondary receiver

A secondary receiver allows to have a smaller absorber area for the same aperture area, increasing the concentration ratio of the solar block and hence, increasing the thermal efficiency.
The Compound Parabolic Concentrator (CPC) is a special type of solar collector fabricated in the shape of two meeting parabolas. It belongs to the non-imaging family, but is consider among the collector having the highest possible concentrating ratio. The CPC is provided in order to improve the thermal efficiency of the tower-top central receiver.

5.1 Geometric construction

The CPC can be represented in the space by the rotation of a parabola arc along the symmetric axis of the concentrator. The origin of the Cartesian axes is set at the center of the exit aperture and the z-axis was set along the CPC axis (*Figure 5.1*). Considering the angle ϕ between the focus of the parabola arc and a point on the arc, and θ the acceptance angle of the parabola, the following equations are used, taken from [31]:

$$\begin{cases} y = \dfrac{2a'\left(1+sin\frac{\theta_i}{2}\right)\sin\left(\phi-\frac{\theta_i}{2}\right)}{1-\cos\ \phi} - a' \\ z = \dfrac{2a'\left(1+sin\frac{\theta_i}{2}\right)\cos\left(\phi-\frac{\theta_i}{2}\right)}{1-cos\phi} \end{cases} \quad (5.1)$$

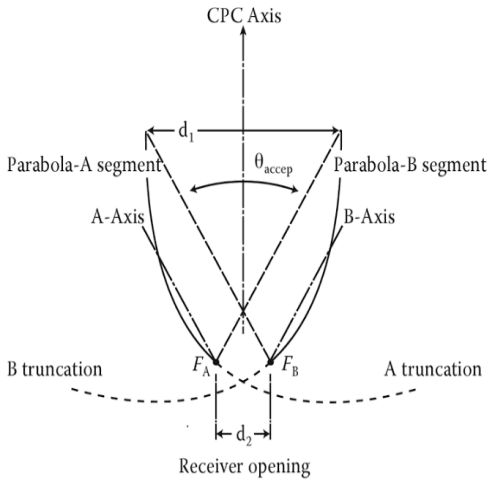

Figure 5.1 Parabolas of a CPC, taken from [3]

CPC modeling in SolTrace

Since SolTrace doesn't allow to insert the analytical equation of the CPC surface to build the element, other surfaces must be used. As a first approach, the lateral side of the CPC is created using the "Cubic Spline Surface", that requires an input file (*.csi*) with a sequence of points calculated [y z]. Files are created using 70 defining points in between the two top surfaces.
A reasoning can be done about the optimal partition of the defining points. In this first approach, points were created in order to have a constant increment in the radius of the horizontal surface of the cone. But as suggested by [32] points could be chosen to satisfy the condition that difference between consecutive slopes remains constant.
Various files are created to define CPC with same aperture are but different semi-acceptance angles: from 30° to 90° (which is the most ideal case since all the incident rays are accepted). The lower limit is set at 30° because of the field layout (*Figure 3.6*); indeed considering lower angles would exclude too many rays (all the ones arriving with an angle higher of the acceptance angle).
As it can be seen in Figure 5.2, for a fixed aperture area of the CPC, the higher the acceptance angle, the higher the absorber area and the shorter is the CPC.

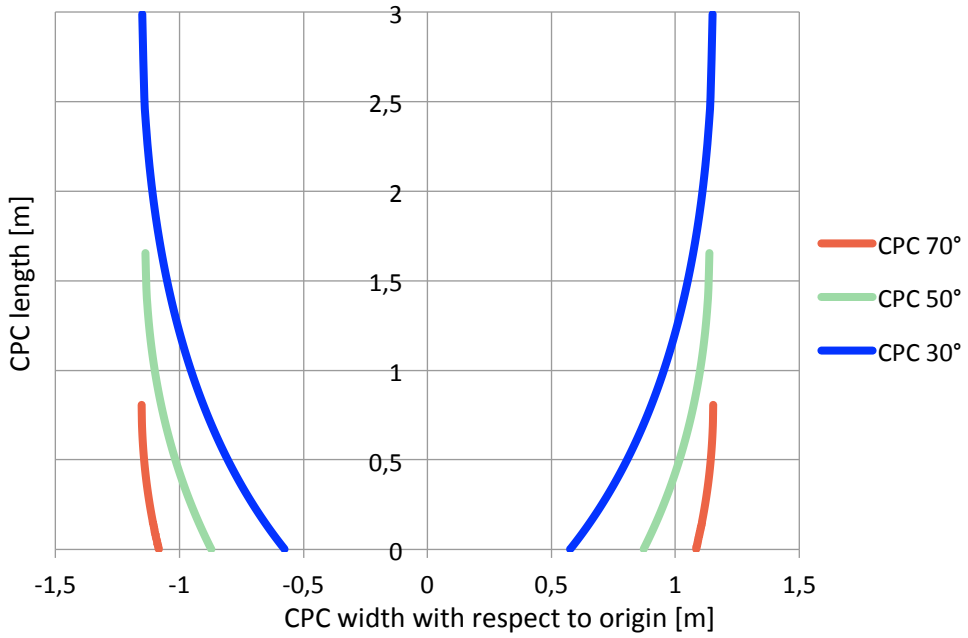

Figure 5.2 CPC layouts, for three different acceptance angle and a fixed aperture area

5.2 Transmittance curves

Transmittance is defined as the fraction of the radiation reaching the absorber area to the radiation entering the aperture area of the CPC:

$$Tr = \frac{E_{abs}}{E_{aper}} \tag{5.2}$$

Directly through a script, the sun is displaced following a day path, and the fraction between the rays incident on the smaller absorber surface and the rays incident on the larger aperture area (created as a virtual surface on SolTrace) is calculated. Thus, transmittance curves are traced using Excel. Computational time is in the order of 3 minutes, since the single trace requires about 2 seconds and 90 positions of zenith are simulated. Results shown in *Figure 5.3* present a wrong trend, meaning that something is not working well with the simulations.

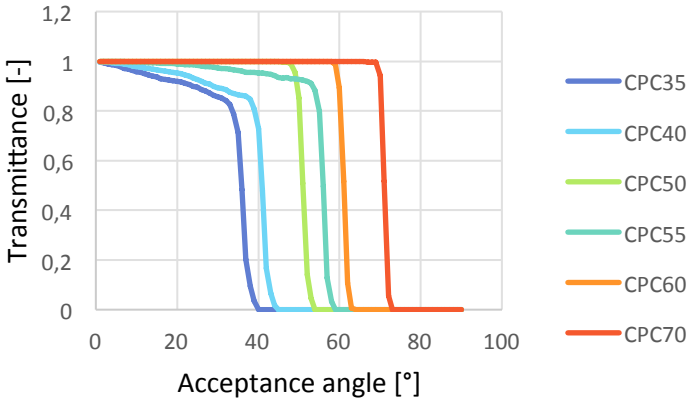

Figure 5.3 Transmittance curves using Cubic Spline Surfaces

In *Figure 5.4* for a CPC with 55° semi-acceptance angle, the number of defining points of the parabola is increased; as it can be seen, transmittance trend approaches the ideal one with a higher number of points.

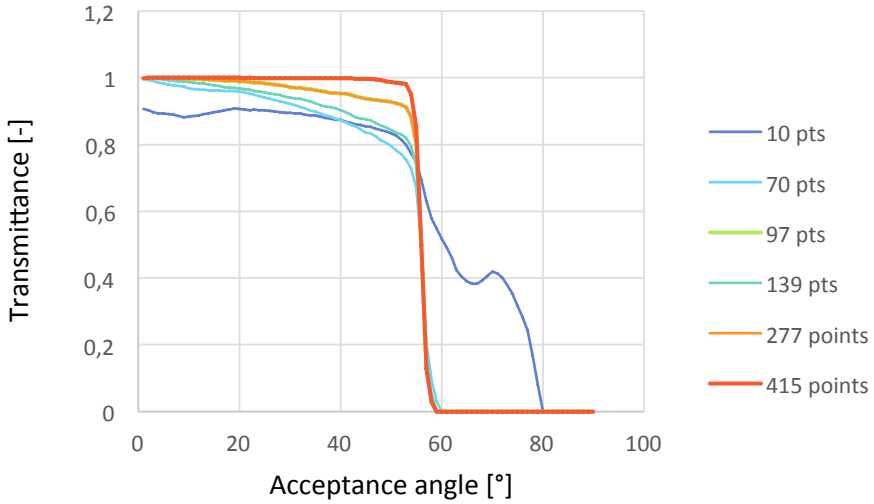

Figure 5.4 Transmittance curve of the CPC with 55° acceptance angle

However this not the case for all the CPC geometries. Indeed, for example a CPC with acceptance angle 40°, never approaches ideal transmittance curve; not even with a thousand defining points.
Therefore thanks to further investigations, it appeared (*Figure 5.5*) that some rays crossed the CPC without being disturbed by the reflective surface. Thus, the previous error came from a SolTrace-software internal issue when using the Cubic Spline Surface for 3D CPC; confirmed by SolTrace's suppot team.

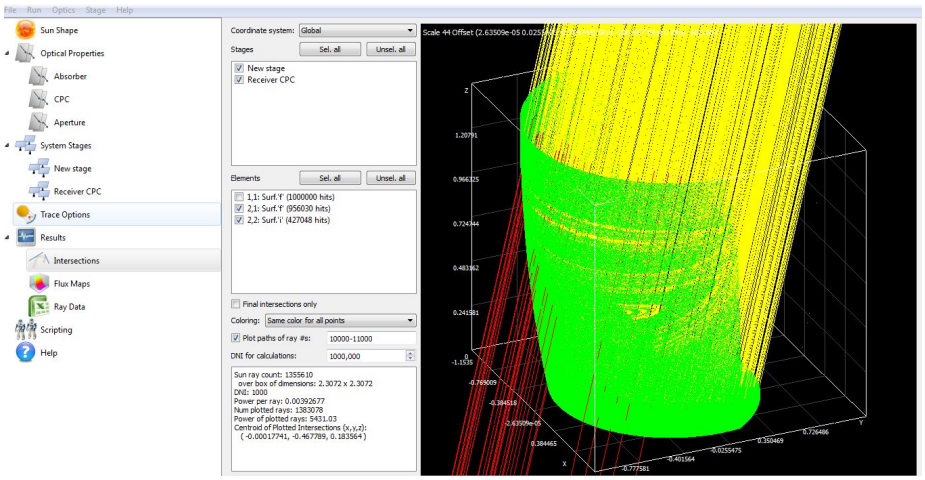

Figure 5.5 Rays passing through the receiver, from SolTrace Platform

As a solution, the Conic Spline Surface is used instead of the Cubic Spline Surface. In this way, the CPC is built by defining a number of truncated cones. In *Figure 5.6* are illustrated some CPC profiles of same acceptance angle, defined with a different number of cones (through SolTrace interface).

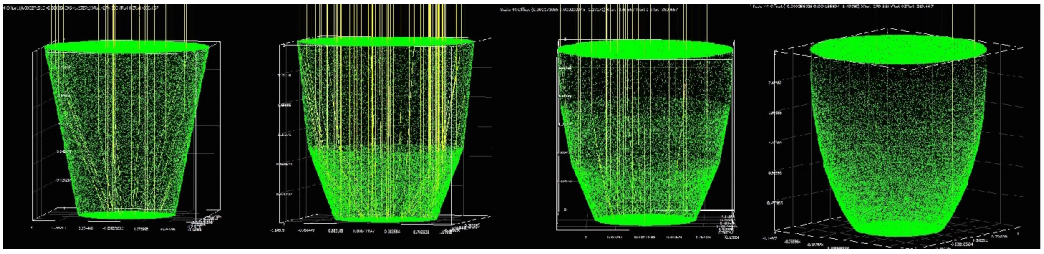
Figure 5.6 CPC profiles varying the number of defining cones

In this second approach, first trial is to set a single reflective cone (as it was a V-through concentrator) between the aperture surface and the absorber surface. As expected, the transmission curve is not the CPC ideal one (*Figure 5.7*), but at least the same behavior is observed for all the geometries.

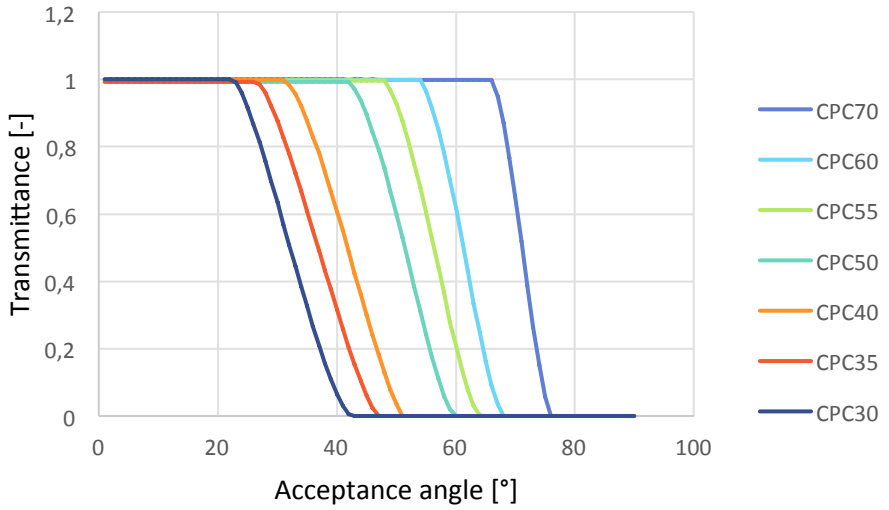

Figure 5.7 Transmission curves for V-through concentrators

For an infinite number of cones, the geometry of the CPC is surely well defined, but this is an ideal situation; a finite number of cones must be set to do the analysis. This optimum number is investigated using the CPC with acceptance angle 35° (which is the one supposed to be optimal, supposing ideal behavior). The number of cones is increased from 1 to 100, and the transmission curves are compared to the one obtained with the Cubic Spline definition (which in this case was working, with no leaking rays). Results (*Figure 5.8*) show that 15 defining cones already give good approximations of the CPC geometry. Nevertheless, the following part considers 96 defining cones for each CPC (in order to have perfect matching results).

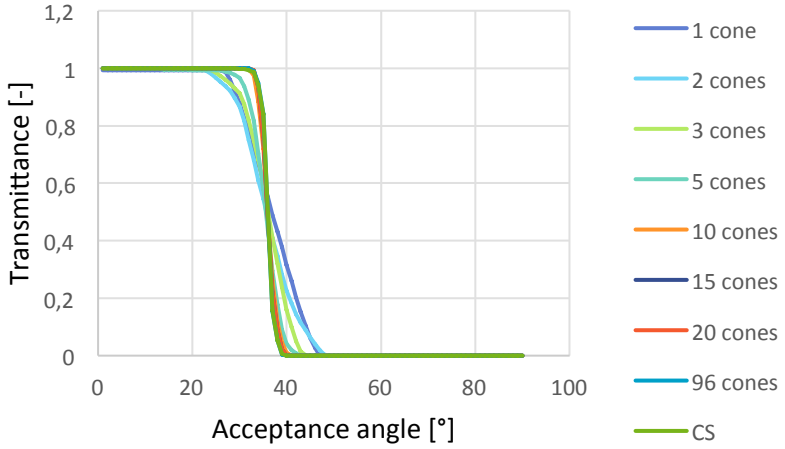

Figure 5.8 Transmission curves of CPC35 for different numbers of defining cones

At this point, all the CPC are constructed in order to give reliable simulations in SolTrace. Ideal transmission curves are shown in Figure 5.9, as well as real ones considering total optical errors equal to 3 mrad and a reflectivity of 0.94. For each

position of the sun 100 000 rays are launched and considering the 96 elements defining the CPC, the resulting computational time of each trace increases to 11 seconds; meaning that to draw a transmission curve more than 16 minutes are required (since zenith of the sun is modified of a 1 degree-step from 0° to 90°).
As it can be noticed in real conditions the intercept of the absorber in the CPC is never equal to 1. Moreover the lower the acceptance angle and the larger is this error. This can be explained by the fact that the lower the acceptance angle, the smaller the absorber area and the longer the side-wall of the CPC (for the same aperture area), so the more the rays will hit the side-walls of the CPC before the absorber area (and so, the more the rays affected by the errors).

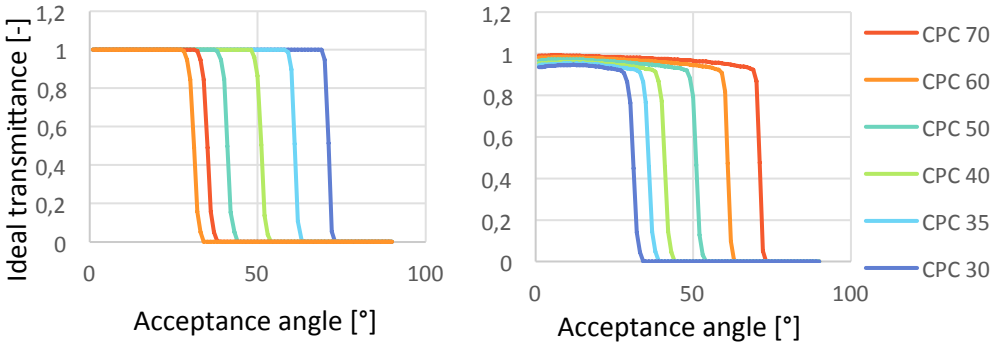

Figure 5.9 Ideal (left) and real (right) transmission curves

A further investigation is done to see the weight of the non-ideal behavior, between the optical errors and the reflectivity reduction. The results showed that the reflectivity accounted for 99% of this reduction.

Until now transmission curves are obtained by placing the CPC on the ground. To evaluate the optical efficiency of these CPC in the actual field, they need to be placed on top of the tower, with the optimal inclination found previously (45°).
In this configuration, computational time reduces to 6 seconds per trace. Optical maps are obtained to have all the efficiencies (and not only the one in the sun's path occurring in Sevilla) in order to be able to extend the simulations to any location if required in the future.
Thus, optical efficiencies are obtained through a script (zenith is discretized by a 5° step while azimuth is discretized by a 10° step) and the final map requires about half an hour to run (19x19 points are calculated).

5.3 Optimal tilt check

Until this point the inclination of the receiver is kept at 45°, which is the optimal inclination found for a flat receiver. Nevertheless having now a different geometry of the receiver, strictly related to ray incidence angles, this inclination could lose it significance. It is thus necessary to re-investigate the variation of the optical efficiency (on the equinox days) varying the inclination of the CPC receiver.

As an anticipation, the optimal geometry of the CPC to maximize annual efficiency (including both optical and thermal contributions) is the one characterized by an aperture diameter of 1.3 meter and an acceptance angle of 35°. Thus, this analysis is done for three similar/meaningful CPCs: having the same aperture area, and three different acceptance angle (32.5°, 35° and 37.5°).
Results as are visible in *Figure 5.10*. The optimal tilt angle is always closely around 45° (which was the value found previously for the flat simple receiver), and this value is thus considered the correct one for an optimized field.

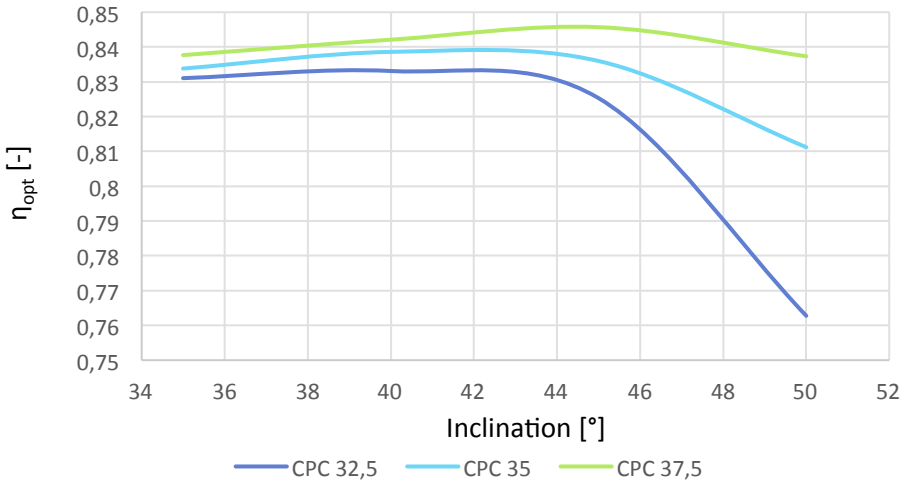

Figure 5.10 Optical efficiency varying CPCs inclinations (for three different acceptance angle geometries: 32.5°, 35° and 37.5°)

5.4 CPCs yearly efficiencies on field

The investigated CPCs have the following acceptance angle: 32.5°, 35°, 37.5° and 40°. In fact, given the geometry of the heliostats and the inclination of the receiver, lower acceptance angle would cut-off too many reflected rays (indeed the theoretical optimal acceptance angle is 35°, given by the rays hitting the receiver as shown in Figure 4.12).

Once optical yields are registered from SolTrace, the optical maps of the various CPCs are created. Thanks to these maps, optical yield for each azimuth-zenith combination is available, interpolating values in the chosen optical map.

Using this last script, an analysis can be done on the annual optical efficiency, giving as input the sun's zenith-azimuth registered last year in Sevilla, hour by hour (values are downloaded through System Advisor Model program [25]). The yearly-average-optical-efficiency is computed according to [33] (weighted on the relative DNI):

$$\eta_{opt-annual} = \frac{\sum_1^{8760} \eta_{opt}(h) * DNI(h)}{\sum_1^{8760} DNI\,(h)} \tag{5.3}$$

Optical efficiency increases for higher aperture areas (more power intercepted), and for a given aperture area, the value is higher for a higher acceptance angle (corresponding to a shorter CPC and thus, a higher absorber area).
Results are plotted on *Figure 5.11* in function of the minimum diameter of the CPC (representing the absorber) and in function of the maximum diameter of the CPC (representing the aperture). As expected, for a given aperture diameter, a CPC with lower acceptance angle gives a lower optical efficiency (corresponding to a smaller aperture area and so a lower intercept factor). From an optical point of view, the best conditions are given by the CPC with the highest acceptance angle, and the highest aperture area possible (tending to the maximum value given by a flat simple absorber with infinite area).

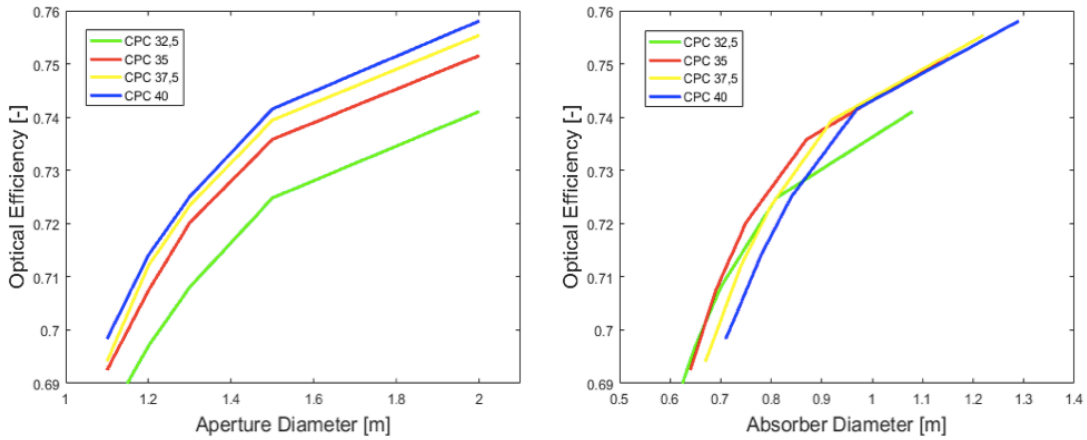

Figure 5.11 Optical efficiency of various CPC

Nevertheless the heat entering the cycle is also affected by the thermal efficiency of the absorber and the CPC, which actually increases with the concentration ratio. As a first approximation thermal efficiency was calculated with equation (5.4), with a sun irradiation G equal to 900 W/m^2 (this value is very important because it highly affects the efficiency and thus, the choice of the CPC).

$$\eta_{thermal} = 1 - \sigma \frac{\varepsilon * (T_{receiver}{}^4 - T_{ambient}{}^4)}{G * CR * \eta_{optical}} \qquad (5.4)$$

For a given aperture diameter lower acceptance angle CPCs give higher thermal efficiencies because they concentrate more the radiation; while for a given absorber diameter, the thermal efficiency is constant no matter the acceptance angle of the CPC (as shown in *Figure 5.12*).

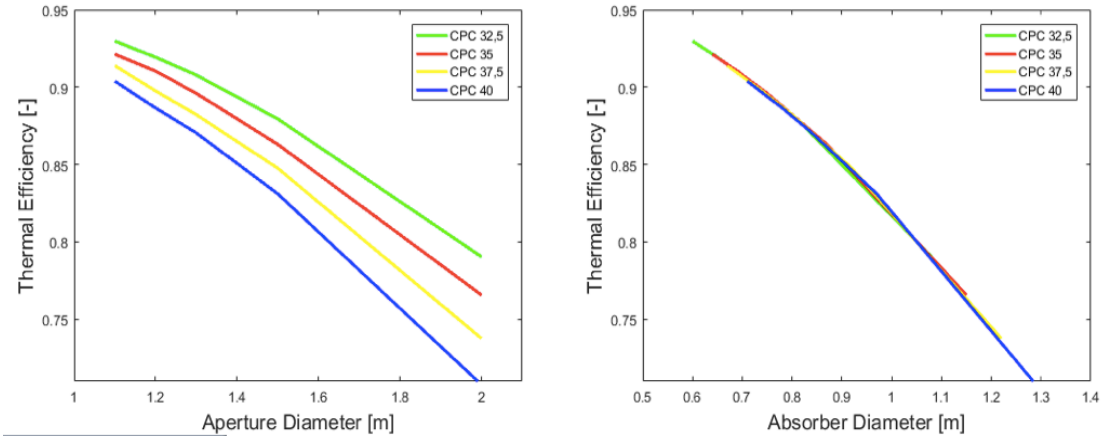

Figure 5.12 Thermal efficiency of various CPC

To decide which CPC geometry to choose it is necessary to consider the maximum value of the total efficiency, given by:

$$\eta_{total} = \eta_{optical} * \eta_{thermal} \tag{5.5}$$

The optimum annual total efficiency in Sevilla (*Figure 5.13*) is found for a CPC with 35° acceptance angle, an absorber area with a 0.75 meters diameter and an aperture area with a 1.3 meters diameter, corresponding to a final concentration ratio of 1883. Moreover the intercept factor is approximately 90%.

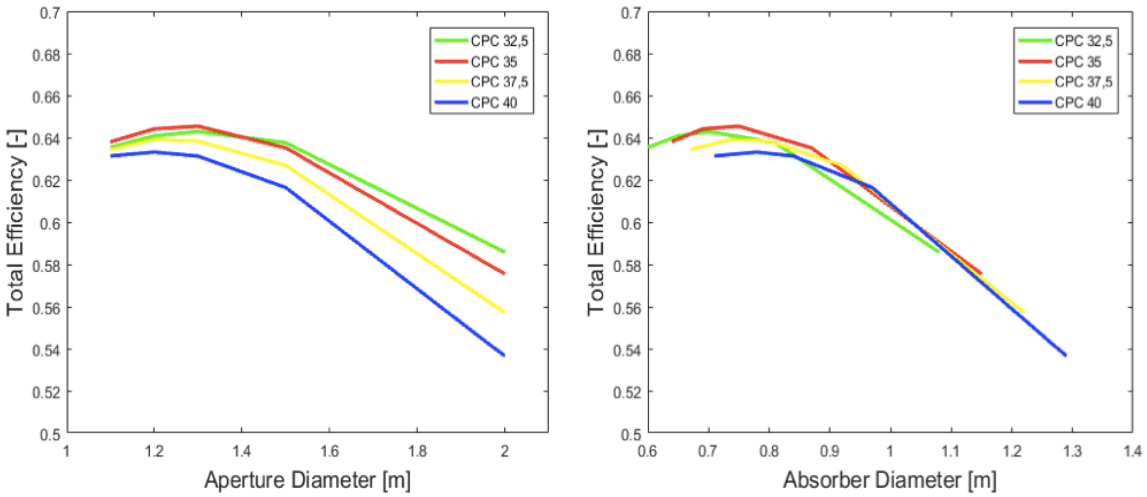

Figure 5.13 Total efficiency of various CPC

As the intercept factor is lower than the one initially suspected, an additional analysis is done to control that all the heliostats are useful. Thanks to SolTrace, rays positions were exported and a script in Matlab implemented to calculate the provenance of the useful rays. Results showed that the reduction of rays intercepts was uniformly distributed among the heliostats; confirming the choice of this CPC.
In the *Table* 2 geometrical values and obtained efficiencies of the different CPCs are reported.

Table 2 Geometrical characteristics of investigated CPC

Acceptance angle [°]	Aperture Diameter [m]	Absorber Diameter [m]	CPC Length [m]	η Optical [-]	η Thermal [-]	η Total [-]
37,5	2	1,22	2,08	0,7554	0,7377	0,5572
37,5	1,5	0,92	1,56	0,7394	0,8476	0,6268
37,5	1,3	0,8	1,35	0,7234	0,8822	0,6382
37,5	1,2	0,74	1,24	0,7121	0,8976	0,6392
37,5	1,1	0,67	1,12	0,6941	0,9139	0,6343
35	2	1,15	2,21	0,7516	0,7658	0,5755
35	1,5	0,87	1,67	0,7358	0,8631	0,6351
35	1,3	0,75	1,44	0,7202	0,896	0,6453
35	1,2	0,69	1,32	0,7074	0,9104	0,6441
35	1,1	0,64	1,25	0,6925	0,9213	0,638
32,5	2	1,08	2,4017	0,7411	0,7905	0,5858
32,5	1,5	0,81	1,7856	0,7248	0,8795	0,6375
32,5	1,3	0,7	1,563	0,7081	0,9079	0,6428
32,5	1,2	0,65	1,4283	0,697	0,9193	0,6408
32,5	1,1	0,6	1,3236	0,6832	0,9299	0,6353

The yearly optical, thermal and total efficiencies of the chosen CPC are relatively equal to: 0.7202, 0.896 and 0.6453. Its optical map is showed below in *Figure 5.14*.

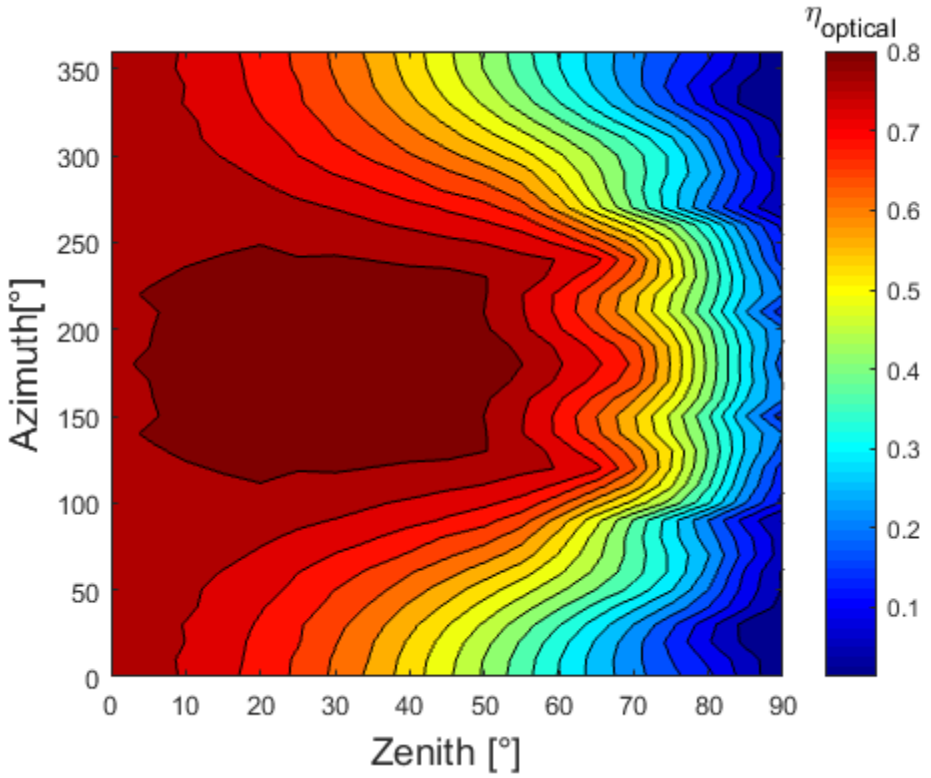

Figure 5.14 Optical map of the CPC with 35° acceptance angle and absorber diameter 0.75 m

NB: it is also important to control the mean flux hitting the absorber (to check its consistency with the chosen receiver attached to the CPC). In fact, as presented in *Figure 5.15* at 12 AM of autumn equinox, the peak flux arriving on the absorber with the 35° CPC is 4675 kW/m^2, while the average flux is of 1240 kW/ m^2 (which is tolerated for volumetric receivers but not for tubular ones, as it is discussed in the *Chapter 6*).

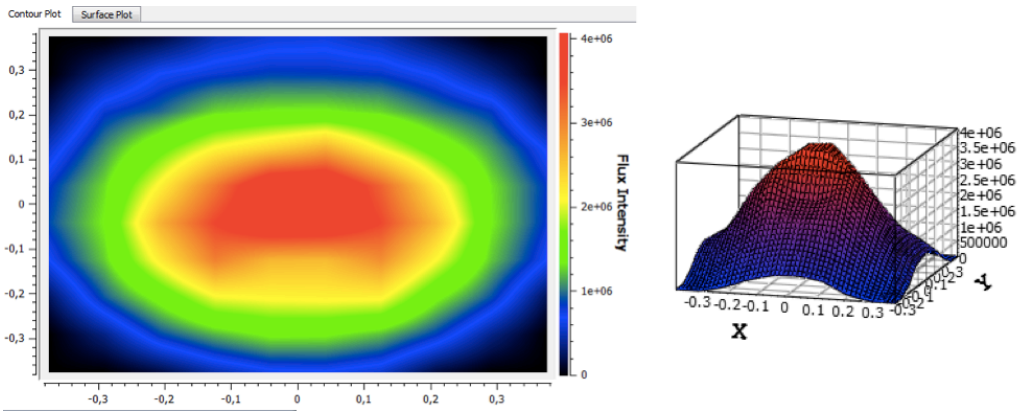

Figure 5.15 Receiver's flux in 2D (left) and 3D (right), as seen on the SolTrace Platform

Additionally, an analysis can be done using other locations than the actual one (Sevilla); two other locations are selected:
- Daggett, California, USA: characterized by a high annual irradiation (about 2.8 GWh/m^2), it is the venue of the most important CSP systems (SEGS 1, SEGS 2, Solar One, Solar 2).

- Messina, Sicily, Italy: characterized by a lower irradiation (1,1 GWh/m^2) than the one in Sevilla (1,8 GWh/m^2), but one of the highest in Italy.

Zenith, Azimuth, and DNI values of last year were again downloaded through the System Advisor Model program for Daggett and Messina locations (Figure 5.16 and *Figure 5.17* show the values of ambient temperature and DNI registered in the three locations in 2015).

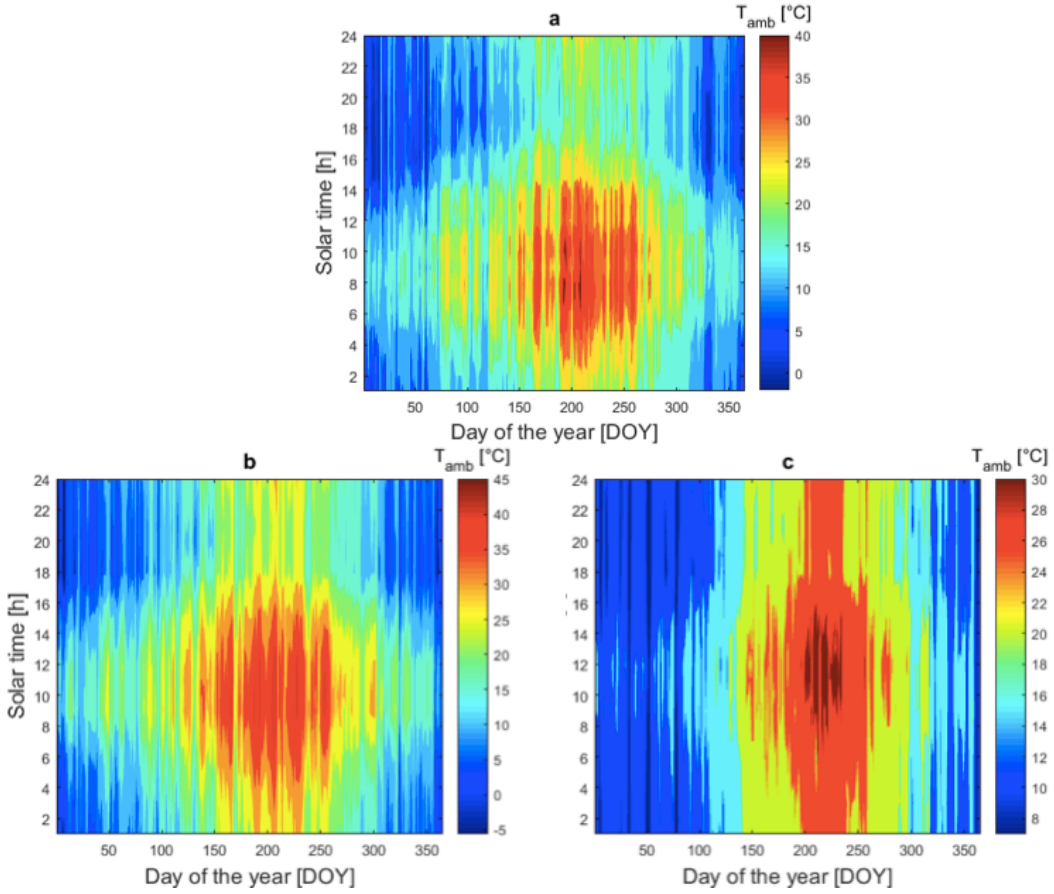

Figure 5.16 Hourly variation of ambient temperature [°C] through the month of June in Sevilla (a), Daggett (b) and Messina (c)

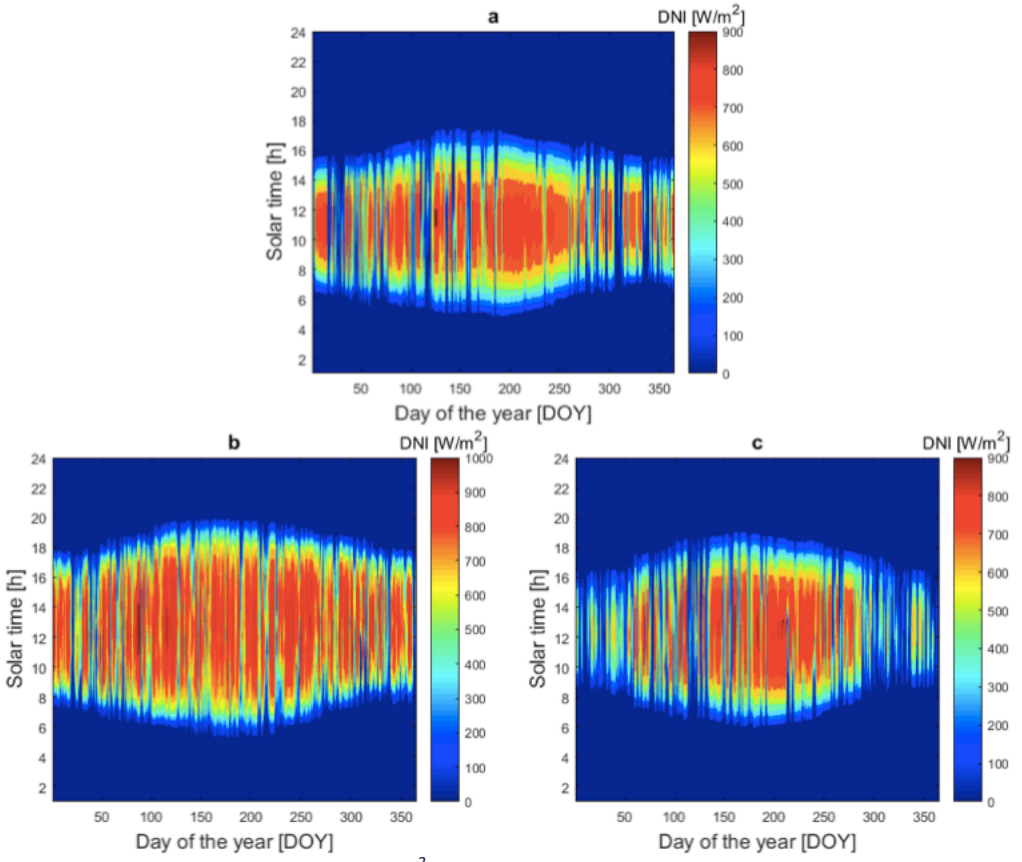

Figure 5.17 Hourly variation of DNI [W/m^2] through the month of June in in Sevilla (a), Daggett (b) and Messina (c)

What was observed is that annual optical efficiencies are lower in Daggett (0.6748), and higher in Messina (0.7267) compared to the Sevilla case (0.7202). In fact, in Daggett DNI at early hours in the morning and late hours in the evening is much larger than in the other two cases, giving more weight to optical efficiency at those hours, and since their values are lower (as shown in the optical maps) the total annual optical efficiency is lower.

Another ascertainment is that average ambient temperature in Daggett is much higher than in the other two locations, leading to higher thermal losses at the receiver (in Sevilla average thermal efficiency is 0.8960, in Messina 0.8970 and in Daggett 0.8890).

Nevertheless since the solar input is much larger in Daggett, also the heat entering in the cycle is larger, giving a higher final energy output.

6. The thermal receiver

The absorber has the task to absorb the impinging concentrated solar radiation and transfer the absorbed heat to the heat transfer fluid (which in this case is pressurized air). First developments and researches focused on tubular receivers but due to temperature limitations, volumetric receivers are today's challenged. Nevertheless, tubular receivers are suggested to be more robust, cheaper and less complex technologies so investigations are still on.

6.1 Tubular receivers

In tubular receiver designs concentrated solar radiation is absorbed by a bundle of tubes able of withstanding high temperatures. The energy is then transferred to the HTF flowing within the tube. The tube temperature is always greater than the fluid temperature, which limits the maximum operating temperature. On the other hand tubular designs have the advantage that the HTF fluid can easily be pressurized and the only pressure limit is the yield strength of the tubes.
Usually, tubular receiver designs have heat loss problems to the ambient due to reflection, thermal radiation and convection losses. In order to minimize reflection losses the tubes are commonly covered with solar selective coating to increase the solar absorbance. However, the solar flux remains limited to about 200 kW/m^2 [34].

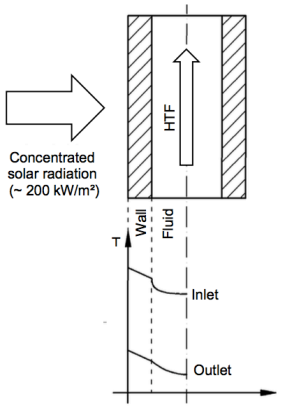

Figure 6.1 Temperature profile on a tubular receiver, taken from [34]

Pressure drop across the tubes presents a linear behavior with the temperature of the HTF (a higher temperature induce a lower pressure drop), and increases along the tube. Anyways, pressure drop never exceeds 10% of the inlet pressure of the fluid .

Considering receivers reaching temperatures in our field of interest (above 800°C), ambient heat losses are kept low by placing the tubular absorber in a cavity.

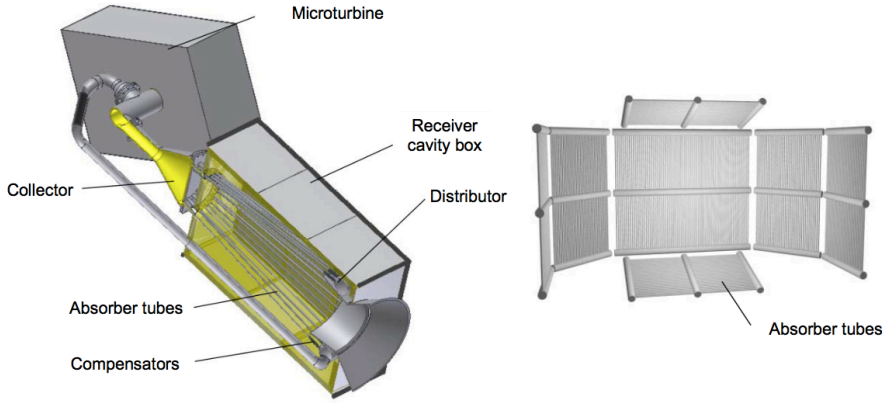

Figure 6.2 Cavity tubular receivers: on the left SOLHYCO, on the right SOLUGAS, taken from [34]

Figure 6.2 shows recent tubular receiver design developments. The SOLar HYbrid power and COgeneration plants (SOLHYCO) tubular cavity design is based on a 100 kW micro turbine and the receiver works at a fluid outlet temperature of around 800°C with the possibility to operate on varying contributions of solar power input and fuel. The model is composed by 40 tubes of 20 meters length [35].
The Solar Up-scale Gas Turbine System (SOLUGAS) tubular cavity design is is the next generation of the SOLHYCO, based on a solar pre-heated Brayton topping cycle and a subsequent Rankine bottoming cycle. The receiver consists of several tubular receiver panels (composed by 170 tubes of 5 meters length) and is used to pre-heat the pressurized HTF which is air up to 650°C before it enters the combustion chamber of a commercial 4.6MWe gas turbine (see [36] and [37]).

A promising alternative, that has been simulated but not tested yet is the Spiky Central Receiver Air Pre-heater (SCRAP), which is an external tubular receiver.

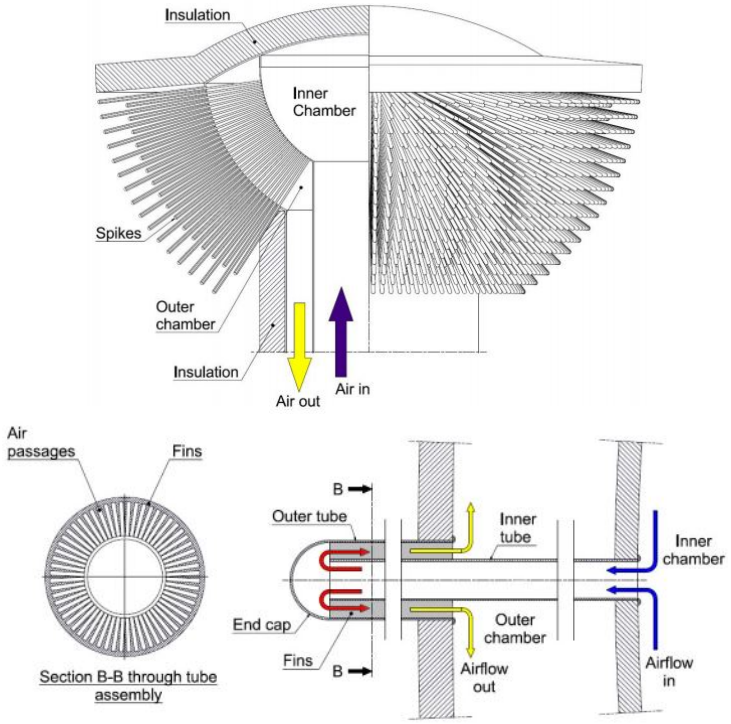

Figure 6.3 SCRAP external tubular receiver, taken from [38]

The air from compressor stage enters the receiver through an inner chamber, and directed through a multitude of circular tubes into the absorber assemblies. Each spike (*Figure 6.3*) consists of two concentric tubes, where the inner tube supplies the cold air stream from the inner chamber to the spike tip (outermost point) from where the air flow is directed back by 180° towards the receiver center, passing through the outer tube. The outer tube's outer surface is exposed to the concentrated irradiation, and in the process heated up, transferring thermal energy into the inner air stream. To enhance the heat transfer the outer tube is internally finned. The fins describe multiple narrow passages of rectangular cross section. To enhance heat transfer and balance flux inhomogenity the fins may be of helical shape instead of straight fins. The spikes function as the heat exchangers, absorbing the concentrated irradiation and transferring the thermal energy onto the pressurized air stream. The heated air is passed on to the outer chamber from where it exits the receiver.
From the mathematical models done by [39] outlet temperature of the pressurized air could achieve 900°C.

6.2 Closed volumetric receivers

Volumetric receiver designs are based on absorber materials consisting of a multitude of porous interlocking shapes such as knit-wire packs, foam, honeycomb structures, packed beds and others with a specific porosity. The absorber material occupies a volume inside the receiver and is irradiated by concentrated solar radiation. The absorber material absorbs the solar radiation (energy) within the receiver material itself, thus heating up, increasing the effective area for absorption without increasing the area for heat loss. This large

absorption surface permits high solar fluxes at the receiver surface despite the low heat transfer coefficient of the air.
This effect causes one of the biggest advantages of volumetric solar receivers namely the increase of the heat transfer area and the consequent reduction of local flux density at the absorber surface. The HTF, which commonly is air, passes through the volume at the same time the solar energy is transferred via forced convection from the absorber material to the HTF.
Radiative heating of the HTF due to the effects of absorption and scattering of the impinging concentrated solar radiation inside the HTF are very small compared to the convective heat transfer and usually negligible according to [40].
The main advantage of volumetric receivers compared to tubular ones is the ability to absorb relatively high solar flux (high efficiencies for average flux 1000 kW/m^2 operate at high temperatures while still being compact [34].

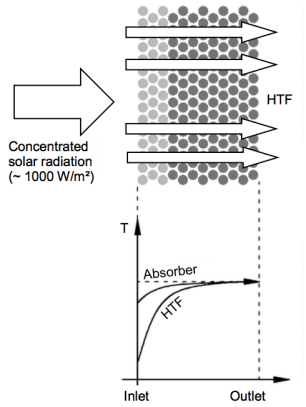

Figure 6.4 Temperature profile on a volumetric receiver, taken from [34]

Depending on the desired outlet temperatures of the HTF the material of the absorber can be of metals or ceramics. According to [41] volumetric receivers with metallic absorber are able to produce fluid outlet temperatures from 800°C to 1000°C, receivers with siliconized silicon carbide (SiSiC) ceramic absorbers temperatures of 1200°C, and receivers with silicon carbide (SiC) absorbers temperatures of 1500°C.

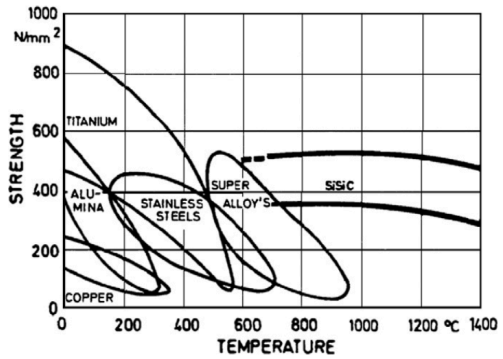

Figure 6.5 Bend strength of different material versus the material temperature, taken from [41]

The main problem regards the flow stability: in the flow through a porous sample, the mass flow density is determined by the pressure difference between the two sides of the sample. Instability occurs when a pressure drop causes different mass flow densities, and can therefore be related to different outlet temperatures.
The poor performance of some receivers is cause for concern. The prediction of outlet air temperatures of over 1000 °C for a variety of absorbers has not been completely fulfilled. Unstable gas flow through volumetric receivers can lead to local overheating and thus poor performance and local failures, such as melting or cracking [41].

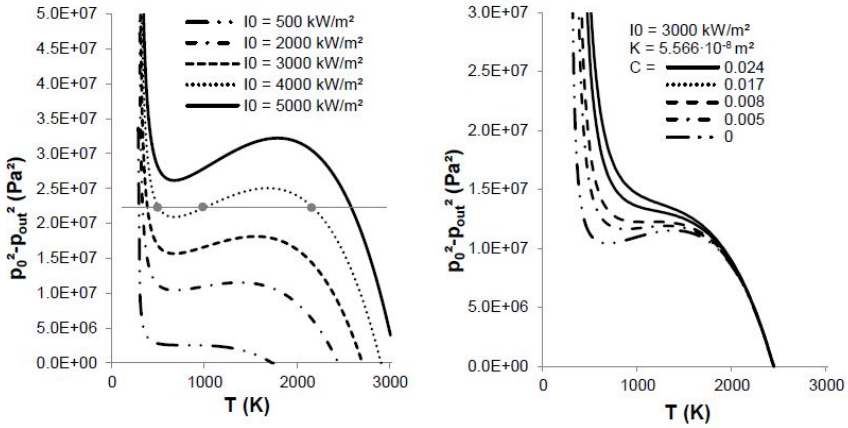

Figure 6.6 Pressure drop versus HTF temperature for different solar fluxes (on the left); for different inertial coefficients C (on the right) , taken from [41]

Pressure losses show a quadratic behavior (*Figure 6.6*); but this trend is strongly dependent on the absorber characteristics. In fact, highly porous structures (such as honeycomb structures, with higher C) present stronger instabilities, while other absorber types (wire mesh, ceramic foams) present a more stable trend (following the quadratic behavior).

As the receiver is to be used with pressurized air, it must be sealed, separating the high-pressure compressor air from the ambient air outside the unit. The aperture of the receiver is thus typically covered by a window of quartz glass, which is capable of resisting the high temperatures and pressures involved. In closed receivers, the presence of a glass cover implies an increase in optical losses due to reflection but will reduce convection losses from the receiver surface and re-radiation losses. *Figure 6.7* shows the working principle of two closed volumetric receivers.

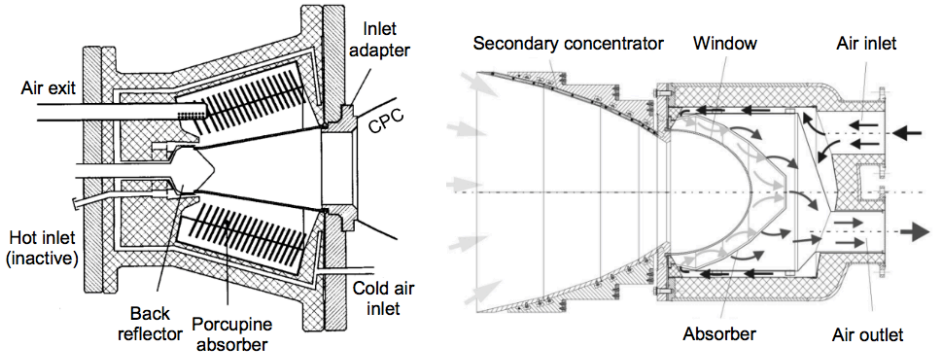

Figure 6.7 Closed volumetric receivers: on the left DIAPR, on the right REFOS, taken from [34]

The Receiver for Solar-Hybrid Gasturbine and CC Systems (REFOS) is a metallic absorber, developed in the REFOS project starting 1996 and also used within the SOLGATE project (starting 2001). The main components are the secondary compound parabolic concentrator (CPC) to increase the solar flux even more and to protect the receiver structure, the doomed quartz glass window that can withstand a pressure of 19.5 bar and additionally providing reduced reflectivity losses compared to a flat window, and the volumetric metallic wire mesh absorber.
Within the SOLGATE project the REFOS receiver was used as a medium and high temperature receiver. For the medium temperature application the metallic wire mesh absorber was maintained while the absorber in the high temperature receiver was replaced by a highly porous ceramic foam absorber. From the previous REFOS project problems with the quartz window were known and therefore an active multiple air jet window cooling was installed. In a test in spring 2003 air outlet temperatures of 960°C were reached before a problem in the gas turbine caused the test to stop. The active window cooling seemed to work keeping the window temperature well below the acceptable limit of 800°C [42]. Average flux was 550 W/m^2 while peak fluxes reached 800 W/m^2.

The Directly-Irradiated Annular Pressurized Receiver (DIAPR), first built by the Weizmann Institute of Science in 1992, is based on porcupine absorbers made of high temperature ceramics and it is the one used in the AORA field in Sevilla. It was developed by the Israeli Weizmann Institute of Science. The main components are the secondary compound parabolic concentrator (CPC) to increase the solar flux even more and to protect the receiver structure.
Experimental tests showed that the design is able to operate at pressures of 17 to 20 bar and solar fluxes between 2500 and 5000 kW/m^2 while creating HTF outlet temperatures of 1200°C for an extended time period of around 250 hours [43]. In these tests hundreds of heating and cooling cycles were passed through without noticeable local hot spots neither on the absorber nor on the window. The lack of hot spots and the fact the porcupines are mechanically independent allowing each element to expand as the temperature varies avoiding thermal stresses no failures appeared. The receiver efficiency was estimated to be between 70 and 90 percent during the tests.

Another interesting volumetric receiver successfully tested is the Reticulate Porous Ceramic (RPC) foam cavity receiver, especially created for solar micro gas turbines. In fact maximum measured air outlet temperature are about 1100°C at absolute operating pressure of 5 bars (and average incident solar flux of 4360 W/m^2) [44]. For MW power applications, modular configuration are possible, consisting of an array of solar receivers, each at a power level of about 50–100 kW. RPC has also being tested at the solar research facility of the Weizmann Institute of Science, Israel [45].

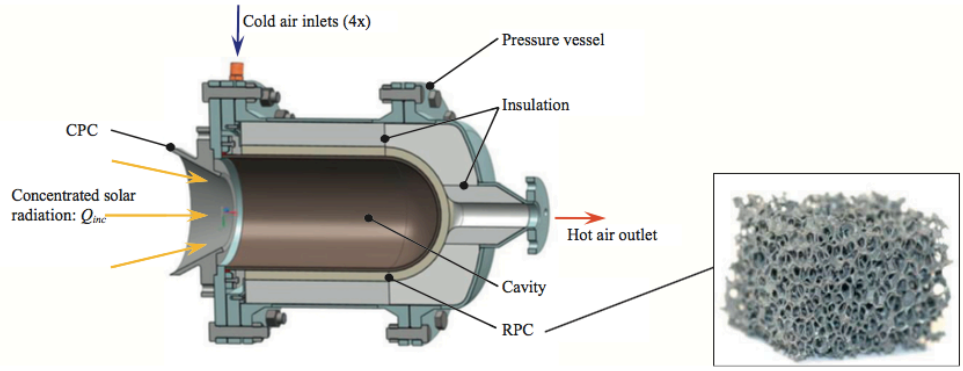

Figure 6.8 Volumetric receiver: RPC, taken from [46]

Resume

From the above considerations, Table 3 resumes the possible receivers to implement in a solar plant coupled to a Brayton cycle today.

Table 3 Currently working solar receivers

Name	Type	Material	Max T_{air} [°C]	Max.average flux [kW/m^2]	DP_{max} [mbar]	Measured η [-]
SOLHYCO	tubular	Nickel alloys	800	200	100	0.7-0.8
SOLUGAS	tubular	Nickel alloys	650	200	150	0.8-0.9
REFOS	closed volumetric	Metallic (Inconel 600) with quartz window	900	1000	18	0.8-0.9
DIAPR	closed volumetric	Ceramic (aluminia-silica)	1200	2000	25	0.7-0.9
RPC	closed volumetric	Ceramic	1000	1000	100	0.9

Receiver's model

Two main constraints make the volumetric receiver the one to adopt for this project:

- The high flux arriving on the receiver (as exposed in Figure 5.15)
- The optimal 950°C TIT for turbines of this size [47]

It is very hard to find an accurate thermal model for a volumetric receiver. A lot of papers are available today, but none has been confirmed yet by experimental results. Nevertheless a thermal efficiency curve adapted from [44] and [21] is considered and included in the model through a polynomial fitting. Figure 6.9 shows thermal efficiency as a function of air outlet temperature (at the exit of the receiver) and incident power at the CPC entrance in the range of 24-624 kW, since 624 kW is the design point, based on the highest irradiated day.
In off-design conditions, receiver heat losses are assumed to be dependent on mean air temperature only; as a consequence the thermal efficiency decreases together with the incident flux.

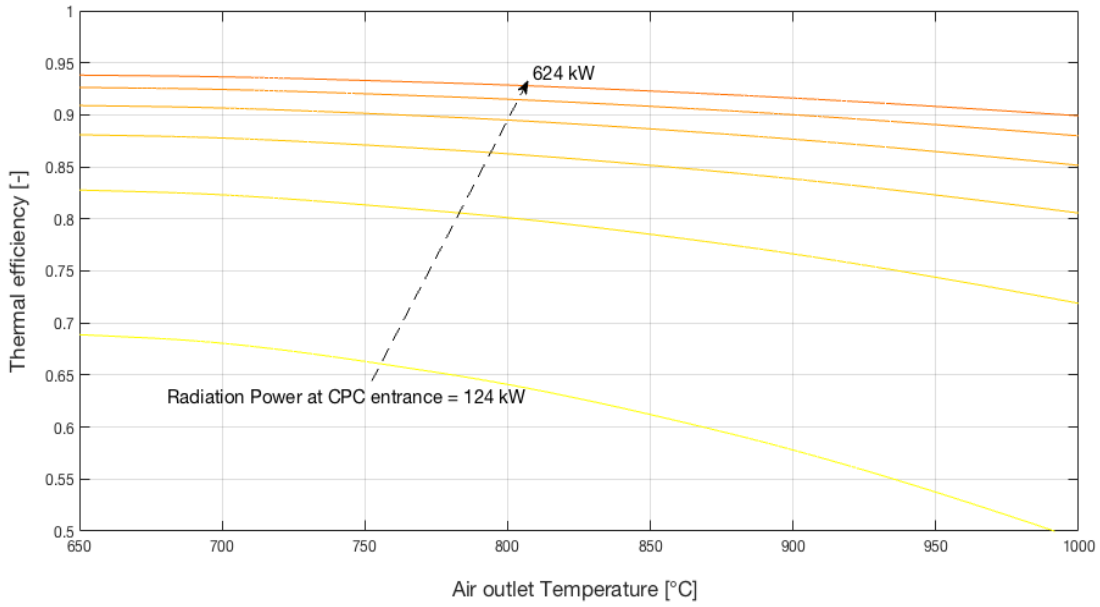

Figure 6.9 Receiver thermal efficiency, adapted from [21]

Pressure drop caused by the air passage through the volumetric receiver influences as well the engine performances. In fact, in design conditions pressure drop was set equal to 0.2 bar as suggested by [44]; while the off-design pressure drop is computed through the Dupuit-Forcheneimer relation developed to predict fluid pressure drop through a porous material. Once the foam viscosity coefficient (K), the Dupuit-Forcheneimer coefficient (F) and foam cross section area (A) are known and assumed constant in part-load operation, the off-design pressure drop of receiver is computer with the following relation:

$$\Delta P_{off} = \Delta P_{on} \frac{\left[\frac{\mu m}{K \rho A} + \frac{F m^2}{\rho A^2}\right]_{off}}{\left[\frac{\mu m}{K \rho A} + \frac{F m^2}{\rho A^2}\right]_{on}} \tag{6.1}$$

7. Gas turbine model

7.1 Introduction

The performances of the solar field and of the thermal receiver have now been defined. Nevertheless the other components still need to be investigated.
As previously said, the solar micro-gas-turbine here modeled is in a recuperative configuration. The combustor is present to allow fuel-integration, even if not used in on-design conditions. The system layout is visible in Figure 7.1. Resuming, ambient air passes through a filter (1-2), is compressed (2-3), is pre-heated (3-4), passes through the solar receiver (4-5), through the combustor (5-6), is expanded in a single stage (6-7), and then the exhausted air (and fuel if the combustor is used) is cooled down in the recuperator (7-8) and released to the ambient (8-9). The net mechanical power is converted by the generator into electric energy that is sent to the grid.

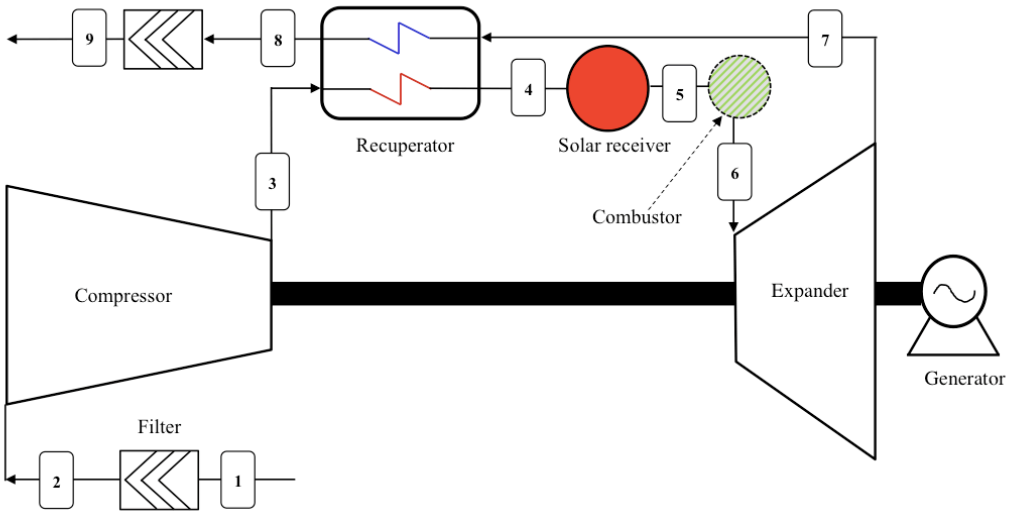

Figure 7.1 Solar micro-gas turbine layout with streams identification numbers

A characterization of the performance of the various components in on-design and off-design conditions is necessary to assess the system yearly performance.
Indeed some values are strongly variable through time: the DNI, the solar incidence angle on the heliostats-field (affecting the optical efficiency) and the ambient air temperature. For these reasons solar plants often work at part-load, and it is necessary to proceed with the detailed dimensioning of each component in order to work in safe conditions, and in optimal conditions (that can have a different meaning depending on the strategy adopted).
The model of the performances of the turbine, the generator and the recuperator are taken and adapted from a similar analysis made by Giostri [28]. Some modifications were necessary since the model was based on a two-shaft-turbine-configuration, the on-design power was lower (32.9 kWe), the maximum TIT was higher (1100°C), and no-hybridization was considered.

7.2 The turbine engine model

Several characteristic values are commonly used in turbomachinery for defining significant performance criteria. Similarity considerations show that actually only four parameters are sufficient to describe completely the characteristics: the Mach number, the Reynolds number and two characteristic velocity ratios. For the choice of the two latter ratios, practical considerations (dealing with the design aspect of turbomachines) indicate parameters containing the rotor diameter and the rotational speed: the specific diameter D_s and the specific speed N_s.

$$Re = \frac{\rho V D}{\mu} \tag{7.1}$$

$$Ma = \sqrt{\gamma R T} \tag{7.2}$$

$$D_s = \frac{D\ gH^{1/4}}{Q^{1/2}} \tag{7.3}$$

$$N_s = \frac{N\ Q^{1/2}}{gH^{3/4}} \tag{7.4}$$

Where D_s and N_s are dimensionless while: rotational speed N [rpm], rotor flow rate Q [feet^3/s], adiabatic head gH [feet], and diameter D [feet].

It is difficult to present the performance of any machine as a function of four parameters at one time. Fortunately, two of these variables, namely Reynold's number Re and Mach number Ma have only a secondary effect on turbomachine performance; if the Reynolds number is above 106 for turbines and compressors the effect of Reynolds number is very nearly constant which eliminates this variable; whereas if the Mach number of the machine is less than or near 1.0 the compressibility effects are negligible which eliminates this variable, and turbomachine performance can be presented as a function of only two parameters: specific speed N_s and specific diameter D_s.

In this way, given an existing commercial turbine, with its diameter and its operational rotational speed, by using Balje diagrams (*Figure 7.2*), an estimation of optimal N_s and D_s can be found to obtain a certain level of efficiency of the turbine (and compressor).

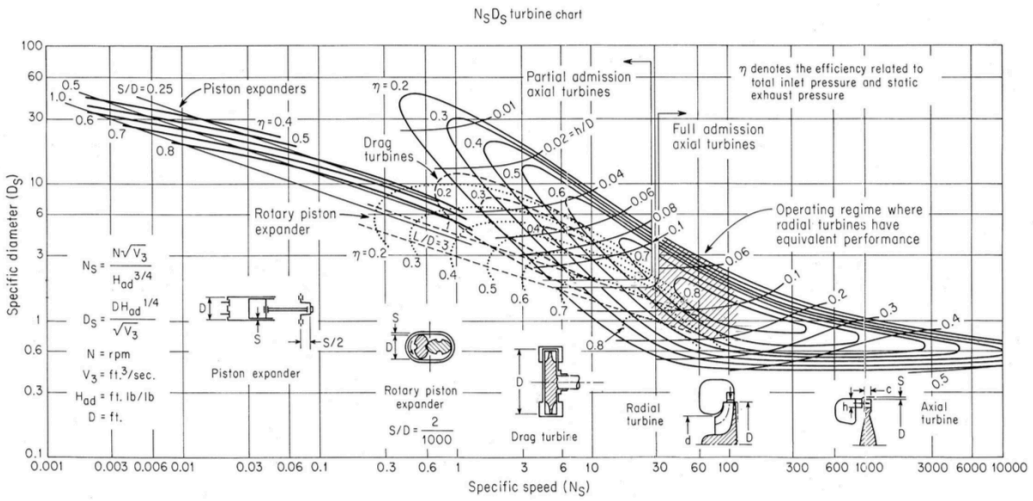

Figure 7.2 Balje diagram for a turbine, taken from [49]

The typical values of micro-gas-turbines (N_s around 50 and D_s around 2-3) bring to the choice of a Radial Turbine, and since most of the commercial turbines have lower power outputs than the one desired for this thesis, only three turbines are appropriate alternatives:

- Turbec MT 100
- Capstone C 200
- Ingersoll Rand MT 250

The adoption of small micro gas turbine engine implies high rotating speed of turbomachinery. This involves that the generator output is high frequency AC and has to be flattened to DC by a rectifier and subsequently converted to grid frequency AC (i.e. 50 – 60 Hz) by an inverter. The design performance of this three-step process is made assuming conversion efficiencies equal to 96.0% for both generator and power control system (PCS) while the organic efficiency is set to 98.0%.

The model of the micro gas turbine for off-design performance is based on the utilization of normalized performance maps (relatively to on-design condition) and the assumption that the engine is arranged in a single shaft layout (i.e. same shaft speed for compressor and turbine).
This approach is based on similarity and dimensional analyses and is widely used in turbomachinery. The corrected variables used are the corrected mass flow rate m and the corrected speed:

$$m_c = \frac{m\sqrt{T_{in}}}{p_{in}} \tag{7.5}$$

$$N_c = \frac{N}{\sqrt{T_{in}}} \tag{7.6}$$

The compressor map is defined as a two-dimension function that are the pressure ratio and the isoentropic efficiency as a function of inlet corrected rotational speed adimensionalised by the on-design-values:

$$m_{CR} = \frac{m_c}{m_{c\_on}} \tag{7.7}$$

$$N_{CR} = \frac{N_c}{N_{c\_on}} \tag{7.8}$$

Figure 7.3 (left) presents the characteristic map of a single stage centrifugal compressor, the choke line and surge line, which contain the feasible operational area, are highlighted. In addition iso-efficiency lines are reported.
Figure 7.3 (right) reports the isentropic efficiency as function of dimensionless corrected mass flow and dimensionless corrected rotational speed.

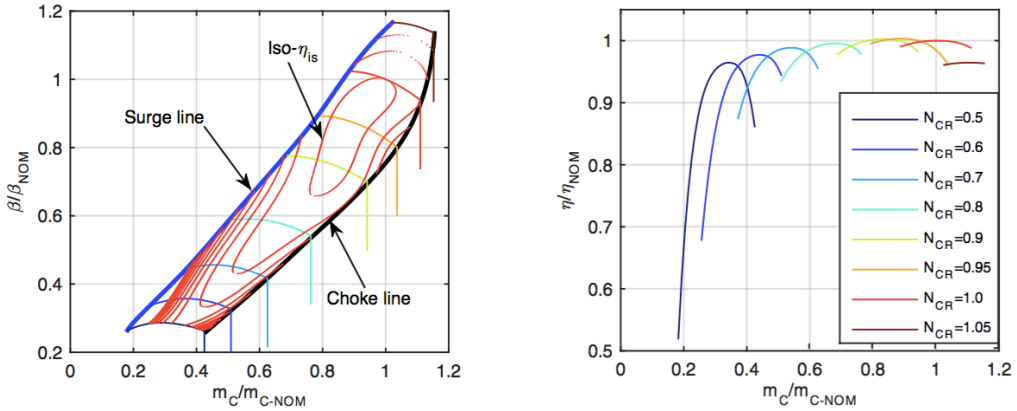

Figure 7.3 Characteristic map (left) and isoentropic efficiency trend of the centrifugal compressor (right), taken from [21]

In order to avoid compressor surge, a common approach resides in the definition (Steyn, 2006) of a surge margin (here chosen to be 2%) that has not to be overcome during operation.

$$SM = \frac{m_{r_{surge}} - m_{r_{working}}}{m_{r_{working}}} \tag{7.9}$$

In accordance with the compressor, the expander off-design behavior is modeled by specific relation that links inlet corrected mass flow and expansion ratio together (*Figure 7.4* left). As regards the expander isentropic efficiency, it is expressed by a function of pressure ratio (*Figure 7.4* right).

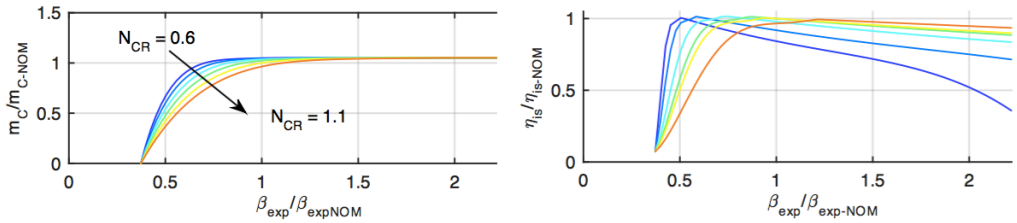

Figure 7.4 Characteristic map (left) and isentropic efficiency trend (right) of the representative radial turbine. Drawn lines represent reduced rotational speed range 0.6 – 1.1 (step equal to 0.1), taken from [21]

The main assumption is that the turbomachinery rotational speed varies in order to maintain a certain TIT.

7.3 Generator and power control system model

The design performance are based on conversion efficiencies equal to 96.0% for both the generator and the power control system and equal to 98.0% for the organic efficiency.
The efficiency decay in part-load operation are computed in accordance with the relation proposed by [50] (visible in *Figure 7.5*).

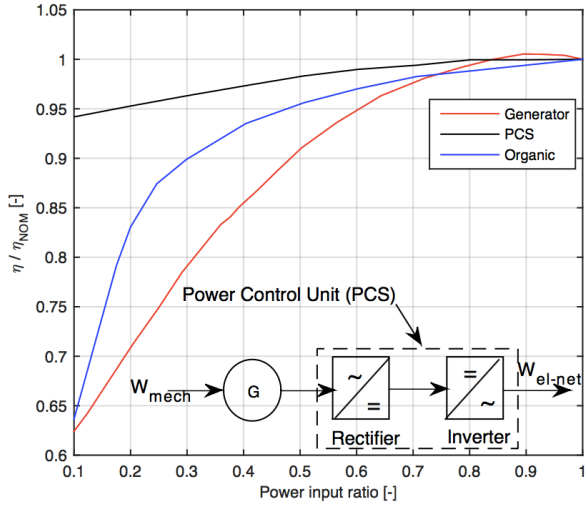

Figure 7.5 Electric and organic efficiencies decay at partial load (Adapted from (Campanari, 2000), taken from [21]

7.4 Recuperator's model

Micro turbines in a simple Brayton cycle are not competitive due to their very low efficiency. This is why most of the micro turbines, work in a recuperative cycle, reaching efficiencies of the same order of higher-output-turbines. The principle of the recuperator is to use the available heat at the exit of the turbine, to increase the temperature of air exiting the compressor.

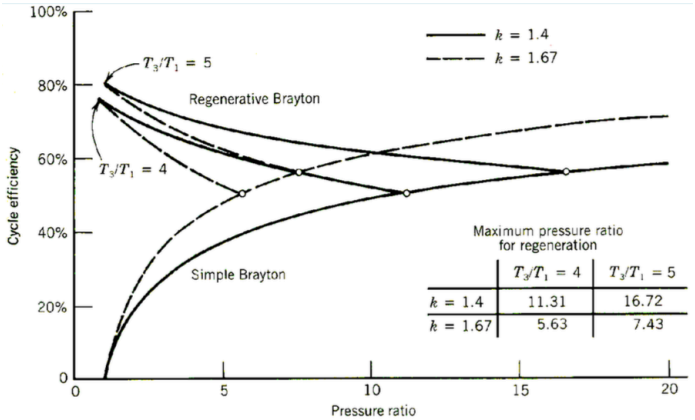

Figure 7.6 Brayton cycle efficiciency for microturbines, taken from [3]

Materials for the recuperator may be categorized by their maximum operating temperature (given by the Turbine Outlet Temperature). Indeed, based on the materials properties, there are limits to avoid recuperator's failure, such as corrosion, oxidation, creep, and strength; numerous experimental results have been analysed by [51].
Generally speaking, metallic alloys are applicable for lower temperatures: up to 675°C using conventional stainless steels, up to 750°C using Super 347 and up to 800/900°C using advanced austenitic stainless steels; while ceramics are applicable for temperatures higher than 900°C (but their cost is significantly higher as well, so they are less commonly used; in fact most of the companies that investigated these large-size ceramic recuperators are no longer in the field).
A conventional stainless steel recuperator will e considered, in an annular wrap-around layout to guarantee the highest level of compactness (required by the MGT placed on top of the tower). Recuperator is then modelled as a counter-flow heat exchanger.
The recuperator is modelled as a counter-flow heat-exchanger, which is characterized by an effectiveness, defined as the ratio between the heat transfer rate and the maximum possible heat transfer rate and the maximum possible heat transfer. For the on-design a value of 0.895 is used, following the Capstone Report on the C200 turbine [52].
Moreover pressure drop is assumed to be 1.3% for the cold side and 2.7% for the hot side.
Part-load modelling of recuperator considers a variation in the heat transfer coefficient which depends on the Reynolds number *(7.10)* and a variation on the pressure drop *(7.11)*.

$$\frac{(UA)_{off}}{(UA)_{on}} = [\frac{(m_{hot})_{off}}{(m_{hot})_{on}}]^2 \tag{7.10}$$

$$\Delta P_{off} = \Delta P_{on} \frac{(\frac{m^2}{\rho})_{off}}{(\frac{m^2}{\rho})_{on}} \tag{7.11}$$

7.5 Combustion chamber's model

Capstone microturbines use a lean premix combustion system to achieve low emissions levels at a full power range. Lean premix operation requires operating at high air-fuel ratio within the primary combustion zone. The large amount of air is thoroughly mixed with fuel before combustion. This premixing of air and fuel enables clean combustion to occur at a relatively low temperature. Injectors control the air-fuel ratio and the air-fuel mixture in the primary zone to ensure that the optimal temperature is achieved for the NO_X minimization. The higher air-fuel ratio results in a lower flame temperature, which leads to lower NO_X levels. In order to achieve low levels of CO and Hydrocarbons simultaneously with low NO_X levels, the air-fuel mixture is retained in the combustion chamber

for a relatively long period. This process allows for a more complete combustion of CO and Hydrocarbons [53].

Hybrid operation with solar energy and fossil fuel supply simultaneously is enabled by a combustor installed in series with the solar receiver. In this case, mass and energy balance equations for the combustor are incorporated into the model, introducing an additional pressure drop term (2% of the combustor inlet pressure and proportional to the squared mass-flow-rate). No thermal losses in the combustor are considered, as they tend to be highly efficient (0.99 and more). The fuel share is defined as:

$$F_{fuel} = \frac{Q_{in\_fuel}}{Q_{in\_solar\_field} + Q_{in\_fuel}} \tag{7.12}$$

Where $Q_{in\_solar\_field}$ and Q_{in_fuel} are the heats entering the thermodynamic cycle, defined as it follows:

$$Q_{in\_solar\_field} = Q_{sun} * \eta_{opt} * \eta_{therm} = m_{air} * (H_5 - H_4) \tag{7.13}$$

$$Q_{in\_fuel} = m_{fuel} * LHV \tag{7.14}$$

The m_{fuel} corresponding to a given F_{fuel} is found by solving the balance of enthalpy in the combustion chamber:

$$\begin{aligned} m_{air}(H_{in_{air}} - H_{0_{air}}) + m_{fuel}\left(H_{in_{fuel}} - H_{0_{fuel}}\right) \\ = m_{mixt}\left(H_{out_{mixt}} - H_{0_{mixt}}\right) + m_{fuel} * LHV \end{aligned} \tag{7.15}$$

Where $H_{in_{air}}$ and $H_{in_{fuel}}$ are the inlet enthalpy of air and fuel (at point 5 of the cycle), $H_{out_{mixt}}$ is the enthalpy of the mixture (at point 6 of the cycle, corresponding to the turbine inlet), and H_0 are the enthalpies of the various mixtures at the reference conditions (25°C and 101325 Pa).

At the exit of the combustor, the working fluid has a different composition than the initial air, thus $H_{out_{mixt}}$ is strictly dependent on the quantity of fuel injected. Starting from an initial assumption that $H_{out_{mixt}}$ is equal to the enthalpy of only air at the required TIT, an iterative process is implemented to find the correct m_{fuel}.

When hybridization is present, speaking about "solar-to-electric efficiency" has no more sense. The most relevant index in this case becomes the annually averaged overall efficiency:

$$\eta_{overall} = \frac{E_{net}}{E_{fuel} + E_{solar}} \tag{7.16}$$

Where E_{net} is the annual energy produced (kWh), E_{solar} is the annual solar energy input and E_{fuel} is the total fuel heat input in a year. These two last parameters are defined as follows:

$$E_{fuel} = M_{fuel} * LHV \tag{7.17}$$

$$E_{solar} = A_{tot,mirrors} * \sum_{t=0}^{8760} DNI(t) \tag{7.18}$$

On-design parameters

Ensuing the components choice, all the assumptions required to solve the system in on-design conditions are reported in Table 4:

Table 4 Resume of on-design parameters

	Symbol	***Value***	***Unit of measure***
Ambient Conditions			
Ambient temperature	T_{amb}	35	°C
Ambient pressure	P_{amb}	101325	Pa
Direct Normal Irradiance	DNI	950	$W.m^2$
Heliostats field			
Number of mirrors	-	52	-
Mirror Length	H	4	m
Mirror Width	W	4	m
Mirror reflectivity	ϱ	0,94	-
Optical errors	σ	3	mrad
Shape	-	spherical	-
Receiver			
Receiver absorbance	α	0,99	-
Sizing pressure drop	ΔP	0,2	bar
Viscosity coefficient	K	45	m^{-1}
CPC surface reflectivity	ϱ	0,94	-
CPC surface slope error	σ	3	mrad
rim angle	θ	35	°
Absorber diameter	D_{abs}	0,75	m
Aperture diameter	D_{aper}	1,3	m
Shape	-	conical	-
Thermal engine			
Turbine inlet temperature	TIT	950	°C
Air intake pressure drop	Δp_{inlet}	0,5	%
Compressor pressure ratio	$\beta_{compressor}$	4,1	
Isentropic efficiency compressor	$\eta_{is\text{-}compressor}$	81	%

Mechanical efficiency compressor/turbine	$\eta_{mechanical}$	98	%
Isentropic efficiency turbine	$\eta_{is\text{-}turbine}$	84	%
Recuperator effectiveness	ε	89,5	%
Recuperator pressure drop (hot side)	$\Delta p_{rec\text{-}hot}$	2,7	%
Recuperator pressure drop (cold side)	$\Delta p_{rec\text{-}cold}$	1,3	%
Air out-take pressure drop	Δp_{outlet}	1	%
Receiver pressure drop	$\Delta p_{receiver}$	5	%
Generator efficiency	η_{gen}	96	
Inverter efficiency	η_{inv}	96	%
Rotational speed	n	45 000	rpm

8. System results

After the definition of the parameters and the assumptions behind all the components interacting in the power plant, this chapter illustrates the results of the working conditions of the plant.

8.1 On-design performances

The on-design system described previously gives a thermodynamic cycle visible in Figure 8.1 and the outputs reported in Table 5.

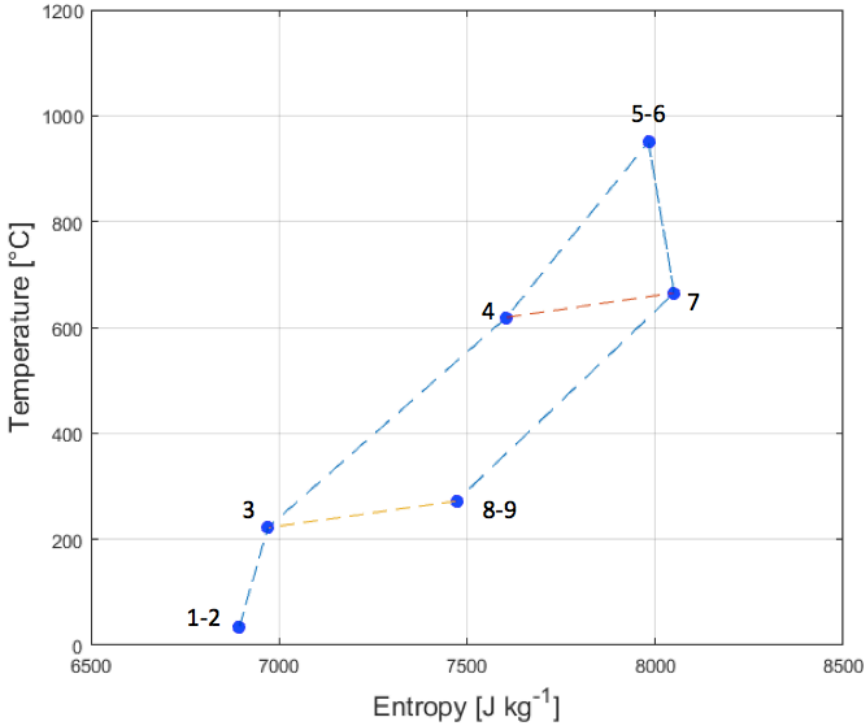

Figure 8.1 T-S diagram of the on-design cycle

Table 5 Performances in on-design conditions

Air mass flow rate	m_{air}	1,49	kg/s
Fuel share	F_{fuel}	0	-
Power from the sun	Q_{sun}	789,87	kW_{th}
Optical efficiency	η_{opt}	79	%
Incident heat on the receiver	Q_{inc}	624	kW_{th}
Thermal efficiency receiver	$\eta_{therm-rec}$	90,96	%
Net power block efficiency	η_{PB}	32,99	%
Net power	P_{el-net}	187,25	kW_{el}
Solar to electric efficiency	η_{sol-el}	23,71	%

8.2 Exergy analysis

Exergy (or second-law) analysis is considered to be a fundamental tool able to offer information to study the performance of energy systems and to complement the outcomes from energy analysis. The irreversibilities associated with real processes leads to a degradation of the energy quality that can be assessed by second law analysis. Focusing on the solar micro-gas-turbine, the sources of irreversibility are represented by: i) optical losses of the concentrator, ii) conversion of radiation energy to thermal energy in the receiver, iii) heat transfer through finite temperature difference in the regenerator, iv) gap between isentropic process and real process in turbomachinery, v) fluid mechanical friction, vi) conversion of Euler work to electricity (i.e. mechanical and electrical losses) and vii) hot air discharge at TET higher than ambient temperature.
The exergy content of the solar radiation (EX_{sun}) has been object of specific research studies that have produced different formulae for calculation of thermal radiation exergy. In [54], an ample literature review and discussion about different models presented in literature is exposed, nevertheless, the difference among the models, although highly significant from a theoretical point of view, shows a small range of uncertainty. Taking into account studies related to exergy analysis applied to CSP plant ([55] and [56]) the following relation is undoubtedly the most used:

$$EX_{sun} = A_{aperture} * DNI * (1 - \frac{4}{3} * \frac{T_{amb}}{T_{bb}} + \frac{1}{3} * \left(\frac{T_{amb}}{T_{bb}}\right)^4) \quad (8.1)$$

Where T_{bb} is the apparent temperature of a black blody (5800 K). After the definition of ambient reference condition (dead-state, corresponding to 101325 Pa and 35°C), physical exergy associated with a flowing stream is defined as follows (both kinetic and potential energies are neglected):

$$EX_{ph} = m * [(h - h_{amb}) + T_{amb} * (s - s_{amb})] \quad (8.2)$$

The irreversibilities that occur in real steady-state transformation imply a destruction of exergy (related to entropy generation) that is calculated with the following relation:

$$EX_{ds} = \sum_{i=1}^{\#in} m_i EX_{ph,i} - \sum_{j=1}^{\#out} m_j EX_{ph,j} + \sum_{k=1}^{\#heat\ flux} Q_k \left(1 - \frac{T}{T_k}\right. \quad (8.3)$$

$$= T_{amb} \Delta S_{gen}$$

In order to identify the impact on the energetic performance of each transformation occurring in each component, it is useful to compute the efficiency decay (Δη) as follows:

$$\eta_{II} = \frac{W_{el}}{EX_{sun}} = 1 - \sum \frac{EX_{ds}}{EX_{sun}} \tag{8.4}$$

In Table 6 exergy analysis outputs are reported; the resulting second law efficiency is equal to 25.49%. This latter value is different than the sun-to-electric efficiency (23.71%); this is imputable to the different denominator in efficiency definition; in particular, exergy associated to solar radiation is slightly lower than DNI as underlined by (*8.1*). Nevertheless, the second law analysis shows its own potential through the possibility to identify the efficiency decay introduced by each transformation.

Table 6 Exergy analysis outputs

	Δη II [%]
Solar exergy	-
Air intake	0.09
Compressor	4.72
Recuperator	3.44
Optical loss	21.05
Receiver	25.26
Combustor	0
Expander	4.30
Turbine outlet	0.18
Mechanical	0.56
Inverter	2.17
Hot air discharge	12.73
Overall	74.51

Notice that the final second-law-efficiency (which is the sum of the second-law-efficiency of the various components) must satisfy the balance *(8.4)*.
Based on the upwards results, a Sankey diagram can be drawn thanks to [57] to show the exergy losses through the system (*Figure 8.2*). As it can be quickly seen, the main losses are: the optical ones, the receiver's ones and the one due to the recuperator (hot discharge). Hence, to improve the system it would be interesting to focus on the mirror's quality (optical efficiency), on the receiver's design (thermal efficiency), on increasing the TIT in the cycle (in the receiver's losses are included also the ones related to the exchange of heat at different temperatures) and on the recuperator's effectiveness.

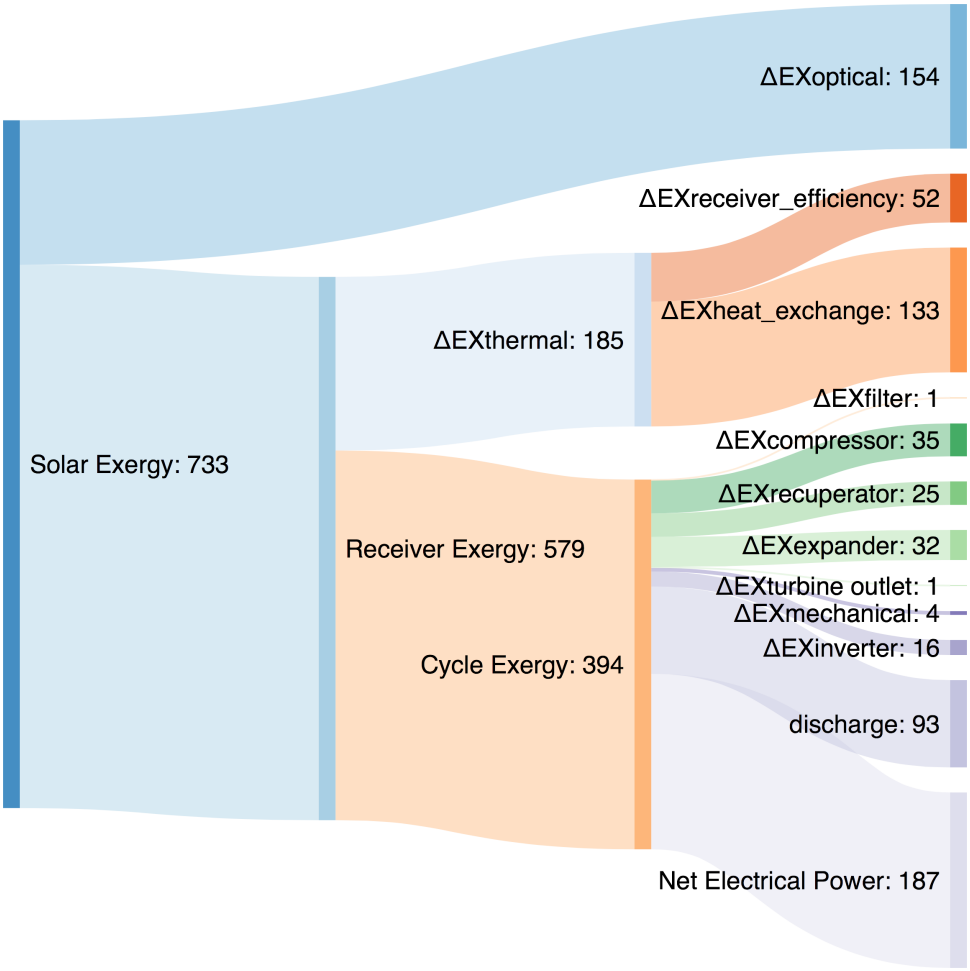

Figure 8.2 Sankey diagram of second law losses analysis

8.3 Operational maps

The overall simulation of the power block is done in Matlab, using the KINSOL solver, to accelerate the computational time. An alternative fuel share definition is defined in this section:

$$\beta_{fuel} = \frac{\Delta T_{combustor}}{\Delta T_{combustor} + \Delta T_{receiver}} \tag{8.5}$$

Where $\Delta T_{combustor}$ is the temperature increment given by the combustion chamber and $\Delta T_{receiver}$ is the temperature increment given by the solar receiver. β_{fuel} is different than F_{fuel} that is based on the fraction of heat and not on the temperatures.

For each β_{fuel} an optimal map is drawn, on the basis that the turbine inlet temperature TIT is the control parameter in order to maximize the system

power output for each ambient condition (characterized by the values of DNI and ambient temperature). The control system acts on rotational speed of turbomachinery in order to fulfill the operational constraints of each component.
From a computational point of view, the developed algorithm carries out a parametric analysis varying the TIT (and thus the rotational speed of the turbomachinery) and selecting the case with highest net power output without incurring in component constraints violation.
The constraints used are:
-mass flow rate at the compressor must be higher than the one of stall condition (surge margin is 2%)
-mass flow rate at the compressor must be lower than the one of choke conditions
-mass flow rate at the turbine must be lower than the blocking one
-expansion pressure ratio must be lower than the blocking one
-maximum power allowed is 15% more than the design power
-minimum power allowed is 10% of the design power
-maximum temperature of the recuperator must not overcome 700°C

The effective DNI is defined as it follows:

$$DNI_{effective} = DNI * \frac{\eta_{opt}}{\eta_{opt\_design}} \tag{8.6}$$

In Figure 8.3 is reported the trend of the system power when running in solar-mode, for a DNI_{eff} of 360 W/m^2 and a T_{amb} of 15°C, varying the TIT (and thus the rotational speed) of the system. The recuperator mean temperature (average between inlet of the hot side and outlet of the cold side) is reported as well, highlighting the maximum limiting 700°C. In facts, for low DNI the principal constraint blocking the system is the recuperator maximum temperature, hence for a fixed ambient temperature, a reduction of the TIT (with respect to the design 950°C) is necessary.

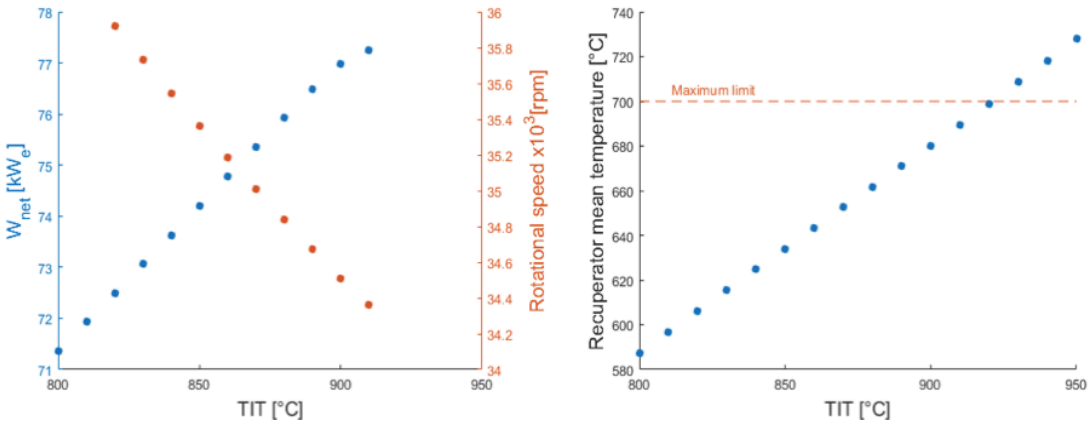

Figure 8.3 System power output and turbomachinery rotational speed (left) and recuperator temperature (right) for DNI_{eff} 360 W/m^2 and T_{amb} 15°C, in function of the TIT

In hybrid operations, the system constraint of mass flow rate at the compressor (which is the choke limit) intervenes at high DNI_{eff}. Figure 8.4 shows at an ambient temperature of 35°C, and a system TIT of 950°C, the power output and reduced mass flow rate at the compressor in function of the DNI_{eff}. NB: the power output is slightly lower at high DNI, because of the combustor losses weight (in those conditions a lower fuel share would be more efficient).

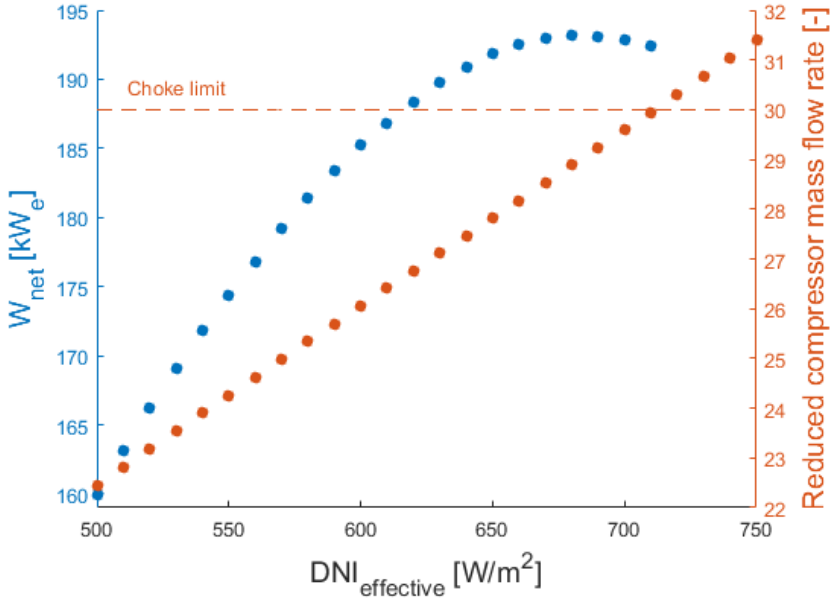

Figure 8.4 System power output and reduced compressor mass flow rate for θ_{fuel} 20%, T_{amb} 15°C, and TIT 950°C, in function of the DNI_{eff}

Finally, another consideration can be done for high values of DNI (close to the design one) and low ambient temperatures; in these cases the resulting TIT is lower than 950°C because of the maximum power constraint (that can't exceed 15% of the design one).

For the sake of accuracy, the matrix (representing the operational map) is evenly spaced in steps of 10 W/m^2 for the effective DNI and 5°C for the ambient temperature in the entire operative range (respectively from 200 W/m^2 to 800 W/m^2 and from 5°C to 40 °C); NB: the DNI reported in the maps is the effective one (normalized on the optical efficiency, hence lower than the actual DNI (*8.6*)).

The TIT considered vary from 950°C to 800°C for the solar-only-mode and from 950°C to 850°C for the other maps (with a step of 10°C); this latter interval reduces the operational maps of the system when using hybridization, but in these cases (happening at low DNI), more fuel is burned to approach the design TIT (of 950°C) rather than having a lower TIT at a lower fuel share.

A single map (that is for a given β_{fuel}) has a computational time of 4 hours (using the Kinsol solver).

Figure 8.5 represents the solar-only operational map: chart area is colored with TIT values that optimize system performance (maximum power) in function of the effective DNI and ambient temperature; in addition iso-solar-to-electric efficiency and iso-net power lines are presented.
Figure 8.6 and *Figure 8.7* represent operational maps for various β_{fuel} (from 10% to 60%); only optimal TIT is represented.

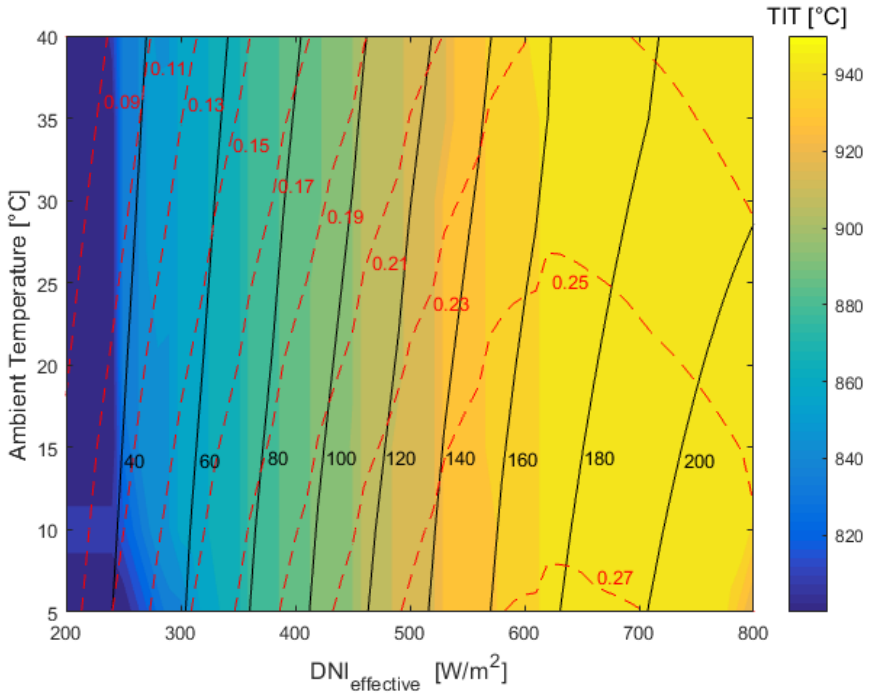

Figure 8.5 Part load map of the solar-only system. Iso-W_{net} black lines (in kW) are shown, while Iso-η_{sol-el} dashed red lines (in -) are shown

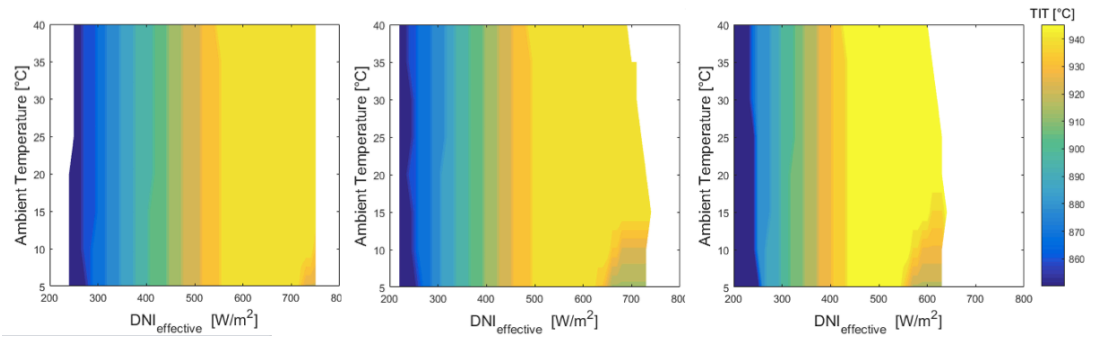

Figure 8.6 Part load map of the system for different β_{fuel} (10% on the left, 20% in the middle, 30% on the right)

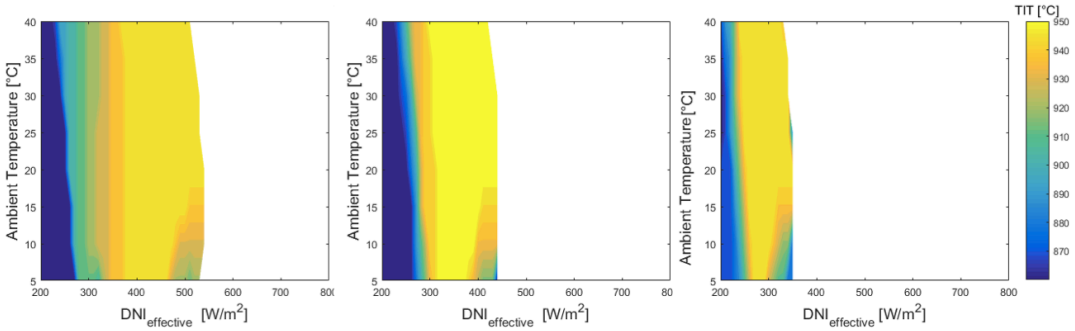

Figure 8.7 Part load map of the system for different θ_{fuel} (40% on the left, 50% in the middle, 60% on the right).

Previous maps are drawn on the basis of maximum power output, and the selected TIT is chosen accordingly. Whereas for high DNI, the condition of maximum power corresponds to the one of maximum efficiency, it is not true for lower DNI. In facts, it might be more convenient to operate at higher TIT from a cycle efficiency point of view with respect to the nominal power one. Thus, additional maps based on the maximum efficiency are drawn.

All these maps are with respect to an on-design system characterized by a DNI_{eff} of 750 W/m^2, corresponding to the most irradiated day of the year in Sevilla. This means that unless using constantly a fuel-integration, the turbine (and the entire system) will mostly work in part-load mode, having an impact also on the economic point of view.
Thusly, an alternative designed at a lower DNI would be interesting to investigate. For example, a DNI_{eff} of 675 W/m^2 would allow to work when DNI is maximal (because within the limit of the extra 10% power for the turbine) and to work more hours on on-design conditions (with a cheaper design). NB: the rated power output would be lower, and all operational maps would consequently change.

8.4 Test cases

Using the operational maps obtained, it is possible to know for each condition of DNI_{eff} and T_{amb} the system outputs at each hybridization level; performances of the system are complex as they entrain various thermodynamic phenomena that oppose one to another, thus contradistinctive behaviors are noticed and explained in the following lines. For low levels of sun's irradiation, an increase of fuel integration leads to both an increase on power produced and on cycle efficiency. Whereas for higher values of DNI, there might be a maximum point in cycle efficiency for a precise hybridization level, or the cycle efficiency might be monotonically decreasing (while the net power output keeps increasing). These trends depend on many factor, thus a detailed analysis of some operating conditions are exposed. In all the following figures, nominal

power and nominal cycle efficiency (referring to the same T_{amb} but to the nominal DNI_{eff}) are drawn in dashed lines.

First case is at the design conditions: ambient temperature of 35°C and effective DNI of 750 W/m^2. As it can be seen in *Figure 8.8* on the left side, as soon as fuel is injected in the system, cycle efficiency drops whereas net power only slightly increases. This is due to various factors. In facts, mass flow rate increases of 10%, augmenting pressure drops as well. Moreover since the pressure ratio increases too, from the compressor maps on the right side of *Figure 8.8* isentropic efficiency drops of 3%.

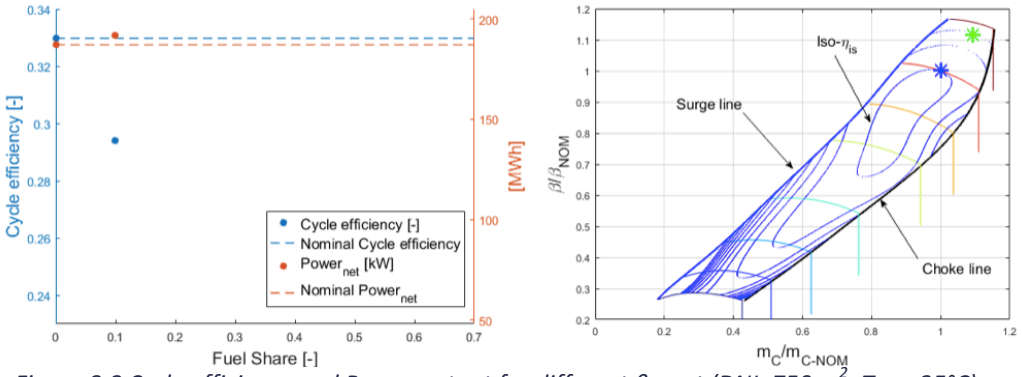

Figure 8.8 Cycle efficiency and Power output for different β_{fuel} at (DNI=750 m^2; T_{amb}=35°C) on the left and compressor map on the right (blue star is the nominal condition, green star is at β_{fuel} 10%)

Second case is still at 35°C, to avoid the effects of temperature on the cycle and an effective DNI_{eff} of 650 W/m^2. Again as hybridization increases, net cycle efficiency drops. It is interesting to analyze the point for which the heat entering the cycle equals the one of the nominal condition (same ambient temperature but with the design DNI); this case occurs when β_{fuel} is of 11.24%. What is observed is that for the same heat, the resulting mass flow rate is 2% lower than the optimal case one, thus the power is lower. This is due to many reasons: the thermal losses in the receiver are higher for a lower sun radiation, thus the outlet temperature of the solar receiver is lower; the internal combustion leads to the change of flow composition at the exit of the combustor, and the use of the combustion chamber leads to additional pressure losses.

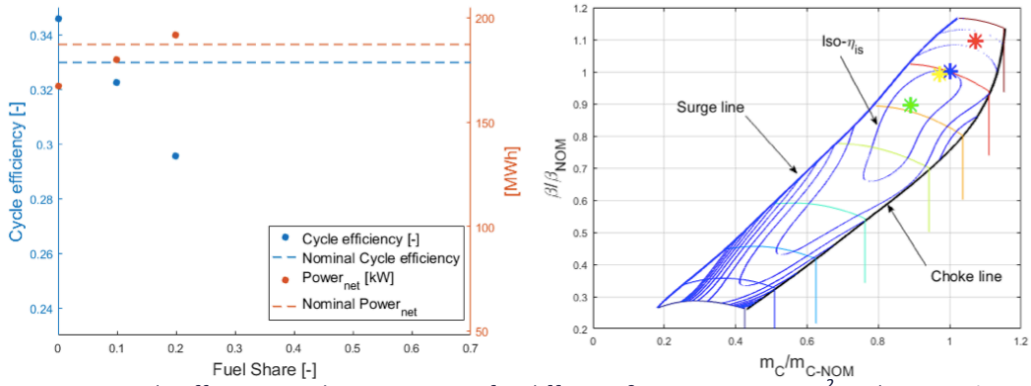

Figure 8.9 Cycle efficiency and Power output for different β_{fuel}, at DNI=650 m^2 and T_{amb}=35°C on the left and compressor map on the right (blue star is the nominal condition, green, yellow and red stars are at relatively at β_{fuel} 10%, 20% and 30%)

Third case is still at 35°C and at an effective DNI of 450 W/m^2. This time, a maximum in the net cycle efficiency trend is observed. When hybridization increases, mass flow rate increases, pressure ratio increases, turbine isentropic efficiency decreases, and compressor isentropic efficiency increases up to a fuel share of 30% and then decreases, approaching the optimal value. The point with same heat entering the system as the design one, gives a 5% lower mass flow rate. Thus, the lowest the effective DNI, the higher the discrepancy at design $Q_{in\text{-}cycle}$ with respect to optimal conditions (thermal losses at the receiver increase).

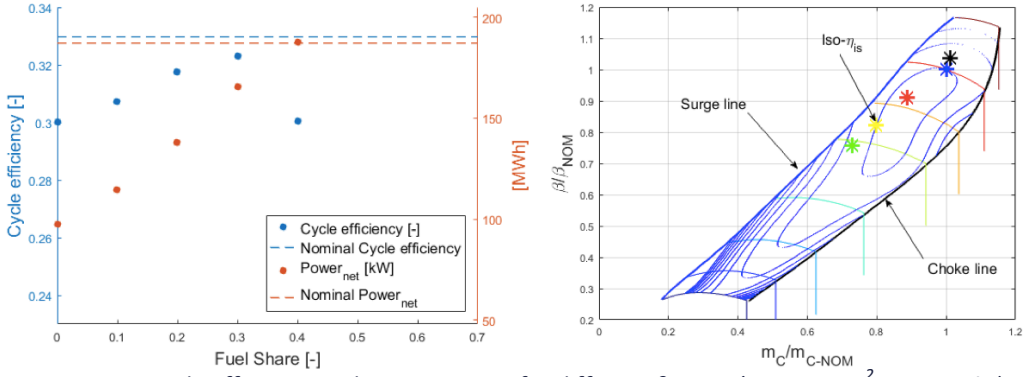

Figure 8.10 Cycle efficiency and Power output for different β_{fuel}, at (DNI=450 m^2; T_{amb}=35°C) on the left and compressor map on the right (blue star is the nominal condition, green, yellow, redand black stars are at relatively β_{fuel} 10%, 20%, 30% and 40%)

Third case is still at 35°C and at an effective DNI of 250 W/m^2. It can be noted that the lower the sun's irradiation, the higher is the β_{fuel} giving the highest cycle efficiency.

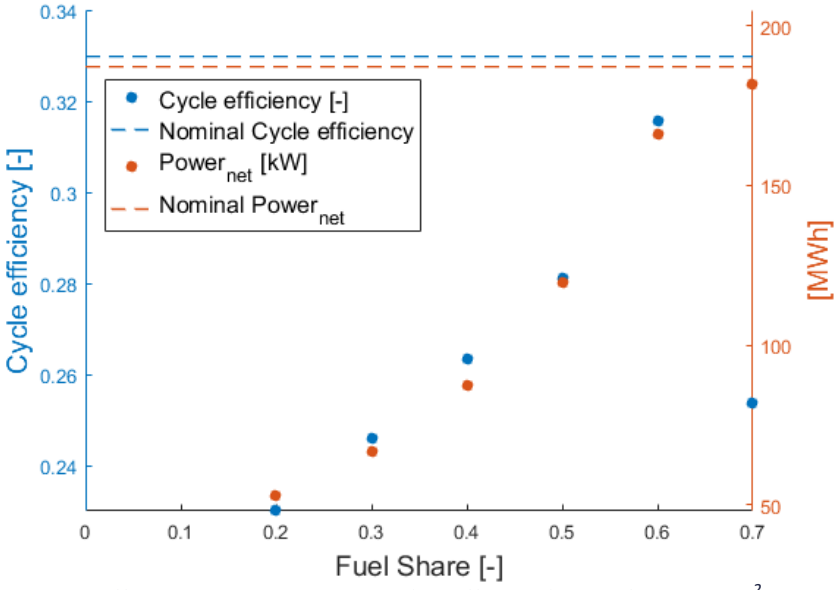

Figure 8.11 Cycle efficiency and Power output for different $\dot{\theta}_{fuel}$, at (DNI=250 m^2; T_{amb}=35°C)

9. Yearly results

Yearly performances are obtained through interpolations among the optimal maps (containing the operating conditions of the system given the DNI and the ambient temperature). As previously explained, for each operating condition and hybridization level, there is one single operating point of the system giving maximum power output (thanks to a changing TIT, thus also a changing shaft speed). Thus, different control strategies need to be investigated to understand the best way to run the plant. A solar-only-mode operating during sun-hours with a by-passed combustor is first considered, followed by a strategy aiming at the nominal power (at the given T_{amb}) with a heavy fuel-integration and by a strategy aiming at the maximum net cycle efficiency.
It is worthy to spend a few words on the Italian law for incentives. In fact, following [58] a power plant can be considered fully renewable with a fossil integration up to 15% calculated on the annual heat entering the system (the heat coming from the combustion of air and fuel can't exceed the 15% of the total heat entering the system). Hence, additional strategies to respect the limit of 15% annual fuel share are implemented.

To compare the different strategies, the following listed parameters are necessary.
The total electric energy output defined as:

$$E_{net} = \sum_{1}^{8760} W_{net} \tag{9.1}$$

The net cycle efficiency defined as:

$$\eta_{cycle} = \frac{\sum_1^{8760} W_{net}}{\sum_1^{8760} Q_{in\_cycle}} \tag{9.2}$$

The annual fuel share defined as:

$$f_{fuel} = \frac{\sum_1^{8760} Q_{in\_fuel}}{\sum_1^{8760} Q_{in\_solar\_field} + Q_{in\_fuel}} \tag{9.3}$$

The solar-to-electric efficiency, when using hybridization defined as:

$$\eta_{sol-el} = \frac{\sum_1^{8760} W_{net} * (1-\alpha)}{\sum_1^{8760} Q_{sun}} \tag{9.4}$$

Equivalent hours are the number of hours per year for which a system has to work at nominal conditions to produce the same amount of energy of the off-design system. They are defined as:

$$H_{eq} = \frac{\sum_1^{8760} W_{net}}{W_{net\_design}} \tag{9.5}$$

9.1 Solar only mode

With this operation strategy, the system works only with solar heat entering the system down to a minimum DNI_{eff} of 200 W/m^2; below this value corresponding to about 25% of the design heat input, the system is shut down. In solar only mode the combustor is by-passed, such as no pressure losses are present.
For each working hour (characterized by a DNI and a T_{amb}), the corresponding system outputs are interpolated from the solar optimal map (Figure 8.5, based on maximum power in each point).
The hourly power profiles of two particular days have been reported in Figure 9.1; May 6th represents one of the most irradiated day of the year 2016 in Sevilla; whereas December 6th represents a typical winter day. The total energy output is significantly different for the two days (1.428 MWh for May 5th and 0.269 MWh for December 5th). From the figures the optical losses, the receiver thermal losses, and the power block losses show in which proportions the initial power coming from the sun is transformed to the net electrical power produced.

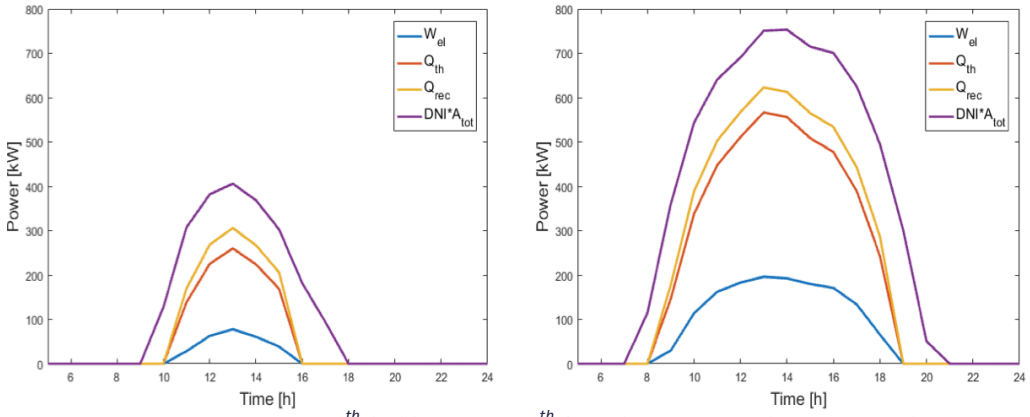

Figure 9.1 December 6th (left) and May 6th (right) hourly specific power profiles

Moreover, in Figure 9.2 the power output (on the left) and the solar-to-electric efficiency (on the right) in function of the power coming from the sun are visible, for three different ambient temperatures.

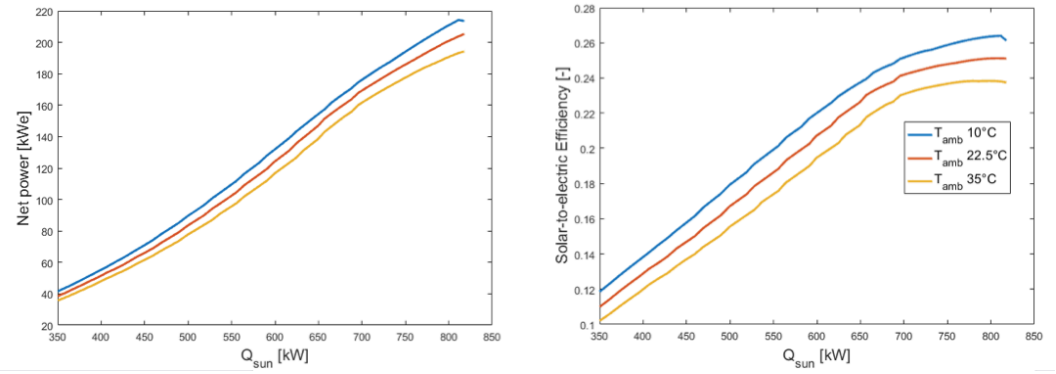

Figure 9.2 Net power output (left) and solar-to-electric efficiency (right) in function of the power from the sun for solar-only mode, for three different ambient temperatures

9.2 Nominal power strategy

With this control strategy, the fuel is fed to the combustor to ensure that the system output is kept at the rated value for each ambient temperature (given by solar-only outputs at the design DNI, and at the considered ambient temperature) during sun hours; for the remaining hours the system is shut down. The cut-off effective DNI is again 200 W/m^2.

For each working hour (characterized by a DNI and a T_{amb}), the corresponding power for each hybridization level is interpolated from the optimal power maps. If the nominal power is reached with these interpolated values: the point is solved. Otherwise, the desired point is in between the maximum-power-point interpolated (corresponding to a *x*% fuel share) and the next null power-point (due to a constraint such as the maximum power allowed, corresponding to a *(x+10)*% fuel share). Hence, the desired fuel share must be found starting from the fuel mass flow rate at the highest power point interpolated, and incrementing it of 0.01 kg/s (until a null point is found again).

This control strategy, characterized by a more regular power output is the one giving the highest annual-fuel-share.

In addition, some considerations must be done regarding the combustor; in hybrid operations, reaching the nominal power when the solar irradiation is high can lead to a temperature rise in the combustion chamber of a few degrees (meaning that the entering compressed air is already at very high temperature). To take into account possible limitations on the combustor operation, a sensitivity analysis is done varying the minimum $\Delta T_{combustor}$ from 0°C to 260°C (*Figure 9.3*). In substance, if the $\Delta T_{combustor}$ required to reach the nominal power is lower than the limiting one, the system switches to solar-only-conditions. In Figure 9.3 the annual energy output, the annual total heat entering the cycle, and the annual heat entering the cycle from the combustor are presented in function of the limiting temperature. It is interesting to notice that the annual cycle

efficiency monotonically decreases for increasing fuel share (thus, lower limiting temperature); this is due to the (previously explained) fact that nominal power conditions don't correspond to a higher cycle efficiency with respect to solar-mode.
The values corresponding to an annual fuel share of 15% are reported and correspond to a minimum temperature $\Delta T_{combustor}$ of 195°C. In Figure 9.4 the trend of the annual fuel share corresponding to each limiting $\Delta T_{combustor}$ is reported.
For $\Delta T_{combustor}$ approaching zero, the various parameters tend to flatten; as it can be seen in Figure 9.5 the number of hours at which the combustor work at low $\Delta T_{combustor}$ is very small (for example only six hours below 20°C), thus influencing less the annual performances. Similar considerations can be done about high $\Delta T_{combustor}$.

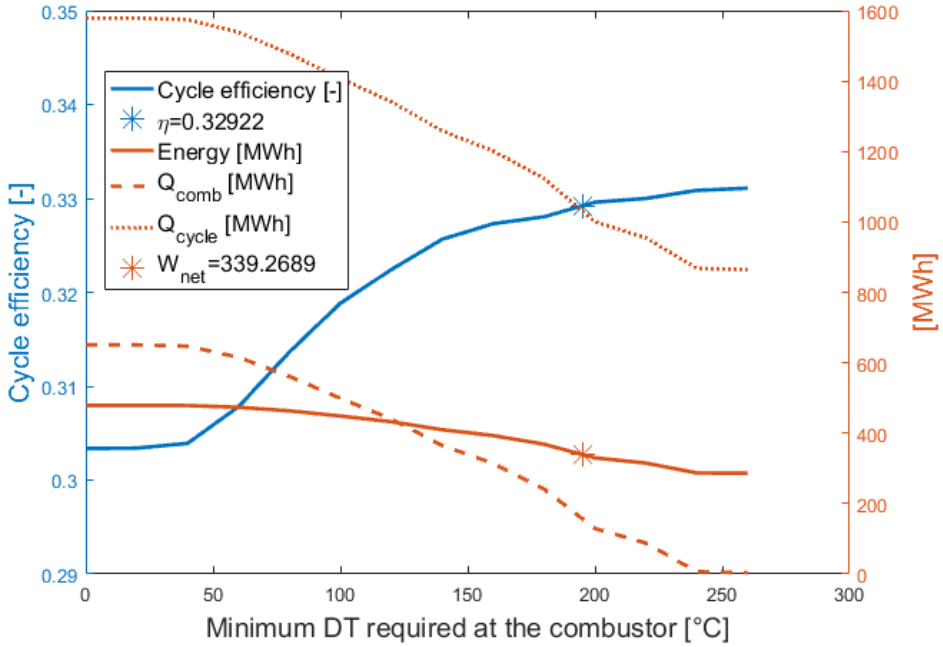

Figure 9.3 Annual results (energy, cycle efficiency and fuel share) for operations with a different limiting ΔT_{comb}

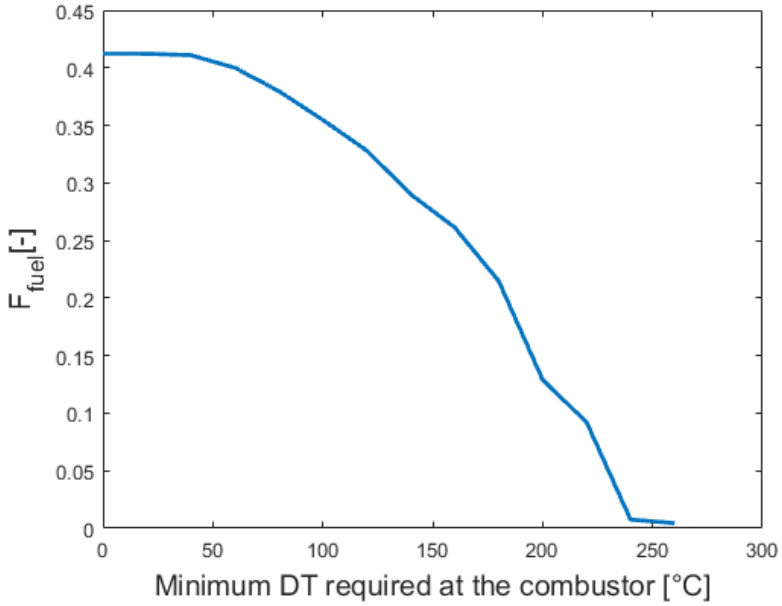

Figure 9.4 Annual fuel share for operations with a different limiting ΔT_{comb}

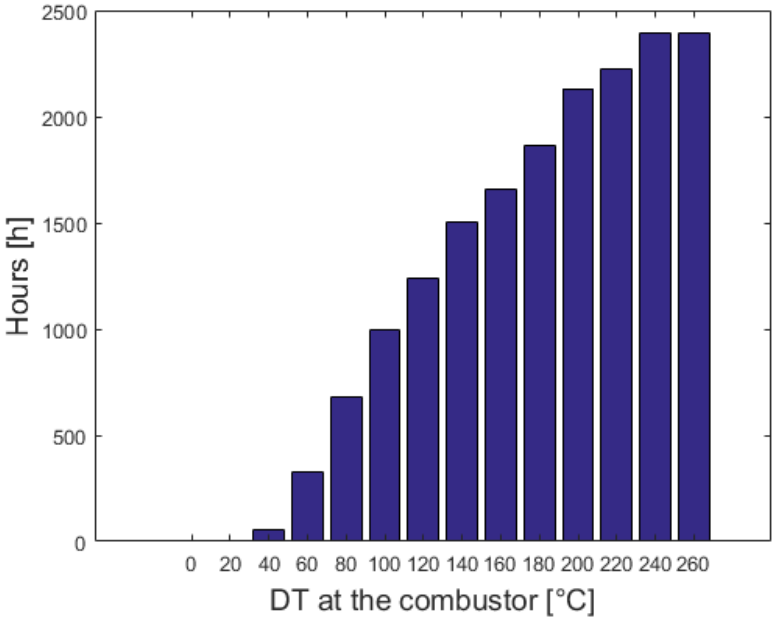

Figure 9.5 Frequence of the various ΔT_{comb} to reach nominal power

9.3 Optimal efficiency strategy

In this strategy, the cycle efficiency is maximized for each hour. The cut-off DNI_{eff} is 200 W/m^2.

For each working hour (characterized by a DNI and a T_{amb}), the corresponding cycle efficiency for each hybridization level is interpolated from the maximum efficiency maps. As it was explained in *Section 8.4*, the cycle efficiency presents a maximum in function of the fuel share (not always corresponding to the maximum fuel integration). Hence, starting from the maximum cycle efficiency point interpolated (corresponding to a *x*% fuel share), the fuel mass flow rate is increased of 0.01 kg/s, and if the resulting net cycle is higher than the previous value, the iteration goes on; if not, starting again from the *x*% fuel share, mass flow rate is decreased of 0.01 kg/s and if the resulting net cycle is higher than the previous value, the iteration goes on. In this process, the maximum cycle efficiency is found hourly.

To take into account the limitations on the combustor temperature, the same procedure of *Section 9.2* has been followed. The results are shown in Figure 9.6 and this time, it is visible how hybridization increases the annual cycle efficiency up to a certain value (as explained in *Section 8.4*, close to the design DNI it is more convenient to work in solar-only-mode to avoid combustor pressure losses). Moreover, for an annual fuel share of 15%, the resulting energy production (347.944 MWh_e) is higher than in the previous case. Thus, working at optimal efficiency is more performing than working at nominal power, and the working hours in hybrid conditions will increase.

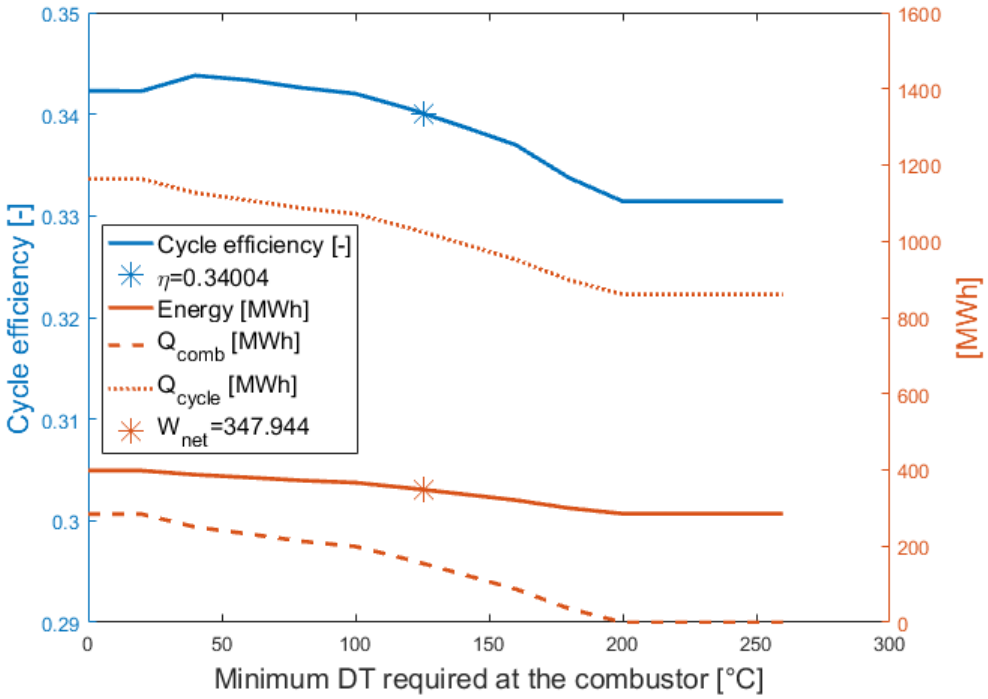

Figure 9.6 Annual results (energy, cycle efficiency and fuel share) for operations with a different limiting ΔT_{comb} based on maximum efficiency

9.4 Hour control strategy

This strategy refers to the limiting annual fuel share of 15%, imposed by the Italian Government in order to access incentive for renewable energy, by controlling each hour the fuel integration.
Since in some cases the optimal output is reachable with a lower fuel share than 15% (for example at high DNI_{eff}), a higher limit can be imposed hourly to reach the desired annual average. This limit is calculated and is equal to 18%. In real applications, last month of the year must be flexible to assure annual target of 15% (so depending on the year, it might be necessary to increase the limit, or to decrease it).

9.5 DNI control strategy

This strategy aims at respecting the annual fuel share to receive the incentives in Italy, by using hybridization according to the effective DNI; it is thus necessary to understand if it is more profitable to use the combustor when the DNI_{eff} is high (close to the design one), when it is low (to act on the smallest power outputs but with more consistent fuel injections required) or when the DNI_{eff} is in its middle range. The following figures (*Figure 9.7*, *Figure 9.8*, and *Figure 9.9*) show the sensitivity analysis on these three cases, highlighting with the stars the working conditions that respect the 15% annual fuel share. These hybridization strategies aim at working at nominal power but same trends are observed if done at optimal efficiency.
As expected the annual energy produced using hybridization from the minimum DNI up to a certain value (to have an annual fuel share of 15%) is more or less equal to the one obtained by limiting the combustor temperatures. This is because these two strategies act on the same working conditions.

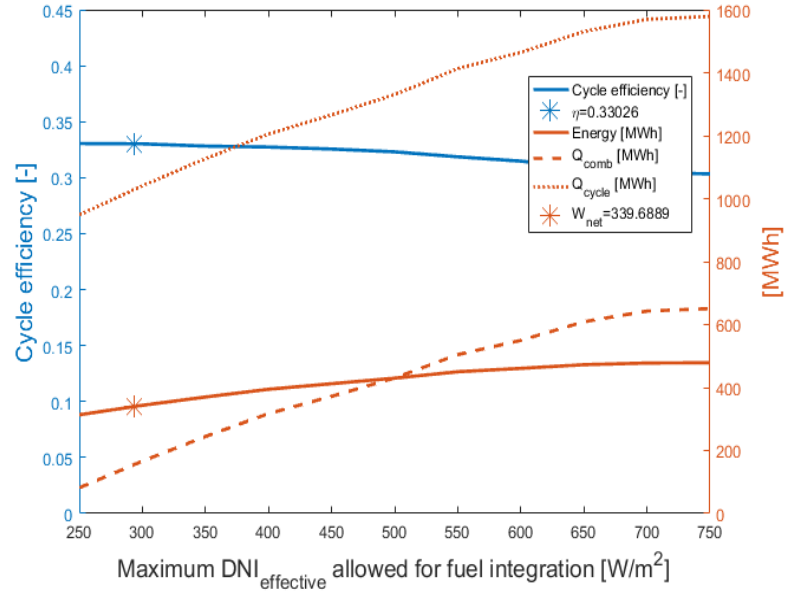

Figure 9.7 Annual results for operations including fuel integration from a 200 W/m^2 DNI_{eff} up to a varying maximum DNI_{eff} (on the abscissa axis)

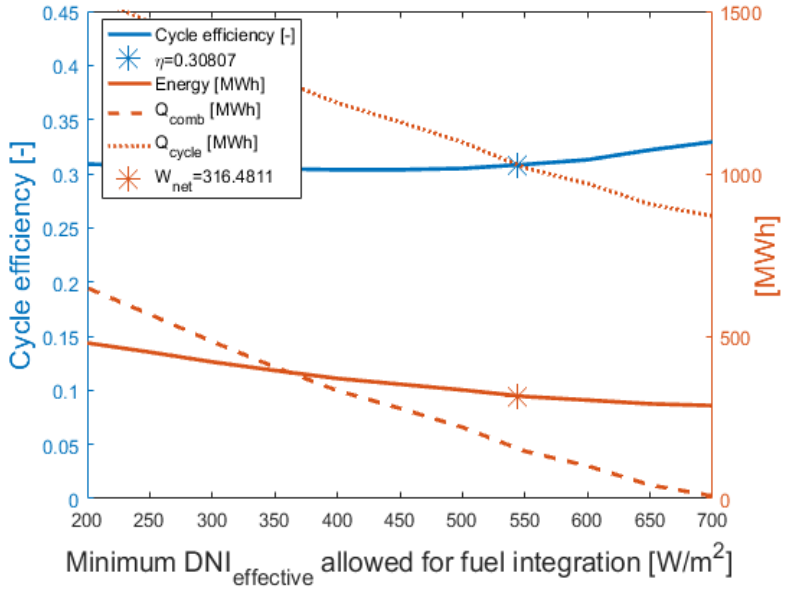

Figure 9.8 Annual results for operations including fuel integration from a varying minimum DNI_{eff} (on the abscissa axis) up to 750 W/m2

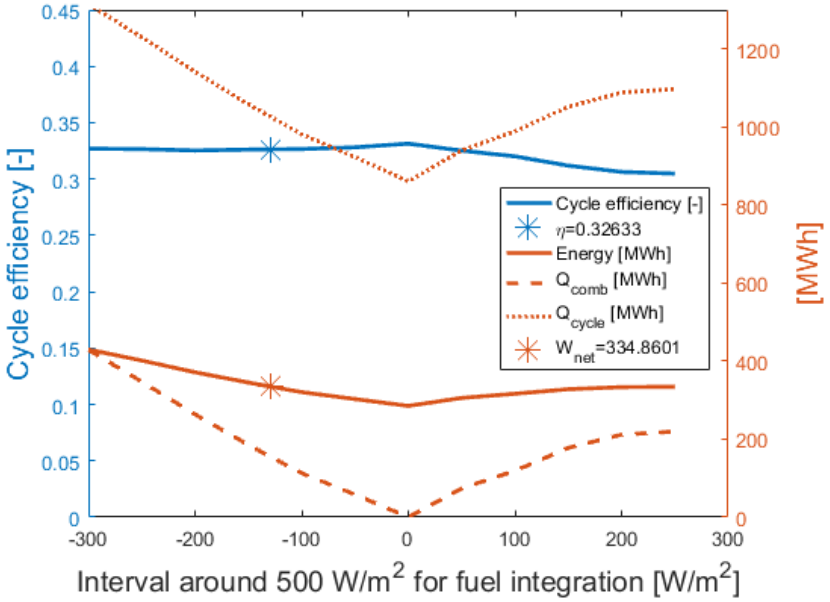

Figure 9.9 Annual results (energy, cycle efficiency and fuel share) for operations including fuel integration around a DNI of 500 W/m2, the highlighted point corresponds to the highest output for a 15% hybridization

For the same annual hybridization, using fuel integration at the lowest DNI leads to a smaller operating interval (93 W/m^2), while using fuel integration at the highest DNI leads to a wider operating interval (206 W/m^2). This is because at higher DNI, the quantity of fuel required to reach nominal power is lower than at low DNI (further from design DNI). Moreover, since it appears that using hybridization when the sun's irradiation is low gives higher outputs, it is interesting to understand if there is also an optimal minimum DNI$_{eff}$. In *Figure 9.10* it emerges that a minimum DNI$_{eff}$ of 200 W/m^2 gives the maximum energy output. In this "best" case, fuel is burned when the DNI$_{eff}$ is the lowest (between 200 W/m^2 and 293 W/m^2), acting on the lowest solar-to-electric-efficiencies (increasing their values) and on the lowest power outputs (*Figure 9.2*) while for the rest of the sun hours the system acts as in solar-only-mode. In Figure 9.11 the interval of hybridization is presented, in function of the minimum DNI$_{eff}$. As for a low DNI, the required fuel to reach nominal power is greater than the one required for a higher DNI, these intervals are expected to increase with their respective minimum DNI. An exception is noticed for hybridization between 450 W/m^2 and 575 W/m^2, where the interval of the combustor operations is lower than the previous one. This can be explained by Figure 9.12, where the DNI distribution in the in Sevilla is reported and appears not homogeneous; highlighting the fact that there are more hours with DNI$_{eff}$ from 500 to 550 W/m^2.

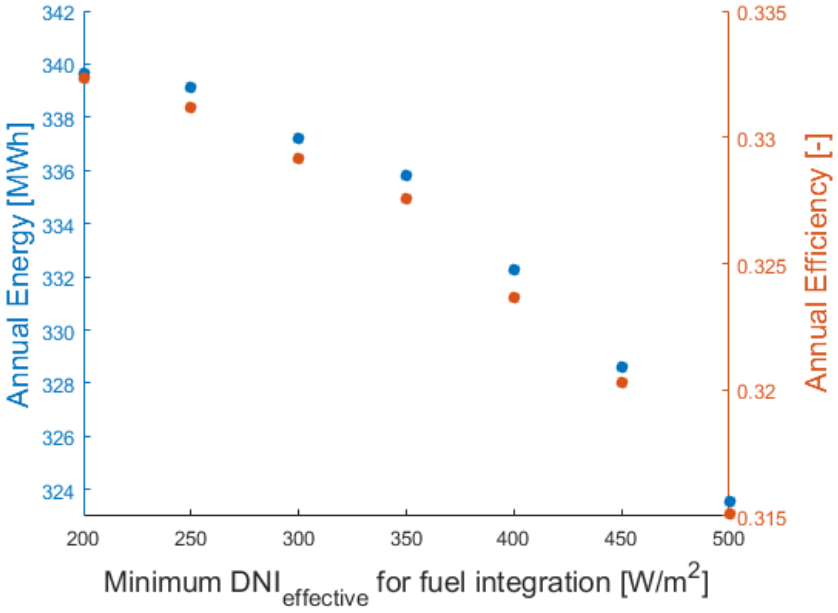

Figure 9.10 Annual results (energy in blue and cycle efficiency in red) for operations including fuel integration from a varying-lower-DNI up to a maximum DNI that produces an annual fuel share of 15%

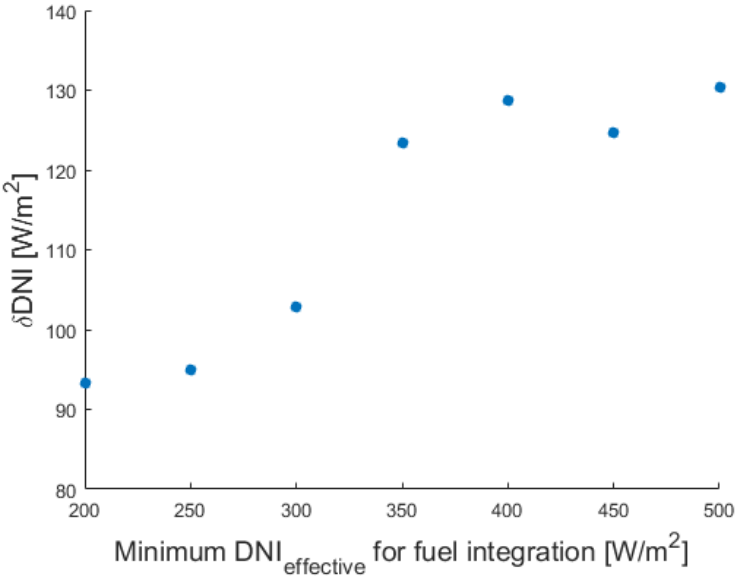

Figure 9.11 Interval of hybridization in function of the minimum DNI at which fuel is burned, producing an annual fuel share of 15%

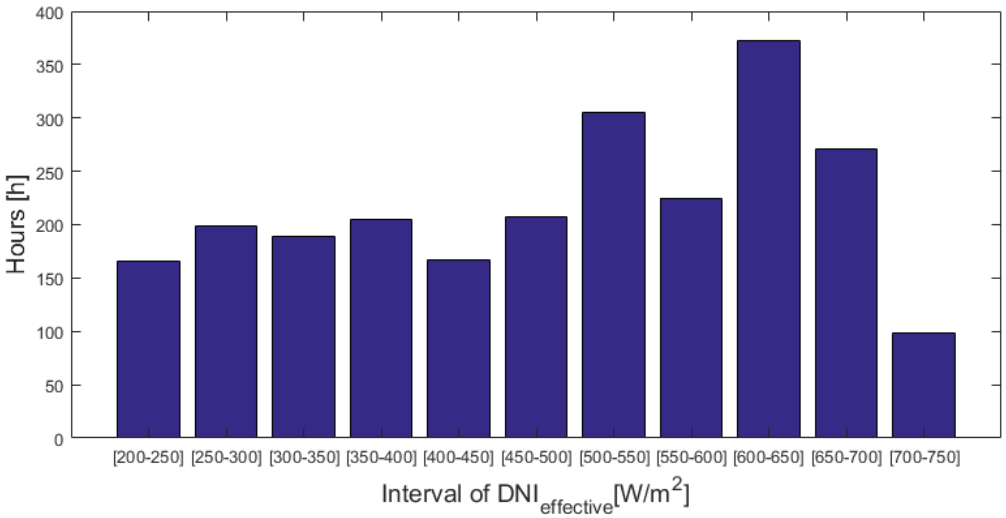

Figure 9.12 Frequence (in hours) of DNI_{eff} in Sevilla

9.6 Results

To compare the previous explained strategies, the main annual results are reported in Table 7.

As expected, the strategy based on the optimal efficiency is the one giving the highest annual-cycle-efficiency, but since the fuel share is almost twice of the one required for incentives, it is not an interesting solution. The reported "*Best strategy*" corresponds to the one with hybridization at low DNI, and gives the second best annual cycle efficiency (both cycle efficiency and solar to electric efficiency).

Table 7 Outputs of the various strategies for a design DNI_{eff} of 750 W/m2

Strategy	***Energy [MWh]***	η_{cycle} ***[-]***	η_{sol-el} ***[-]***	f_{fuel} ***[-]***	H_{eq} ***[h]***
Optimal efficiency	398,22	0,3423	0,2325	0,2443	2127
Best strategy	339,04	0,3318	0,2239	0,1500	1811
Solar only	285,29	0,3314	0,2189	-	1524
Hour control	333,86	0,3141	0,2176	0,1500	1783
Nominal power	479,01	0,3088	0,2141	0,4181	2558

Additional information such as annual optical efficiency and receiver thermal efficiency are not reported in Table 7. However it can be said that for all the strategies annual optical efficiency is always equal to 0.7202 since

the plant switches on and off for the same interval of DNI, while the thermal efficiency is lower for the Solar-Only-Mode (0.8104), higher for the Nominal Power (0.8427), and in-between for the Optimal Efficiency (0.8276) and for the Best Strategy (0.8176). This can be explained by the fact that in Solar Only mode the receiver outlet temperature of air is the TIT (no matter the DNI) and these conditions of high temperature and low radiation lead to low thermal efficiencies (Figure 6.9); while in the Nominal Power mode, for low DNI the receiver outlet temperature is lower (due to the presence of the combustor), leading to higher thermal efficiencies.

Finally, power output of the different strategies are reported in *Figure 9.13*, on the left for the design ambient temperature with respect to the actual DNI, and on the right in a 3 dimensions plots with respect to both the ambient temperature and the DNI. Some fluctuations are visible in the Nominal Power and in the Optimal Efficiency strategies; this is due to the discretization of the maps presented in *Section 8.3*.
For a given temperature, some disturbances are observed, due to the tolerance of the model. In fact, two hours are required to obtain a single strategy output, and a more accurate analysis would lead to longer computational times.

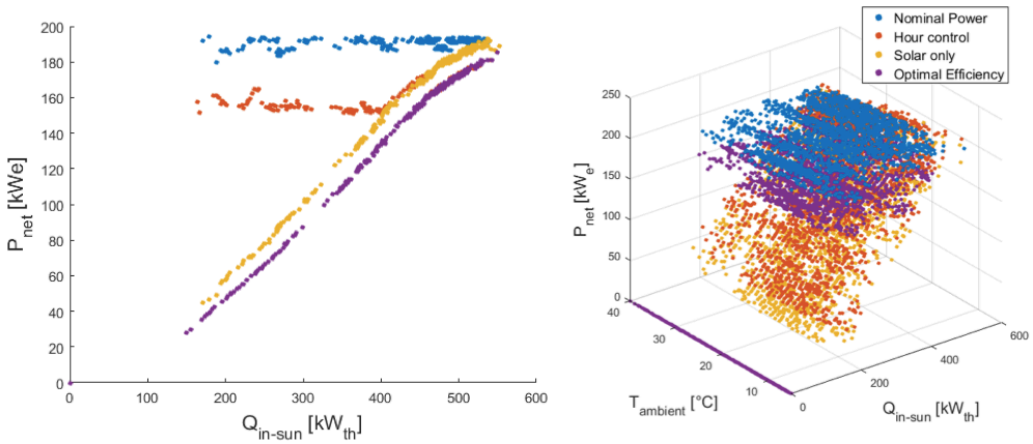

Figure 9.13 Net power ouput at 35°C (left) over actual DNI and in a 3D plot (right)

9.7 Carbon dioxide emissions

The annual CO_2 emissions are an important environmental performance indicator and can be calculated based on the mass of fuel burnt annually and on its carbon content.
Depending on the strategy adopted the power output and the amount of fuel used changes. Thus, three cases will be considered to calculate the avoided CO_2 emissions with respect to a standard gas turbine: the solar-only mode, the nominal power strategy and the best strategy.

The standard micro-gas turbine used for comparisons is the one designed at an ambient temperature equal to the mean of the ones occurring when using the solar-only-mode, which is 24.5°C (lower than the design 35°C). Although in this case, the combustor is constantly used. The resulting carbon dioxide emissions are equal to 573 kg/MWh_{el}.
Hence, during the solar-only operations 573 kg/MWh_{el} of CO_2 are avoided, while by using the "Nominal power" strategy the saving is of 312 kg/MWh_{el}, with the "Optimal efficiency" 430 kg/MWh_{el}, with the "Hour control" 433 kg/MWh_{el}, and with the "Best" strategy the saving is of 484 kg/MWh_{el}. As expected the "Nominal power" strategy is the one that reduces less the CO_2 emissions since it has the highest annual fuel share, while the "Best solution" is the most green one, abating the highest CO_2/MWh_{el}. For the five strategies, the total carbon dioxide emissions per year are reported in *Figure 9.14*.

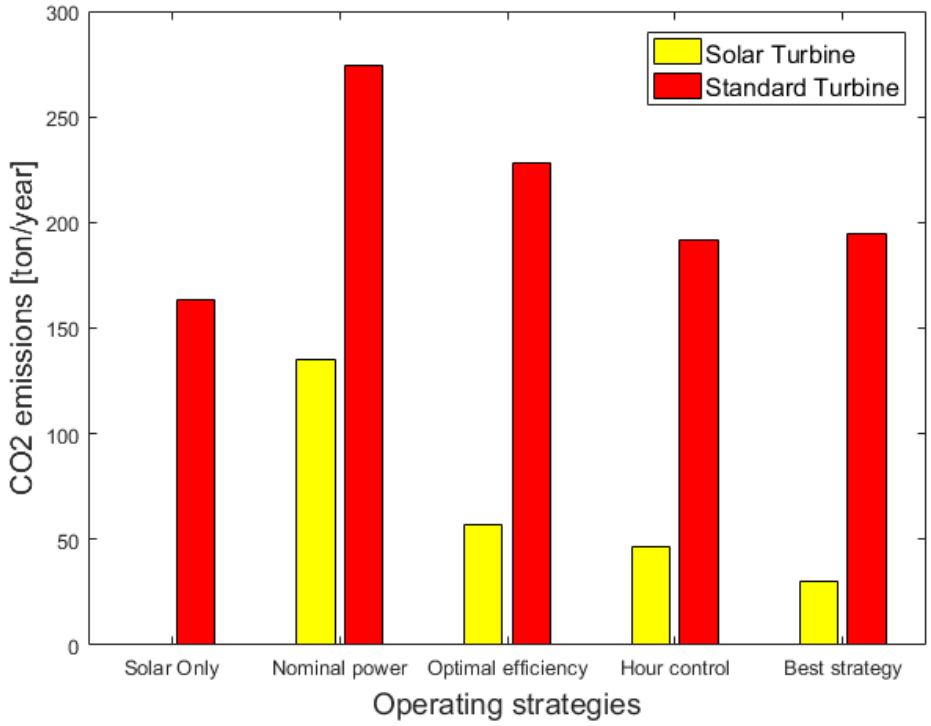

Figure 9.14 Annual CO2 emissions for the different strategies by using a Standard Turbine and a Solar Turbine

10. Economic Analysis

This section aims at giving an economical evaluation of the studied system through the assessment of Levelized Cost of Electricity (LCOE) that is recognized as an easily understandable and comprehensive parameter to measure the competitiveness of different energy generation technologies where the cost of electricity generated is the key metric used.
The LCOE represents the equivalent cost of each unit of electricity generated during the lifetime of the project taking into account the initial investment cost (CAPEX), operations and maintenance cost (OPEX) and financing costs associated with interest on any borrowings. It represents the real cost of producing electricity. The formula used for calculating the LCOE is:

$$LCOE = \frac{CAPEX + \sum_{t=1}^{n} \frac{OPEX_t}{(1+r)^t}}{\sum_{t=1}^{n} \frac{E_t}{(1+r)^t}} = \frac{NPV_{lifetime\ cost}}{NPV_{energy\ ouptut}} \quad (10.1)$$

Where: CAPEX is the initial investment, OPEX is the O&M costs in year t, n is the lifetime of the project in years is, E_t is the electricity generated in year t, and r is the discount rate (often referred as the Weighted Average Cost of Capital).

$$r = c_{debt} \cdot \frac{D}{T} + c_{equity} \cdot \frac{E}{T} \quad (10.2)$$

Where c_{equity} is the cost of equity, c_{debt} is the cost of debt, E is the market value of the firm's equity, D is the market value of the firm's debt and T is the total market value of the firm's financing (equity and debt).

Lifetime of Solar Tower is more than 30 years as suggested by the IRENA [59], but a value of 25 years was used in accordance to the Italian law regarding the renewable incentives.

When evaluating prospective energy projects [60], some assumptions are made to evaluate easily the LCOE: annual output of the project and cost of production per unit of output are constant each year.

$$LCOE = \frac{C_{inv} \,.\, FCR}{E_{el}} + \frac{O\&M}{E_{el}} \quad (10.3)$$

Where the Fixed Charge Rate (FCR) is used, defined as:

$$FCR = \frac{r.(1+r)^n}{(1+r)^n - 1} \tag{10.4}$$

The simplified equation is the one used for our analysis. It is important to notice how the discount rate strongly influences the LCOE, so the LCOE is both calculated for a 5% and a 10% discount rate.

10.1 CAPEX

A key input when assessing economic performance constitutes the initial investment required by the developer of the project. However, it is difficult to find reliable cost data. Nevertheless, industry validation of the cost data allowed accurate and up-to-date cost data to be collated. The investment cost can be divided in two main expenses: the Power Block and the Solar Block.

10.1.1 Power Block purchasing cost

As regards thermal engine, information derived from stationary MGT sector are recognized reliable to be used in the studied system; in particular, it is reasonable to expect that no particular cost issues are introduced by the placement of the thermal engine at the top of the tower.
The power block section is composed by standard components: compressor, recuperator, combustion chamber, uncooled expander and generator. Regarding the MGT, informations are now considered reliable due to the diffused technology. Specific cost correlations are taken from [61] and costs are adapted with [62]. The coefficients used in these equations are reported in Table 8.

$$C_{compressor} = \sqrt{\frac{R_g}{R_{ref}}} * c_1 * \frac{m_{air}}{c_2 - \eta_{pol_c}} * \beta_c \tag{10.5}$$

$$C_{expander} = \sqrt{\frac{R_g}{R_{ref}}} * t_1 * \frac{m_{tot}}{t_2 - \eta_{pol_t}} * \beta_t \tag{10.6}$$

$$C_{combustor} = \frac{cc_1 * m_{tot}}{cc_2 - \frac{p_{out}}{p_{in}}} \tag{10.7}$$

$$C_{recuperator} = 1.5 * \left(r_1 * m_{air} * {p_{in_{cold}}}^{-0.5} * \Delta p^{-0.5} * \frac{\varepsilon}{1-\varepsilon}\right) * f \tag{10.8}$$

$$C_{generator} = g_1 * {P_{el}}^{g2} \quad (10.9)$$

Where the Δp in the recuperator's cost represents the sum of the Δp on the cold side and on the hot side.

Table 8 Coefficients of the gas turbine cost function, taken from [61]

c1 (€)	55.8	**t2 (€)**	0.903
c2 (€)	0.942	**g1 (€)**	18.7
cc1 (€)	36.1	**g2 (€)**	0.95
cc2 (€)	0.995	**r1 (€)**	625.1
t1 (€)	376.1	**f**	1.0

The final purchasing cost has been multiplied by 1.56 to account the costs of installation, electrical equipment and control instrumentation.

10.1.2 Heliostats field and Tower cost

The cost functions for the solar equipment are subject to a much higher degree of uncertainty than the other, more standard power plant equipment costs, as a large number of the components are still at the prototype stage. It is to be expected that with further developments and mass production the cost of the solar components will drop rapidly [27].
The cost functions for the heliostat field are based on the work of [27]. The total cost of the heliostat field can be broken down into the cost of the heliostat mirror units themselves and the land purchasing costs:

$$C_{field} = C_{land} + C_{heliostats} \quad (10.10)$$

Where:

$$C_{heliostats} = c_{heliostats} * A_{hel} * N_{hel} \quad (10.11)$$

$$C_{land} = c_{land} * (1.3\ A_{land}) \quad (10.12)$$

Heliostats mirrors cost used is 170 euro/m^2 representing an average value for current production levels (for glass/metal heliostats) given by SAM software [63]. This value is a trade-off between cost and optical performances, today's technologies as suggested by [64] and [65] can even reach cost of heliostats of 130 euro/m^2 but corresponding to bigger heliostats (45 m^2

each). The heliostat cost is the most capital intensive one. Land costs strongly depends on the location; anyways a value of 1.5 euro/m^2 is used for the model. The fixed area increase in the land cost function takes into account the requirements for roads and additional land surrounding the power block.

Towers are constructed of steel or reinforced concrete Figure 10.1.

Figure 10.1 Steel tower (left) and reinforced concrete tower (right)

The cost of the tower is based on a gas turbine cost analysis [27] (and not a micro-turbine), which showed that below a height of 120 m a metal tower is less expensive (whereas above this height a reinforced concrete tower should be considered). The cost of the central receiver tower can be calculated based on its height and for a height lower than 120 meters, equation (10.13*)* can be used (showing the cost in USD, thus requiring the conversion into euro); even if no difference is considered based on the metal composition used, and no information are given on the minimum height of the tower for which this equation is correct.

$$C_{tower} = 1.090 * 10^6 * e^{(0.0088 * h_{tower})} \quad (10.13)$$

Equation (10.13*)* gives an investment cost of 1.5 thousand euros. Which is a meaningful value for higher power output solar tower (in the MW_e range); but not in this context. In fact, the higher the power output, and the strongest the tower structure is.

The solar receiver is the component of the hybrid solar gas-turbine power plant that is subject to the largest degree of uncertainty concerning the purchasing cost. To date, each receiver design has been essentially a prototype and only limited experience exists with the manufacture of high-temperature receivers for gas-turbine systems.
The cost of the receiver is found in System Advisor Model (SAM) cost database (in USD):

$$C_{receiver} = 200 * Q_{in\_receiver} \quad (10.14)$$

To calibrate the capital cost function, some documents about AORA field were used ([66] and [67]), stating that the total system costs 550 thousand euros (not including land acquisition). So, being the tower the only unknown cost, it can be deduced from the other costs (it is important to notice that the Power Block of the Aora field has a different investment cost since the generator is design on a peak power of 100 kW_e):

$$C_{tower\_receiver} = (C_{total\_Aora} - C_{PB\_Aora} - C_{heliostats} - C_{receiver}) \quad (10.15)$$

Finally, an additional 10% of investment cost is added to consider other expenses such as wiring.

10.1.3 Results

After having applied all the costs definitions to this project outputs, the investment costs of the various components are resumed in Table 9, and an additional pie diagram is illustrated in Figure 10.2.

Table 9 Investment cost of the studied tower system

Component	Investment cost	Specific cost	Relative cost
	[euro]	[euro/kW_e]	[%]
Compressor	3 030	16,18	0,6
Expander	26 270	140,31	5,0
Recuperator	29 265	156,31	5,6
Generator	2 695	14,39	0,5
Combustor	3 583	19,14	0,7
TOT Power Block	64 843	346,33	12,4
Heliostats	141 440	755,43	27,1
Land	12 675	67,70	2,4
Tower	178 720	954,55	34,2
Receiver	124 800	666,56	23,9
TOT Solar Block	457 635	2444,24	87,6
TOT System	522 478	2790,57	100,0

It is worth to notice how the impact of the solar field and receiver on the investment cost is predominant (82.09%) compared with the power block one (17.91%).

Recuperator accounts for 45.07% of the thermal engine cost, nevertheless a reduction cost would be attainable thanks to an effectiveness reduction, which would involve a cycle efficiency penalty, thus a negative effect on the LCOE.

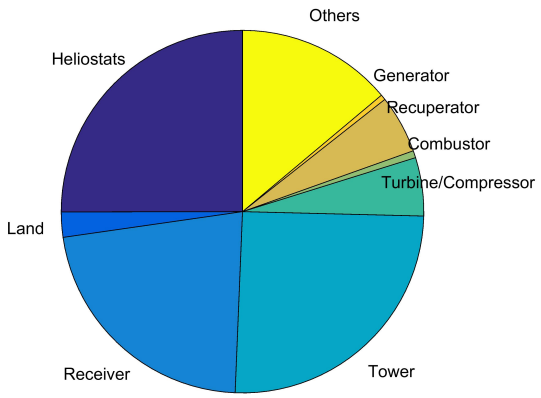

Figure 10.2 Proportion of capital investment costs

10.2 OPEX

Since the operation of a solar tower plant relies mostly on free solar irradiance as the energy source, the running costs are notably reduced when compared with conventional fossil fuel power generation. As a result, the OPEX of a solar tower plant is very small compared with the initial investment, although it still remains significant.
Larger plants (producing powers in the MW scale) have to consider labor costs such as plant manager, administration, security, maintenance and operations (supervisor and technicians), mirror cleaning… but since this plant has only 52 heliostats and a power block we can neglect it.
The operations and maintenance cost (that also include insurance cost) is considered to be 5% of the capital cost (for each year) plus the fuel cost (which depends on the strategy adopted).

$$C_{O\&M} = 0.05 * C_{CAPEX} \tag{10.16}$$

$$C_{fuel} = c_{fuel} * \sum_{1}^{8760} V_{fuel} \quad (10.17)$$

$$C_{OPEX} = C_{O\&M} + C_{fuel} \quad (10.18)$$

Natural gas price [euro/Sm^3] for industrial applications has been converted from the value from *BP review* [68], given as 6.5 euro/MMBtu.

Notice that in the report [69], a mean operations expenses of 0.017 euro/kW_eh is calculated based on the existing solar plants; which is approximately half of what is considered in this case. This is because the existing plants are (almost all) of much larger sizes (MW).

10.3 Profitability

A sensitivity analysis has been done on the LCOE, based on the Weighted Average Cost of Capital (average after-tax cost of a company's various capital sources). In fact, the LCOE of the various strategies is strongly influenced by the WACC, and this value can't be predefined. The most common interval of WACC has been used (between 5% and 10%).

Finally, the Net Present Value (value of a project reported to the actual day), the Internal Rate of Return (discount rate for which the NPV is null) and the Pay-Back Time (time required to earn back the initial investment costs) have also been calculated in order to analyse the profitability of this project. For these parameters, tariff of electricity is required.
Incentives applicable for CSP technologies in Italy belong to the "Tariffa onnicomprensiva" mechanism. In this case (because it depends on the annual energy output) a minimum tariff (324 euro/MWh in 2016) is guaranteed, and a premium (45 euro/MWh in 2016) is also obtained for respecting the annual fuel share of renewable technologies (tariffs taken from [22]).

As it can be seen in Table 10 and in

Table 11, which are the results corresponding to two plausible different discount rates, thus two different FCR from (*10.4*), the best strategy from the LCOE point of view is the "Optimal Power" one, but since the tariff given by the PUN is much lower than this LCOE, the NPV would be negative. The best strategy presents the second lowest LCOE (lower than the Tariffa Omnicomprensiva for both discount rates), the lowest PBT, the highest margin, and the highest IRR. This latter index, is the rate of growth that a project is expected to generate.

Table 10 NPV, PBT, IRR for each strategy, for 5% discount rate (best scenario)

Strategy	LCOE [euro/kWh]	PBT [year]	NPV [keuro]	IRR
Solar only	0,2396	7	653,490	0,151
Nominal power	0,1548	3	1509,700	0,272
Best strategy	0,2064	5	905,490	0,185

Table 11 NPV, PBT for each strategy, for 10% discount rate (worst scenario)

Strategy	LCOE [euro/kWh]	PBT [year]	NPV [keuro]
Solar only	0,3173	9	228,340
Nominal power	0,2011	4	785,860
Best strategy	0,2717	6	392,430

10.4 No incentives strategy

Renewable energy production is more costly than energy produced by fossil fueled power plants, thus it needs subsidies. However, as it happened with photovoltaics, once a technology is well-known, incentives usually drop. Hence, a scenario following the hourly price of energy of the Italian market (and no more a fixed tariff given by the "*Tariffa Omnicomprensiva")* is interesting from a long-term perspective point of view. In this future scenario it is important to understand if hybridization is economically sustainable for the considered CSP technology or not.

The capital investment cost related to the solar field is expected to decrease, hence as a first assumption it is divided by two with respect to the current cost, and then divided by three (as it could optimistically happen by the time that incentives stop). NB: the capital cost associated with the power block is fixed as it is considered a consolidated technology.

Since the hourly price of energy "*Prezzo Orario*" depends on the region of the country, the "*Prezzo Unico Nazionale*" (PUN) announced on the Day-Before Market is used, being an average of the zones for a single day (*Figure 10.3* taken from [70]). Moreover since the PUN changes everyday, a single day of the year is considered for this analysis, chosen to be January 25 of 2017.

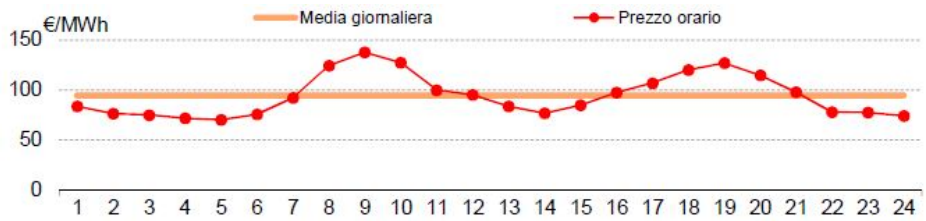

Figure 10.3 PUN of January 25 of 2017, from GME report

It is important to notice how the PUN chosen (100 euro/MWh) seems high, compared to the 2016 annual average value (42.78 euro/MWh [71]), but it is representative of the month of January 2017 (due to the consequences of France nuclear power plants shut down).
LCOE and CO_2 emissions of this "No incentives" strategy are reported in *Figure 10.4*, for two possible investment costs of the solar block (divided by 2 or 3 with respect to today's values). The results show how an increase of the fuel share of the system leads to more convenient LCOE, but to dramatic increase of the CO_2 emissions (going against the renewable goal of this plant). Their respective NPV aren't plot, but it is important to state that they remain negative for any LCOE, highlighting the fact that this technology is not economically sustainable without incentives. Moreover these results are strongly dependent on the PUN chosen. In facts, from [72] it is visible how the tariff changes based on the month of the year (higher during winter and summer) and on the region (higher in the northern regions).

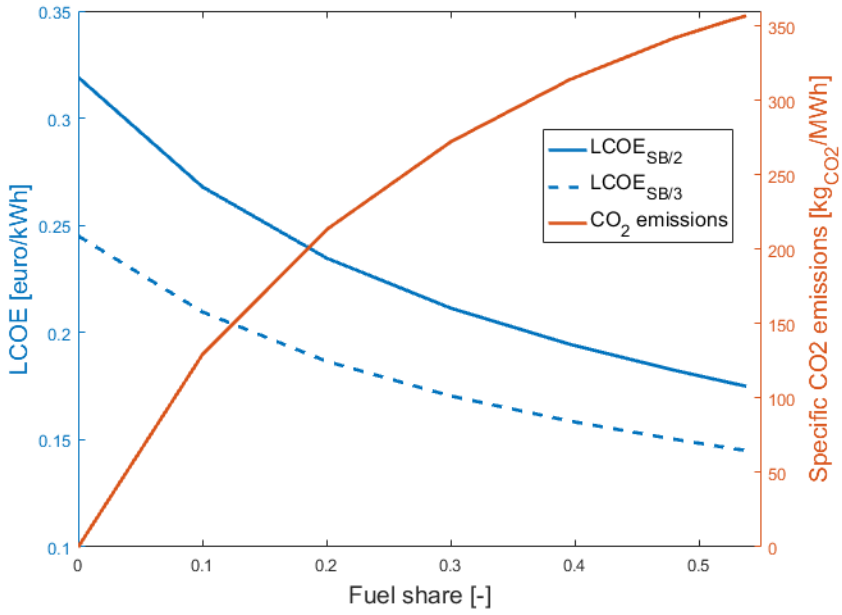

Figure 10.4 LCOE and specific CO2 emissions as function of hybridization level

11. Conclusions

In these years we are assisting at the strongest acceleration of climate change brought on by the increasing emissions of industry-induced global warming gases. Hence, today's biggest challenge is to find new ways to produce renewable energy.
This thesis project has investigated a technology currently still at research level: a micro-gas turbine (design net power output of 187.25 kW_{el}) coupled with a CSP tower system and a fossil fuel backup.

After the definition of the 52 heliostats field (corresponding to a 832 m^2 reflective area), which coordinates were taken from an existing plant situated in Almeria (Spain), the optical model of the field and the receiver was implemented using SolTrace software. To increase the concentration ratio of the field, a secondary receiver design was optimized, based on the annual optical performances of the various geometries. The resulting compound parabolic concentrator has a 35° semi-acceptance angle and a final concentration ratio of 1883, while the optimal annual optical efficiency weighted on the corresponding DNI, is 0.7202.
The power block was designed on the basis of a model previously developed in Politecnico di Milano, upgraded following the most recent publications on the topic, and extended by adding a combustor for hybridization.
Technical constraints such as the power output (limits at part loads), stall and choke limits at the compressor, blocking limit at the turbine and maximum recuperator's temperature were accounted to perform the system on-design and off-design performances, for each level of fuel-integration.
The on-design conditions, characterized by a DNI of 950 W/m^2, an optical efficiency of the solar field of 79%, solar only operations and a 950°C TIT, lead to a receiver efficiency of 90.96%, a power block efficiency of 32.99% and a net power output of 187.25 kW_e.

Following a discussion about the power plant running characteristics, different operating strategies were defined. The most environmentally interesting strategy is the Solar-Only-Mode producing 285.29 MWh_e, at the annual solar-to-electric efficiency of 0.2189.
Referring to the GSE in Italy, a power plant can access renewable incentives while using an annual fuel-integration up to 15%; thus, a strategy was modeled expressly in order to increase the system output and receive the relative fixed tariff (higher than the variable price-market). The analysis demonstrated that using fuel-integration at the lowest irradiations, increased the system cycle efficiency (and receiver thermal efficiency). The annual energy produced with this 15% limitation was 339.0 MWh_e while the annual solar-to-electric efficiency was 0.2239.

Additionally, a strategy bringing to a strong increase of carbon dioxide emissions but aiming at producing the nominal power for each T_{amb} was defined, leading to the highest energy output (479.0 MWh_e), the highest fossil fuel share (0.4181) and the lowest solar-to-electric efficiency (0.2141). This latter case highlighted that it is not more efficient to work annually at nominal power; thus a strategy aiming at working at maximum net cycle efficiency each hour was also implemented. The resulting energy output (398.22 MWh_e) is lower, such as the fuel integration (0.2443) while the annual cycle efficiency 0.3423 is higher, showing how it might be more convenient to work at a lower hybridization level to have a higher efficiency. CO_2 emissions-savings with respect to a standard gas turbine were also highlighted for all the strategies adopted.

Since the main challenge of CSP technologies is their cost, an economic analysis was then performed based on the reliable power-block costs (346.33 euro/kW_e), and on the more uncertain solar-block costs (2444.24 euro/kW_e). A best scenario characterized by a lower discount rate (5%) gives a LCOE of 0.2064 euro/kW_eh for the best renewable strategy, and a worst scenario with a higher discount rate (10%) gives a LCOE of 0.2717 euro/kW_eh. Both these values are higher than the market hourly price of electricity, but much lower than the fixed tariff guaranteed for renewable CSP in Italy; hence this technology is convenient today, implemented with the actual incentives. Other economic parameters such as Net Present Value, Pay Back Time and Internal Rate of Return are calculated to evaluate the profitability of the project. The best renewable strategy in the best discount rate scenario, features a 5 years PBT, a 905 500 euro NPV and an IRR of 0.185; thus classified as a rewarding project.

Finally a last case assuming that no incentive is available, thus using the hourly profile of the energy tariff of a single day (PUN of January 26 2017) is considered. The results show that the lowest LCOE corresponds to the highest fuel share case (highlighting the convenience of natural gas price) and to a negative NPV. Thus with these plant parameters and no incentive, this power plant wouldn't be profitable.

Future developments

On the power block side the integration of a bottom ORC cycle could be studied, in order to increase the output of the plant. In facts, the temperature outside the recuperator is still high during operations (281°C in on-design conditions as a reference).

On the solar field, the possibility of storing the heat in parallel of the power block could be implemented, to increase the flexibility of the plant, allowing to work outside the sun-hours.

Moreover, a more accurate model of the volumetric receiver could be written; many papers are published today ([73], [74], [30], [75]), but none of them have theoretical results matching the practical ones.

Bibliography

[1] Kristin Seyboth *et al.*, *Renewables 2016 Global Status Report*. 2016.

[2] A. Morales, "https://www.bloomberg.com/news/articles/," 2015. [Online]. Available: https://www.bloomberg.com/news/articles/2015-12-03/the-100-billion-dollar-question-hanging-over-un-climate-talks.

[3] "Power from the Sun BOOK, chapter 8." [Online]. Available: http://www.powerfromthesun.net/Book/chapter08/chapter08.html.

[4] A. Fernández-García, M. E. Cantos-Soto, M. Röger, C. Wieckert, C. Hutter, and L. Martínez-Arcos, "Durability of solar reflector materials for secondary concentrators used in CSP systems," *Sol. Energy Mater. Sol. Cells*, vol. 130, pp. 51–63, 2014.

[5] L. S. Mendoza Castellanos, G. E. Carrillo Caballero, V. R. Melian Cobas, E. E. Silva Lora, and A. M. Martinez Reyes, "Mathematical modeling of the geometrical sizing and thermal performance of a Dish/Stirling system for power generation," *Renew. Energy*, vol. 107, pp. 23–35, 2017.

[6] R. Larson and R. Emmett West, "Implementing of Solar Thermal Technology," The MIT Press, 1996.

[7] J. Barbee, "Could this be the world's most efficienct solar electricity system?," *Guard.*, 2015.

[8] "Xah Arts." [Online]. Available: http://xaharts.org/Whirlwheel_dir/reflecting_disks/reflecting_disks.html.

[9] "Wikipedia." .

[10] "No Title." [Online]. Available: http://www.puertoerrado2.com/.

[11] "No Title." [Online]. Available: http://www.abengoasolar.com/web/en/acerca_de_nosotros/sala_de_prensa/noticias/2016/.

[12] "CSP worl map," 2016. [Online]. Available: http://www.solarpaces.org/.

[13] "CSP world map," 2017. [Online]. Available: http://cspworld.org/cspworldmap.

[14] "Solar thermal power plants article." [Online]. Available: http://www.volker-quaschning.de/articles/fundamentals2/index.php.

[15] "ETH Zurich University." [Online]. Available: http://www.prec.ethz.ch/research/solar-power/solargasturbine.html.

[16] X. Py, Y. Azoumah, and R. Olives, "Concentrated solar power: Current technologies, major innovative issues and applicability to West African countries," *Renew. Sustain. Energy Rev.*, vol. 18, pp. 306–315, 2013.

[17] H. J. Lee, J. K. Kim, S. N. Lee, and Y. H. Kang, "Numerical study on optical performances of the first central-receiver solar thermal power plant in Korea," *J. Mech. Sci. Technol.*, 2016.

[18] D. Hopwood, "Abu Dhabi's Masdar plan takes shape," *Renew. Energy Focus*, vol. 11, no. 1, pp. 18–23, 2010.

[19] S. Ekkad, S. Dutta, and J.-C. Han, *Gas Turbine Heat Transfer and Cooling Technology*, Second Edi. 2000.

[20] “Google Earth.” [Online]. Available: https://www.google.com/earth/.
[21] A. Giostri and E. Macchi, “An advanced solution to boost sun-to-electricity efficiency of parabolic dish,” pp. 1–32, 2014.
[22] Gse, “Incentivazione della produzione di energia elettrica da impianti a fonti rinnovabili diversi dai fotovoltaici,” *Ww.Gse.It*, vol. 2016, pp. 1–97, 2016.
[23] “Matlab R2016b.” [Online]. Available: https://it.mathworks.com/products/new_products/latest_features.html.
[24] M. National Institute of Standards and Technology, Gaithersberg, “NIST Reference Fluid Thermodynamic and Transport Properties Database (REFPROP): Version 9.1,” 2007.
[25] T. Wendelin, A. Dobos, and A. Lewandowski, “SolTrace: A Ray-Tracing Code for Complex Solar Optical Systems,” *Contract*, no. October, 2013.
[26] F. J. Collado and J. Guallar, “A review of optimized design layouts for solar power tower plants with campo code,” *Renew. Sustain. Energy Rev.*, vol. 20, pp. 142–154, 2013.
[27] J. Spelling, *Hybrid Solar Gas-Turbine Power Plants - A Thermoeconomic Analysis*. 2013.
[28] S. Semprini, D. Sánchez, and A. De Pascale, “Performance analysis of a micro gas turbine and solar dish integrated system under different solar-only and hybrid operating conditions,” *Sol. Energy*, vol. 132, pp. 279–293, 2016.
[29] M. Binotti, P. De Giorgi, D. Sanchez, and G. Manzolini, “Comparison of Different Strategies for Heliostats Aiming Point in Cavity and External Tower Receivers,” *Sol. Energy*, 2016.
[30] W. G. Le Roux, T. Bello-Ochende, and J. P. Meyer, “The efficiency of an open-cavity tubular solar receiver for a small-scale solar thermal Brayton cycle,” *Energy Convers. Manag.*, 2014.
[31] M. Biassoni, “Tesi: PRODUZIONE DI IDROGENO SOLARE TRAMITE REATTORE TERMOCHIMICO AD OSSIDI DI CERIO,” Politecnico di Milano, 2015.
[32] A. Segal, “Optimum layout of heliostat field when the tower-top receiver is provided with secondary concentrators,” 2012.
[33] M. Binotti, G. Manzolini, and G. Zhu, “An alternative methodology to treat solar radiation data for the optical efficiency estimate of different types of collectors,” *Sol. Energy*, vol. 110, pp. 807–817, 2014.
[34] L. Aichmayer, “Solar Receiver Design and Verification for Small Scale Polygeneration Unit.”
[35] L. Amsbeck, R. Buck, P. Heller, J. Jedamski, and R. Uhlig, “Development of a tube receiver for a solar-hybrid microturbine system,” *Proc. 14th SolarPACES Conf. Las Vegas, NV, March*, no. November, pp. 4–7, 2008.
[36] R. Korzynietz *et al.*, “Solugas - Comprehensive analysis of the solar hybrid Brayton plant,” *Sol. Energy*, 2016.
[37] M. Quero, R. Korzynietz, M. Ebert, A. A. Jiménez, A. Del Río, and J. A. Brioso, “Solugas - Operation experience of the first solar hybrid gas turbine system at MW scale,” in *Energy Procedia*, 2013.
[38] M. Lubkoll Promoters, T. van Backström, and D. Kröger, “Spiky Central Receiver Air Pre-heater (SCRAP) an introduction,” 2013.

[39] P. Poživil, “On-sun demonstration and heat transfer analysis of a modular pressurized air solar receiver.” 2015.
[40] F. P. Incropera, D. P. DeWitt, B. T.L, and L. A.S, *No Title*, vol. 7th editio. John Wiley & Sons Inc, 2007.
[41] A. L. Ávila-Marín, “Volumetric receivers in Solar Thermal Power Plants with Central Receiver System technology: A review,” *Sol. Energy*, 2011.
[42] R. M., P. M., and B. R., “Multiple Air-Jet Window Cooling for High- Temperature Pressurized Volumetric Receivers: Testing, Evaluation, and Modeling,” *J. Sol. Energy Eng.*, 2006.
[43] K. A. *et al.*, “Performance of the Directly-Irradiated Annular Pressurized Receiver (DIAPR),” *J. Sol. Energy Eng.*, 2001.
[44] I. Hischier, “Experimental and Numerical Analyses of a Pressurized Air Receiver for Solar-Driven Gas Turbines,” *J. Sol. Energy Eng.*, vol. 134, no. 2, p. 21003, 2012.
[45] M. Lubkoll, T. W. Von Backström, T. M. Harms, and D. G. Kröger, “Initial Analysis on the Novel Spiky Central Receiver Air Pre-heater (SCRAP) Pressurized Air Receiver,” in *Energy Procedia*, 2015.
[46] P. Poživil, V. Aga, A. Zagorskiy, and A. Steinfeld, “A pressurized air receiver for solar-driven gas turbines,” in *Energy Procedia*, 2013.
[47] T. Reference, “Capstone Turbine Corporation Capstone C200 Microturbine,” no. June, 2009.
[48] R. Carrara and A. Mologni, “Analisi e ottimizzazione dell’impianto sperimentale MCFC-Microturbina in realizzazione presso il CESI,” 2004.
[49] E. Keneth and P. E. Nichols, “How to Select Turbomachinery For Your Application How to Select Turbomachinery For Your Application,” *Barber-Nichols Inc.*
[50] S. Campanari, “Full load and part-load performance prediction for integrated SOFC and microturbine systems,” *Eng. Gas Turbines Power*, 2000.
[51] O. O. Omatete, P. J. Maziasz, B. A. Pint, and D. P. Stinton, “Assessment of Recuperator Materials for Microturbines,” 2000.
[52] Corporation Capstone, “Final Technical Report,” 2008.
[53] M. A. Rosa do Nascimento *et al.*, “Micro Gas Turbine Engine: A Review,” *Prog. Gas Turbine Perform.*, pp. 107–141, 2013.
[54] R. Petela, “Exergy of undiluted thermal radiation,” *Sol. Energy*, 2003.
[55] M. Pons, “Exergy analysis of solar collectors, from incident radiation to dissipation,” *Renew. Energy*, 2012.
[56] J. Pye, M. Zengh, C. Asselineau, and J. Coventry, “An exergy analysis of tubular solar-thermal receivers with different working fluids,” 2015.
[57] “Sankey Matic.” [Online]. Available: http://sankeymatic.com.
[58] D. T. Informativo, P. Per, and L. A. Del, “Incentivazione degli impianti solari termodinamici,” 2014.
[59] E. Pihl, “Concentrating Solar Power,” no. April, pp. 8–15, 2009.
[60] W. Short and D. J. Packey, “A Manual for the Economic Evaluation of Energy Efficiency and Renewable Energy Technologies,” *Renew. Energy*, vol. 95, no. April, p. 30896, 1995.

[61] L. Galanti and A. F. Massardo, “Micro gas turbine thermodynamic and economic analysis up to 500kWe size,” *Appl. Energy*, vol. 88, no. 12, pp. 4795–4802, 2011.
[62] T. R. Mancini, J. A. Gary, G. J. Kolb, and C. K. Ho, “Power Tower Technology Roadmap and cost reduction plan.,” no. April, 2011.
[63] “SAM.” [Online]. Available: https://sam.nrel.gov.
[64] F. Von Reeken, D. Nicodemo, T. Keck, G. Weinrebe, and M. Balz, “Key aspects of cost effective collector and solar field design,” *AIP Conf. Proc.*, vol. 1734, 2016.
[65] G. Weinrebe, F. Von Reeken, M. Wöhrbach, T. Plaz, V. Göcke, and M. Balz, “Towards holistic power tower system optimization,” *Energy Procedia*, vol. 49, no. July 2015, pp. 1573–1581, 2013.
[66] T. Lombardo, “AORA Concentrated Solar Power: A Scalable Solution,” 2015.
[67] A. Michler, “AORA’s Second Tulip Power Plant Springs Up in Spain,” 2012.
[68] B. P. S. Review and W. E. June, “BP Statistical Review of World Energy 64 th edition Natural gas,” no. June, 2015.
[69] Groupe Reaction Inc., “CSP Solar Tower Report: Cost, Performance and Key Trends,” 2013.
[70] GME, “Report - Mercato del Giorno Prima,” p. 3.
[71] “Mercato Elettrico.” [Online]. Available: http://www.mercatoelettrico.org/.
[72] GSE, “Prezzi medi mensili per fascia oraria e zona di mercato,” 2016.
[73] Q. Li, Z. Wang, F. Bai, S. Chu, and B. Yang, “Thermal Analysis of Honeycomb Ceramic Air Receiver.”
[74] F. Gomez-Garcia, J. González-Aguilar, G. Olalde, and M. Romero, “Thermal and hydrodynamic behavior of ceramic volumetric absorbers for central receiver solar power plants: A review,” *Renewable and Sustainable Energy Reviews*. 2016.
[75] C. Zou, Y. Zhang, Q. Falcoz, P. Neveu, J. Li, and C. Zhang, “Thermal Modeling of a Pressurized Air Cavity Receiver for Solar Dish Stirling System.”